Modeling of Warm Dense Plasmas for the Determination of Transport Properties and Equation of State

by

Nathanael Gill

A dissertation submitted to the Graduate Faculty of
Auburn University
in partial fulfillment of the
requirements for the Degree of
Doctor of Philosophy

Auburn, Alabama
May 2, 2020

Keywords: Warm Dense Matter, Opacity, Equation of State, Average Atom

Approved by

Stuart Loch, Chair, Professor of Physics
Charles Starrett, Staff Scientist, Los Alamos National Laboratory
Christopher Fontes, Staff Scientist, Los Alamos National Laboratory
Marcelo Kuroda, Assistant Professor of Physics
Konrad Patkowski, Associate Professor of Physics

Abstract

We present the results of research studying the properties of dense plasmas using the average atom model. The average atom model is a physically reasonable statistical representation of an atom in a plasma, and various forms of average atom models have been implemented over the past four decades. We developed a formalism using Green's functions to construct an average atom electronic density that overcomes many of the numerical difficulties that plague other implementations. The code developed in this work includes a relativistic and nonrelativistic implementation. The average atom model, though in and of itself useful to describe the statistical properties of a dense plasma, also serves as an excellent starting point upon which additional models can be built. We demonstrate how the underlying average atom model implemented in the beginning of this work (Chapters 2 and 3) could be built upon to include more correlations between ions in the plasma. This is done through use of a pseudoatom model that incorporates information on the correlations between ions and electrons in the plasma on top of an average atom calculation. In Chapter 4 we use this model to extract a mean-force potential which allows us to get improved results for electrical conductivity, with especially significant results for the free-free contribution. In Chapter 5 we apply a molecular dynamics calculation along with the pseudoatom model to create a more physically informed structure factor for the ions in a plasma. In Chapter 6 we show that the average atom model provides a good ground state electron density for use in a time-dependent density functional theory calculation. These time-dependent calculations incorporate the dynamic response of the multi-electron average atom system to an external perturbation, and the results generated show good agreement with experiments. Overall the work in this dissertation collectively demonstrates the usefulness of the average atom model as both a means of determining thermodynamic properties of plasmas and as a starting point for building more complex models.

Acknowledgments

Any good education in physics should highlight the complexity and vastness of interactions between all things. Though the application of mathematical techniques to the study of nature can be applied to systems of any complexity and scale, my study of complex plasmas has made it clear that capturing the full-breadth of correlations in dense, large systems is an intractable problem. As such my ability to fully understand the contributions and influences of the many people and institutions involved in my life over the past several decades is severely lacking, and due to this I will undoubtedly exclude or understate the importance of some within this acknowledgments section. Still, there are those whose place in my heart will be forever fixed and apparent, and that is what I hope these pages make clear.

The journey through my higher education in physics has been supported and influenced at every step by the faculty and staff of the physics department at Auburn University. From being provided the opportunity to start research from my first week of college to being broken down and built up in Francis Robicheaux's oral homeworks to being made to feel like part of an academic family at the annual Christmas potluck, I have been profoundly appreciative of the people in Auburn. I would especially like to that thank Stuart Loch for his support of this joint research opportunity with Los Alamos National Laboratory over the last 5 years. Beyond that support I would also like to thank him for the many conversations we have had regarding physics education, Rydberg continua, and many other topics.

My time in Los Alamos has been a bittersweet period, filled with enlightening research, terrible medical news, stressful but rewarding business opprotunities, and reassurance of the goodness of humanity. During the many long and terrifying nights that Kathryn and I have been through in the last several years, I always knew that when the sun rose over the Land of Enchantment, I would have the support and sympathy of those at work. Though everyone in XCP-5 have shown their support, I have to specifically thank Kevin Honnell and Patrick Talou for being managers that treated me like a human while still guiding and enabling me to progress

my career. The kindness of my other colleagues has been the saving grace of the last 5 years and I cannot possibly list them all here, but I would like to specifically thank Tina Jenkins and Maureen Johnson for dealing with my many, many documents (both medical and for remote work) and saving me countless bureaucratic headaches.

My education has not followed a traditional pattern, and I have Charlie Starrett, Didier Saumon, and Kevin Honnell to thank for that. My first internship at LANL under Charlie and Didier was enlightening, fun, and made me fall in love with the study of quantum mechanics in dense plasmas. Kevin provided the support needed for me to continue this study as part of my education and this dissertation. Though I owe Charlie more than I can say, I will unfortunately dissapoint him here by not being concise in my appreciation of him. Charlie has been a phenomenal advisor, maintaining the utmost in professionalism as a mentor while being honest, kind, and direct in his guidance of my progress towards a career. He has let me find my own way in my research while guarding against my often over-zealous optimism, but simultaneously he has helped me shake off unrealistic pessimism in both my research and my life. As a physicist he serves as an example of what to be: professional, realistic, competent, adaptable, ever-yearning for new information, and humble. As a friend he serves as an example of what to be: supportive without smothering, sympathetic without platitudes, and present without request. I have caused him more work than he signed on for but he has never let it stymie his mentorship of me. To attempt to reign in my verbosity, I owe Charlie, more than any other person, for my right to call myself a physicist.

To say that my family has been influential in my life would be an understatement. My grandfather taught me the value of wisdom and showed me what it meant to be a man of integrity. My father has given me an example that has influenced my approach to science, engineering, philosophy, psychology, education, survival, and too many other things to list. I only regret that my path as a theoretician will likely never lead to me rivalling his mechanical savvy. My siblings greatly influenced my early life, and the lessons I learned from them directed me into my early adulthood. Specifically, I wish to thank my mother, Arlene. Her work ethic, her ability to pragmatically assess any situation, and her respect for me taught me more than all of the education I have received. She supported my independence in college and has been here for

Kathryn and me when we needed her the most. I cannot thank her enough for everything she has done over the past 30 years.

Though this section is for professional and personal acknowledgments, how I feel about Kathryn Allison Gill goes beyond mere acknowledgment. Few can say they were fortunate enough to marry their best friend, and I am chief among the few. She has taught me how to feel the dance within the music, hear the music within the math, and stop seeing everything in terms of only the math. She has believed in me in the darkest of moments and gave me courage in the face of fear. Her strength is an inspiration and her continued kindness is an indescribable virtue. Since she has entered my life, her unique perspective has colored my monochrome brain, leaving nothing of me untouched or uninspired by her. Due to unfortunate circumstances we have been stuck at home together for far longer than just the COVID-19 isolation, and amazingly we still grow in love for each other every day. Her sacrifices, her love, her support, her quirkiness, her passion, and her directness have given me a complete life of experiences before I have even hit middle-age. She is the star in the darkest night, and I could never have become the person or the physicist I am today without her.

Finally, some anectdotal thanks: Auburn SPS (for all of the fun, the philosophy, the politics, and the friends); Chris Fontes (for making me proudly feel like an old man as we chat about eggcellent gameshows of days long past and the sociopolitical dynamics of our field); Anya and Aria (for always being happy to see me and being there for me whenever I need comfort); the Allisons and Edgeworths (for giving me another family and helping Kathryn and me make our life together); Francis Robicheaux (for teaching me what being “clever” really means); the Adventuring Adventurers (for making sure that I always have friends and new adventures in my life); Frasier (for bringing about the modern sitcom and setting the standard for the many hours of quality comedy that I have enjoyed over the last decade); Wikipedia (for all of the stuff I have no reason to know, but know nonetheless); World Book Encyclopedia (for starting me down this path over 20 years ago).

Table of Contents

Abstract ii

Acknowledgments iii

1 Introduction 1

1.1 Warm and Hot Dense Matter 2

1.2 Average Atom Model 4

1.2.1 Overview of Average Atom Model 6

1.2.2 Benefits and Difficulties of Average Atom Model Calculations 11

1.2.3 Adaptation of Average Atom Models to Complex Applications 14

1.2.4 Alternative Methods 21

1.3 Outline of Chapters 22

1.3.1 Chapter 2 - Tartarus Model Description 23

1.3.2 Chapter 3 - Tartarus Code Package 24

1.3.3 Chapter 4 - Mean Force Scattering Potential 24

1.3.4 Chapter 5 - Dynamic Structure of Plasma Mixtures 25

1.3.5 Chapter 6 - Time-Dependent DFT and the Linear Response of Plasmas . 25

1.3.6 Conclusion and Appendices 26

2 Tartarus: A relativistic Green's function quantum average atom code 27

2.1 Abstract 27

2.2 Introduction 27

2.3 Theory 29

2.3.1 Average Atom Model and DKS-DFT Orbitals 29
2.3.2 Green's Function Formalism 32
2.3.3 Thermodynamic Quantities 33
2.4 Numerical Details 36
2.4.1 Wavefunction Normalization, Complex Spherical Bessel Functions and Choice of Contour 36
2.4.2 High Angular Momentum States 38
2.4.3 Calculation Speed 40
2.5 Results 41
2.5.1 Thermodynamic Consistency 41
2.5.2 Shock Hugoniots 41
2.6 Discussion 43

3 Wide Ranging Equation of State with `Tartarus`: a Hybrid Green's Function/Orbital based Average Atom Code 47
3.1 Abstract 47
3.2 Introduction 47
3.3 Average Atom Model 48
3.3.1 Model Description 48
3.3.2 Poisson Equation 50
3.3.3 Electron density 50
3.3.4 Boundary Conditions 53
3.3.5 Density of States 55
3.3.6 Equation of State 56
3.3.7 Summary 57
3.4 Numerical Methods 57
3.4.1 Numerical Solution of the Schrödinger and Dirac Equations 57

3.4.2 Contour Integrals for Green's Functions . . . 59
3.4.3 Density Construction . . . 61
3.4.4 Self Consistent Field Acceleration . . . 65
3.5 Example . . . 69
3.5.1 Density of States . . . 69
3.5.2 Extraction of Ionization . . . 73
3.6 Case Study: Equation of State of Lutetium . . . 77
3.7 Conclusions . . . 88

4 Mean-Force Scattering Potential for Calculating Optical Properties of Dense Plasmas 89
4.1 Abstract . . . 89
4.2 Introduction . . . 89
4.3 Theory . . . 91
4.3.1 Average Atom Potential . . . 91
4.3.2 Potential of Mean Force . . . 92
4.3.3 Optical Properties . . . 93
4.4 Results . . . 96
4.4.1 DC Conductivity . . . 96
4.4.2 AC Conductivity . . . 97
4.4.3 Opacity . . . 101
4.4.4 Temperature and Density Effects on Ion-Correlation Features . . . 103
4.5 Conclusion . . . 110

5 Ion-ion dynamic structure factor of warm dense mixtures . . . 112
5.1 Abstract . . . 112
5.2 Introduction . . . 112
5.3 Methods . . . 114

5.4 Results . . . 121
5.4.1 Aluminum plasmas . . . 121
5.4.2 Carbon-hydrogen Plasma . . . 124
5.5 Conclusions . . . 128

6 Linear Response Time-Dependent Density Functional Theory Applied to Absorption Cross-sections . . . 129
6.1 Theoretical Overview of Linear Response TD-DFT . . . 132
6.1.1 Linear Density Response . . . 132
6.1.2 Time-Dependent Kohn-Sham Equation . . . 134
6.1.3 TDKS Linear Response . . . 135
6.2 Induced Linear Response . . . 136
6.2.1 Induced Density . . . 136
6.2.2 Application to Photoabsorption . . . 137
6.3 Practical Implementation of TD-DFT . . . 139
6.3.1 Independent Particle Approximation and χ_0 . . . 140
6.3.2 Self Consistent Field Approach . . . 143
6.3.3 Implementation in Radial Expressions . . . 145
6.3.4 Numerical Considerations . . . 147
6.4 Results . . . 153
6.4.1 Neutral Gas Results . . . 153
6.4.2 Finite Temperature Plasma Results . . . 158
6.5 Conclusions and Future Work . . . 162

7 Conclusions . . . 167

Appendices . . . 169

A Radial Expressions of the TD-DFT Formalism 170

A.1 Treatment of Angular Dependence of δn 171

A.2 Resulting Expressions for δV_C and δV_{XC} 173

A.3 Determination of $G_l(r, r', E)$ 176

A.4 Expressions Implemented in Code 176

A.5 Unchanging Susceptibility-Like Term 177

A.6 Polarizability 178

References 179

List of Figures

1.1 This figure shows some of the rough plasma conditions at which certain physical systems exist. Lines are drawn showing $\Gamma = 1$ and $\Theta = 1$ (which is identical to the condition $k_B T = E_F$, where k_B is the Boltzmann constant, T is the particle temperature, and E_F is the Fermi energy). The green shaded area represents the general conditions for which warm dense matter exists. Figure provided via free license: By Madayano - Own work, CC BY-SA 4.0, https://commons.wikimedia.org/w/index.php?curid=50048287 5

1.2 This diagram gives a basic illustration of the SCF procedure used to solve for the ground state electronic density within the DFT formalism. The better the initial guess at the electron density (Step "0" in the diagram), the fewer iterations of the solver are needed to converge on a final electron density. 8

1.3 (This figure also appears in Chapter 3 of this work.) Schematic diagram of average atom physical model. Inside the ion sphere the electronic structure is determined with density functional theory. The boundary condition is that outside the sphere the effective electron-nucleus potential is zero. 10

1.4 This diagram shows the iterative procedure used in order to determine the average atom electronic structure. In this diagram, the chemical potential of the electrons in the system, μ, must be varied in order to ensure that the integral of the electron density within the ion-sphere produces the same number of electrons as protons within the nucleus of the ion, Z. 12

1.5 This diagram shows an overview of the general algorithm used to solve the AA-TCP model. An initial guess for the ion-ion pair distribution function, g_{ii}, as a step function at the ion-sphere radius is used to solve the AA/Pseudoatom model, which yields the screening electron density. This density, along with two other closure relations, allows for the determination of an ion-ion pair distribution function from the coupled AA-TCP model. This more informed distribution function can then be fed back into the AA calculation, and the two calculations can be iterated until converged. Starrett and Saumon showed that the g_{ii} resulting from the first iteration is largely unchanged over subsequent iterations [1]. 19

2.1 Comparison of the number of electrons in each calculated partial wave, $Z_l = \int_V n_l d\vec{r}(\vec{r})$, for both the numerically determined waves (Z_l) and the known free waves (Z_l^0) in aluminum at solid density and 1000 eV. 39

2.2 Thermodynamic consistency of the plasma pressure in silicon and aluminum (both at solid density) as calculated using the virial theorem and differentiation of the free energy. $\Delta P/P = \frac{P_{virial}-P_{thermodynamic}}{P_{virial}}$, where P_{virial} is the pressure obtained through use of the virial theorem and $P_{thermodynamic}$ is the pressure obtained from numerical differentiation of the free energy. 42

2.3 Comparison of the principal shock Hugoniot determined by the nonrelativistic and relativistic modes of Tartarus and the PIMC/DFT-MD method of Militzer et al. The compression ratio is the shocked density divided by the nominal density, $\rho_0 = 2.33$ g/cm^3 [2] 44

2.4 Comparison of the nonrelativistic and relativistic modes of the Tartarus calculation for silver, with $\rho_0 = 10.49$ g/cm^3. No error was given in the sources for the experimental data [3, 4]. 45

3.1 Schematic diagram of average atom physical model. Inside the ion sphere the electronic structure is determined with density functional theory. The boundary condition is that outside the sphere the effective electron-nucleus potential is zero. 51

3.2 Grid spacing $r_{i+1} - r_i$ for various grid generation methods described in the text. 58

3.3 Example of SCF acceleration for lutetium at 10 eV and 10 g/cm^3. We compare simple mixing to Eyert's method with $M = 5$, as a function of the mixing parameter α. 66

3.4 Example of SCF acceleration for lutetium at 10 eV and 10 g/cm^3. We compare Eyert's method with $\alpha = 0.9$ as a function of the order M. 67

3.5 Density of states $\chi(z)$ for lutetium at 10 g/cm^3 and 10 eV. The solid red line is calculated using orbitals along the real energy axis. Using Green's functions we can evaluate $\chi(z)$ for complex energy z. Increasing the imaginary part of z features, including the discrete bound states and a continuum resonance, are broadened, making them easy to integrate over. Note $\Im z = 0.5$ E$_h$ is typical for the horizontal part of our integration contour. 70

3.6 Density of states $\chi(\epsilon)$ for lutetium at 10 eV for real energy ϵ. 71

3.7 Average ionization of lutetium at 10 eV. Two definitions are explored. Note that the definition choice does not affect in any way the properties of the average atom, for example, the equation of state does not depend on the definition. For $\bar{Z}$ the more prominent ionization features are labelled. 72

3.8 Isotherms of entropy of lutetium plasma from `Tartarus`. Both non-relativistic (solid lines) and relativistic (dashed lines) are shown for temperatures from 0.1 eV to 1 keV. For any given density the entropy increases with temperature, as expected. 74

3.9 Isotherms of internal energy of lutetium plasmas from Tartarus. Both non-relativistic (solid lines) and relativistic (dashed lines) are shown for temperatures from 0.1 eV to 1 keV. 75

3.10 Electron pressure of lutetium plasmas along isotherms. Both relativistic and non-relativistic results are shown. The inset also shows electron pressure but focused on the low temperature region where entropy increases with density for fixed temperature. The result is a region where pressure increases as temperature is lowered, for a fixed density. 76

3.11 Electron pressure for lutetium divided by the pressure of a non-interacting, relativistic, quantum electron gas with electron density Z/V^{ion}. 79

3.12 Electron pressure for lutetium from Tartarus (relativistic) compared the Thomas-Fermi model's prediction [5]. Note we have used the same exchange and correlation potential for both [6]. 80

3.13 The effect of finite temperature exchange and correlation on the average ionization per atom Z^*. We compare the zero temperature Perdew-Zunger (PZ) functional [6] to the recent finite temperature functional [7] (here labeled QMC17). In the panel (a) we show $\Delta Z^* = Z^*$(PZ) - Z^*(QMC17), in panel (b) we show $\Delta Z^*/Z^*$, where Z^* is calculated with PZ. The bottom two panels (c) and (d) show the same Z^*(PZ) but on different scales. 81

3.14 Isocore (9.773 g/cm^3) of lutetium comparing results from the Abinit plane wave code using a HCP crystal structure to Tartarus results. 83

3.15 Isotherm (0.0285 eV) for lutetium compared to the plane wave code Abinit using the HCP crystal structure. 85

3.16 Comparison of pressures from Tartarus for lutetium calculated with the virial expression (3.39) and via a numerical differentiation of the free energy $P = -\partial F/\partial V|_T$. 87

4.1 Here we compare the DC conductivity calculated with the average atom and mean force potentials with the results obtained by Witte et al. [8] for aluminum at solid density (2.7 g/cm^3). Witte et al. used finite-temperature DFT-MD with both the HSE and PBE functionals. We also show the results of a relaxation time approximation as is done in Ref [9] in the results labeled MF Relaxation Time. 98

4.2 We compare the results of the V_{eff}^{AA} and V^{MF} calculations with the DFT-MD results of Witte et al. [8] for the AC conductivity of aluminum at solid density over several temperatures. The top inset shows the location of the 2p edge for the .5 eV case. We can see from this how the V^{MF} eigenvalues differ significantly from the DFT-MD and V^{AA} values. The bottom inset shows the mean force results with a broadened bound state width comparable to the DFT-MD results for the 12 eV case. The difference in the frequency location of the bound-bound transition feature is due to the different exchange-correlation functionals used in the two calculations. The inset axes are the same units as the main plot. 99

4.3 We compare the opacity as calculated with V_{eff}^{AA} and V^{MF} for aluminum at 10 eV and solid density. The red curve labeled "AA with MF free-free" uses the free-free part of the opacity calculated with V^{MF} and V_{eff}^{AA} bound-bound and bound-free parts of the opacity. We can see that the bound-bound and bound-free transitions are generally weakly affected by use of V^{MF}, and therefore have a small effect on the total opacity in contrast to the effect on free-free transitions. 100

4.4 Opacity for deuterium at various densities and temperatures as compared to the DFT-MD results found in reference [10]. The V^{MF} results show improved agreement with the DFT-MD results compared to the V_{eff}^{AA} opacity. The opacity in this case is entirely due to free-free transitions. 102

4.5 We show the f-sum rule for the opacity as a function of frequency for aluminum at 1 eV and solid density. The high frequency limit is the total number of electrons. The eigenvalues of the average atom electronic states are shown, as well as the chemical potential, μ, of the system, which is the same in both the V_{eff}^{AA} and V^{MF} calculation. 104

4.6 Mass absorption coefficient for various densities and temperatures of aluminum, which is the opacity divided by the mass density of the plasma. The V_{eff}^{AA} results are in black with the V^{MF} results in dashed green. The values of the electron degeneracy parameter, Θ, and the plasma coupling parameter, Γ, are shown as (Θ, Γ) for each temperature and density. 106

4.7 Mass absorption coefficient for various densities and temperatures of iron. The V_{eff}^{AA} results are in black with the V^{MF} results in dashed green. The values of the electron degeneracy parameter, Θ, and the plasma coupling parameter, Γ, are shown as (Θ, Γ) for each temperature and density. The low temperature, solid density results show that the average atom calculation has difficulties fully capturing the free-free opacity. 107

4.8 We show the calculation of the iron opacity at 182 eV and .4 g/cm^3. The differences between the V_{eff}^{AA} and V^{MF} calculations are small, and only has appreciable difference in the 400 eV to 800 eV range, though we see far less of a significant difference in this frequency range when compared to Krieff et al [11]. 108

4.9 We show the calculation of the iron opacity at 182 eV and .4 g/cm^3 in the range accessible by the Bailey et al. experiment [12]. The differences we see between the two calculations are negligible compared to the discrepancies highlighted by the experiment, indicating that the effect of ion correlations does not account for the missing opacity. Since the average atom model cannot resolve individual ion stages, there is no meaning in directly comparing to the experimental data. 109

5.1 $S(k, \omega)$ for aluminum at 5.2 g/cm^3 and 3.5 eV. Solid lines are PAMD calculations and the numbers beside each curve indicate the k-value. The dashed lines are from QMD simulations [13] and the legend indicates their k-values. Despite the very different simulation methods involved, the agreement is good. The differences result from a combination of physical approximations and computational limitations (see text). 116

5.2 Dispersion relation ω_s (top panel) and adiabatic sound speed $c_s = \omega_s/k$ (bottom panel) for aluminum at 5.2 g/cm^3 and 3.5 eV. Solid lines with triangles are PAMD calculations using 10,000 particles. The blue dots are QMD results from [13], where 256 particles were used. For comparison, we also plot the results of a PAMD simulation using 256 particles (solid lines with squares). . . 117

5.3 Static structure factor (top panel) and $S(k, \omega)$ (bottom panel) for aluminum at 2.7 g/cm^3 and 5 eV compared to TF-DFT-MD simulations [14]. We show PAMD results using both Thomas-Fermi (TF) and Kohn-Sham (KS) functionals. ω_p is the ion plasma frequency. For KS-PAMD $\hbar\omega_p$ = 0.123 eV, for TF-PAMD $\hbar\omega_p$ = 0.125 eV. 118

5.4 Dispersion relation ω_s (top panel) and adiabatic sound speed $c_s = \omega_s/k$ (bottom panel) for aluminum at 2.7 g/cm^3 and 5 eV. We show PAMD results using both Thomas-Fermi (TF) and Kohn-Sham (KS) functionals. 119

5.5 Static structure factor (top panel) for aluminum at 5.2 g/cm^3 and 3.5 eV. The bottom two panels show the calculated dynamical structure factor and the hydrodynamical fit (equation (5.1)). The four fit parameters are determined by a least squares fit of the calculated data for $k = 0.143$ Å^{-1}. On increasing k (values are marked beside the corresponding lines) this hydrodynamical fit begins to deviate from the calculated curves, as is expected. 120

5.6 Static structure factor from PAMD (top panel) for a carbon-hydrogen mixture at 10 g/cm^3 and 10 eV. The bottom three panels show the dynamic structure factors for C-C, H-H and C-H at various fixed values of k. 123

5.7 Elastic part of the electron-electron dynamic structure factor for CH at 10 eV and 10 g/cm^3. The k-values and line labels in this figure and inset are the same as in figure 5.6. 125

5.8 Top panel shows the dispersion relations extracted from the PAMD dynamic structure factors $S_{CC}(k,\omega)$, $S_{HH}(k,\omega)$ and $S^{el}_{ee}(k,\omega)$ as well as the dispersion relations for a pure hydrogen and a pure carbon plasma at the same temperature and density as the mixture (10 eV and 10 g/cm^3). In the bottom panel the corresponding adiabatic sound speeds ($c_s = \omega_s/k$) are shown. For clarity, the sound speed for the pure hydrogen case has been shifted by -35 km s^{-1}. 127

6.1 A schematic of the SCF procedure and radial functions used to determine the induced density. 148

6.2 Here we see the results for the SCF calculation of the photo-absorption cross-section (σ) when we enforce a minimum energy as a criterion for whether we consider the contribution of an initial state to the susceptibility. IND refers to the independent particle solution, and SCF refers to self-consistent solutions to TDKS equations. 154

6.3 This figure shows the photo-absorption cross-section (σ) for neon compared to results digitized from Caizergues et al. [15] and to the experimental results of Marr and West [16]. We see a modest reduction of the cross-section in the SCF results for the frequency range shown on the plot. This reduction translates to a redistribution of the spectrum towards higher energies. The slight offsets in peak features (notably the 2p ionization near $.5E_H$) are due to the differences in exchange-correlation energy and to the finite temperature and density used in our calculation. IND refers to the independent particle solution, and SCF refers to self-consistent solutions to the TDKS equations. 156

6.4 This figure shows the photo-absorption cross-section (σ) for argon compared to results digitized from Caizergues et al. [15] and to the experimental results of Marr and West [16]. We see a very dramatic shift of the cross-section towards higher frequencies, including changing where the peak absorption occurs in neon. IND refers to the independent particle solution, and SCF refers to self-consistent solutions to TDKS equations. 157

6.5 This figure shows the photo-absorption cross-section (σ) for xenon compared to results digitized from Caizergues et al. [15] and to the experimental results of Hansel et al. [17]. IND refers to the independent particle solution, and SCF refers to self-consistent solutions to TDKS equations. 159

6.6 This figure shows the photo-absorption cross-section (σ) for solid density iron (7.85 $\mathrm{g/cm^3}$) at 100 eV. This work was also done by Grimaldi et al. [18], but the data in the publication could not be easily digitized without significant loss of quality. This figure is directly comparable to Figure 8 in Reference [18]. We see sharp features in the SCF results that arise from Fano resonances at frequencies corresponding to bound-bound transition energies. IND refers to the independent particle solution, and SCF refers to self-consistent solutions to the TDKS equations. 161

6.7 This figure shows the photo-absorption cross-section (σ) for cold manganese in the isolated atom limit. The primary features of interest are the Fano resonances that appear in the SCF solution. IND refers to the independent particle solution, and SCF refers to self-consistent solutions to TDKS equations. 163

6.8 This figure shows the photo-absorption cross-section (σ) for cold manganese in the isolated atom limit compared to experimental results done at Oak Ridge [19]. The Fano resonance follows the experimental results quite nicely. The discrepencies at low frequency are likely due to temperature and density effects, as the weakly bound states involved in that part of the spectrum are particularly sensitive to the plasma conditions. IND refers to the independent particle solution, and SCF refers to self-consistent solutions of the TDKS equations. . . 164

List of Tables

Chapter 1

Introduction

This dissertation details the use of an average atom model to study warm and hot dense plasmas. The work shown here includes improving the algorithmic and numerical treatment of a standard average atom calculation as well as the use of models built upon the foundation of an average atom to obtain addtional information about these complex plasmas. Average atom models are a class of physical models used to determine an electronic density around a single ion that represents the average of all ions in the plasma. These models are computationally expedient and allow for determining approximate values for quantities of interest within the plasma as a whole (e.g. equation of state [EOS], diffusion coefficients, electrical conductivity, etc.). These plasmas exist at temperatures and densities where typical classical plasma physics approaches fail to provide adequate physical descriptions due to the need to address the quantum mechanical nature of both the bound and free electrons in the system. Further, many techniques for describing the electrons quantum mechanically are difficult or impractical to use without discretion due to the large range of temperatures under study and due to the complicated density effects from the plasma environment.

One of the difficulties in studying warm and hot dense plasmas is that often properties of the plasma, such as transport properties and equation of state (the relation between thermodynamic quantities in the system), are needed over a wide range of plasma temperatures and densities. This necessitates the creation of tables or analytic fits that can be called by multi-physics simulations such as those used to study radiation hydrodynamics. Simulations using robust and expensive calculations (e.g. Density Functional Theory Molecular Dynamics [DFT-MD] for transport properties and equation of state, or Path Integral Monte Carlo [PIMC] for

equation of state) can obtain results with high fidelity, but they are unsuited for application over the full range of plasma conditions necessary.

Average atom models are able to provide a means of determining physically reasonable electronic structure and subsequent plasma properties at the temperatures and densities relevant to warm and hot dense matter, and this is possible with a fraction of the computational cost of many other approaches. In average atom models, the many ions in the system are reduced to having their electronic density represented by a single ion whose nuclear Coulomb potential is screened by the surrounding free electrons and other ions in the plasma. How this screening is incorporated into the model and what constraints (such as boundary and neutrality conditions) are applied when determining the electronic density give rise to different flavors of average atom models. Though average atom calculations are fast, there are significant computational difficulties involved in the simulations, many of which will be explained and addressed in the chapters of this work.

The remainder of this introduction will serve to give more details on the nature of warm and hot dense systems, provide an overview of the average atom and the models derived from it that are applied in the chapters of this dissertation, and give a brief description of other theoretical approaches to modeling dense plasmas.

1.1 Warm and Hot Dense Matter

Many areas of study require understanding the properties of matter at high pressures and densities. The cores of massive planets, brown dwarfs, and white dwarf stars are examples of where warm dense matter exists in nature. Further, an understanding of the behavior of these extreme systems is necessary for simulating radiation-hydrodynamics in the study of solar convection and inertial confinement fusion experiments. Most of the plasmas of interest for our studies have temperatures from near one to tens of thousands of eV and densities ranging from one-thousandth to hundreds of times the material's solid density.

With such a wide range of temperatures and densities encompassing the warm and hot dense states, it is difficult to characterize these systems with temperature, mass density, and electron density alone. The same temperature and densities that would cause a plasma of one

material to fall into the category of warm dense matter would not necessarily describe similar plasma behavior for another material. It is more useful to describe these systems based on the strength of the coupling between the ions and electrons and on the degeneracy of the electrons. To do this it is common to define these two parameters: the plasma coupling parameter, Γ, and the degeneracy parameter, Θ.

The plasma coupling parameter is the ratio of the average potential energy that a particle in the plasma has to the average kinetic energy of the particle. This means that when $\Gamma = 0$, the plasma obeys the ideal gas law. On the other hand, when $\Gamma >> 1$, the plasma is very strongly coupled. Classical plasmas such as those often found in laboratory and magnetically confined plasmas are often marked by $\Gamma << 1$.

The degeneracy parameter is the ratio of the particle's thermal kinetic energy to its Fermi energy. Though the Fermi energy is derived for systems at zero temperature, here it serves as a benchmark that illustrates the energy range over which most of the electronic states are distributed. For systems with $\Theta >> 1$, the electrons are so energetic that the quantum electronic structure is negligible in describing the electron's behavior. When $\Theta << 1$ the system is highly degenerate, with the electronic structure characterized by an occupied density of electronic states spread over a relatively small range of energies. In these degenerate systems, the electrons tend to be packed into the lowest energy states available, which means that excitation of electrons beyond the ionization threshold is often more difficult (due to the lack of unoccupied electronic states nearby in energy to the ionizing electron). High degeneracy is a characteristic of white dwarf cores, where the so-called degeneracy pressure (i.e. pressure caused by the stability of the electronic structure of the degenerate atoms) resists the gravitational collapse of the star.

Warm dense systems can be found when the plasma is moderately coupled and the electrons are partially degenerate, i.e. when $\Gamma \approx 1$ and $\Theta \approx 1$. This is illustrated in Figure 1.1. This condition can also be seen in the following expressions:

$$\Gamma = \frac{(Ze)^2}{R_{WS} k_B T} \approx 1 \tag{1.1}$$

where Z is the atomic number of the element, e is the electron charge, k_B is the Boltzmann constant, T is the system temperature, and R_{WS} is the so-called Wigner-Seitz radius which corresponds to a sphere whose volume is equivalent to the average volume attributable to the ion in the system.

$$\Theta = \frac{k_B T}{E_F} \approx 1 \tag{1.2}$$

where E_F is the Fermi energy of the system. Since the Fermi energy is dependent on the electron density, and the de Broglie wavelength, λ_{dB}, of the electrons is dependent only on the temperature of the system, Θ can also be thought of in terms of the spatial properties of the electrons in the system. The degeneracy parameter is effectively unity when $\lambda_{dB} \approx R_{WS}$.

1.2 Average Atom Model

The average atom physical model underlies almost all of the work demonstrated in this dissertation. Though some of the more nuanced details of the average atom model we use is presented in Chapters 2 and 3 of this work, here we will give a basic overview of what an average atom model is and how it is a powerful tool for describing many of the properties of dense plasmas as well as serving as an excellent foundation upon which to build models with additional physics.

Electronic structure in average atom models is determined using Density Functional Theory (DFT) around a single ionic center. The use of DFT and the simplicity with which the average atom model's constraints are defined make it an ideal model for performing fast calculations of properties such as equation of state. The ability to quickly determine plasma properties is in high demand when generating tables of data needed to inform higher-order physics simulations such as radiation hydrodynamic calculations. As will be shown later in this work, average atom models make for an excellent tool when needing results across a broad range of plasma temperatures and densities.

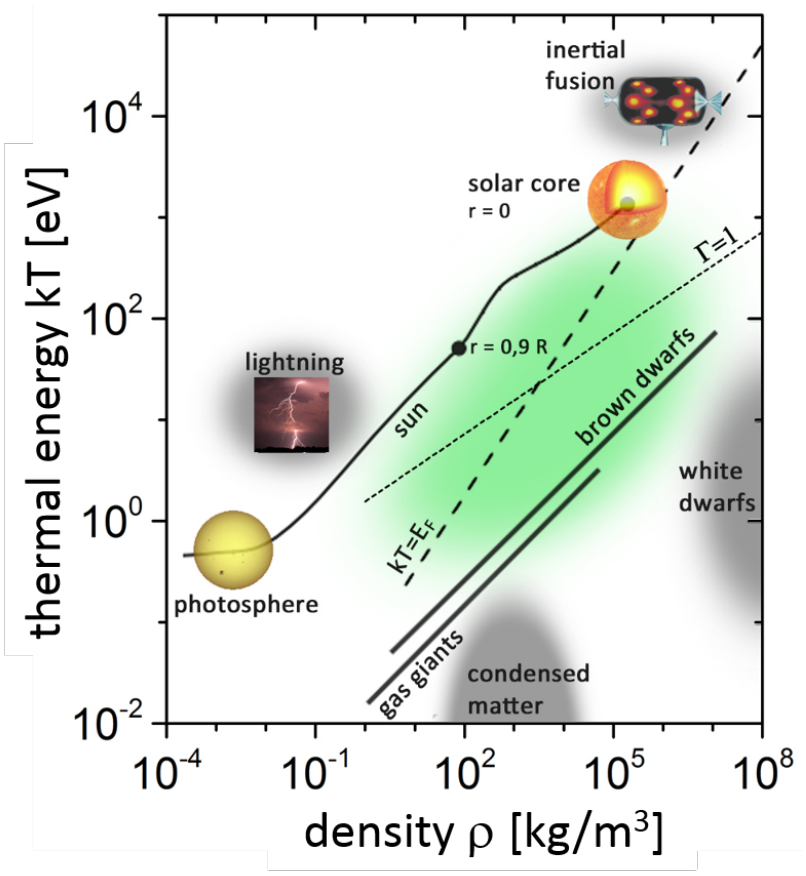

Figure 1.1: This figure shows some of the rough plasma conditions at which certain physical systems exist. Lines are drawn showing $\Gamma = 1$ and $\Theta = 1$ (which is identical to the condition $k_B T = E_F$, where k_B is the Boltzmann constant, T is the particle temperature, and E_F is the Fermi energy). The green shaded area represents the general conditions for which warm dense matter exists. Figure provided via free license: By Madayano - Own work, CC BY-SA 4.0, https://commons.wikimedia.org/w/index.php?curid=50048287

1.2.1 Overview of Average Atom Model

Density Functional Theory

Since the average atom model is reliant on DFT calculations to determine electronic density, it is necessary to understand the basics of DFT before fully describing the nuances of average atom calculations. Density functional theory, in principle an *ab initio* formalism, is capable of fully describing the ground state electronic density of a given system. In practice DFT approaches lack a complete and general quantification of the exchange and correlation effects between electrons in the system, however this does not prevent DFT from being an accurate and relatively expedient method for determining the electronic structure in many-body electronic (and even nuclear) systems.

The basis of the theory was developed by Hohenberg and Kohn [20] in work characterizing inhomogeneous electron gases. In this work they demonstrated two theorems which would serve as the foundation for the complete DFT theory to come:

Theorem 1.1 *The external potential (and hence the total energy), is a unique functional of the electron density.*

Theorem 1.2 *The groundstate energy can be obtained variationally: the density that minimises the total energy is the exact groundstate density.*

Through the use of these theorems and the subsequent mathematical description of electronic ground states with the electron density being the fundamental variable, Kohn and Sham [21] developed the so-called Kohn-Sham DFT. This ground-breaking work allowed for the description of complex, interacting many-body systems to be decomposed and accurately described by non-interacting one-body equations, the so-called Kohn-Sham equations (which functionally take the same form as the Schrodinger equation, but with effective electronic potentials that implicitly include exchange and correlation effects):

$$\left(\frac{-\hbar^2}{2m}\nabla^2 + V_{eff}(\vec{r})\right)\psi_{KS,i}(\vec{r}) = E_{KS,i}\psi_{KS,i}(\vec{r}) \tag{1.3}$$

where V_{eff} contains the external potential (i.e. the potential created by the nuclei), the Coulombic interaction between the various electrons in the systems (i.e. the Hartree potential), and the exchange-correlation potential, V_{xc}, and where $\psi_{KS,i}$ is a single-particle Kohn-Sham eigenstate of energy $E_{KS,i}$ within the effective system. The exchange-correlation potential is based on the functional derivative of the exchange-correlation energy of the system, which is a functional of the electron density. The choice of this functional is the means of introducing approximations to the model, and much work has been done in the past decades to inform the choice of these functionals with as much physics as possible. As one can easily see, Equation 1.3 is analogous to the standard Schrodinger equation description in quantum mechanics, and likewise the KS-Dirac equation is analogous to the Dirac equation for relativistic systems.

As is implied by the second of the Hohenberg-Kohn theorems, the DFT formalism is capable of accessing information on the ground state of the electronic system. Given the free choice of the form of the exchange-correlation functional, the Kohn-Sham equations are solved in a self-consistent (i.e. iterative) procedure, usually starting with an informed guess of the ground state electronic density and iterating the solution of the equation until a converged result is obtained. This iterative procedure is illustrated in Figure 1.2.

Though DFT provides an excellent framework for determining the ground state electron density of many-body systems, there are still problems with the formalism that limit its use on certain problems. These problems arise mainly due to the theory's inability to describe excited states and due to a lack of *ab initio* and general knowledge of the exchange-correlation energy functional. Fortunately for our studies, these problems do not hinder our ability to use DFT to obtain physically reasonable results in an expedient manner. Our model implements the finite temperature extension of the original Hohenberg-Kohn theory—the Mermin generalization [22]. This extension applies to finite temperature systems in thermodynamic equilibrium.

Boundary Conditions and Details of the Average Atom Model

Using DFT we can construct a model for an ion embedded in a plasma. This model should account for the finite density of the plasma. The average atom model does this by defining boundary conditions which are imposed upon the electrons within a DFT calculation. This

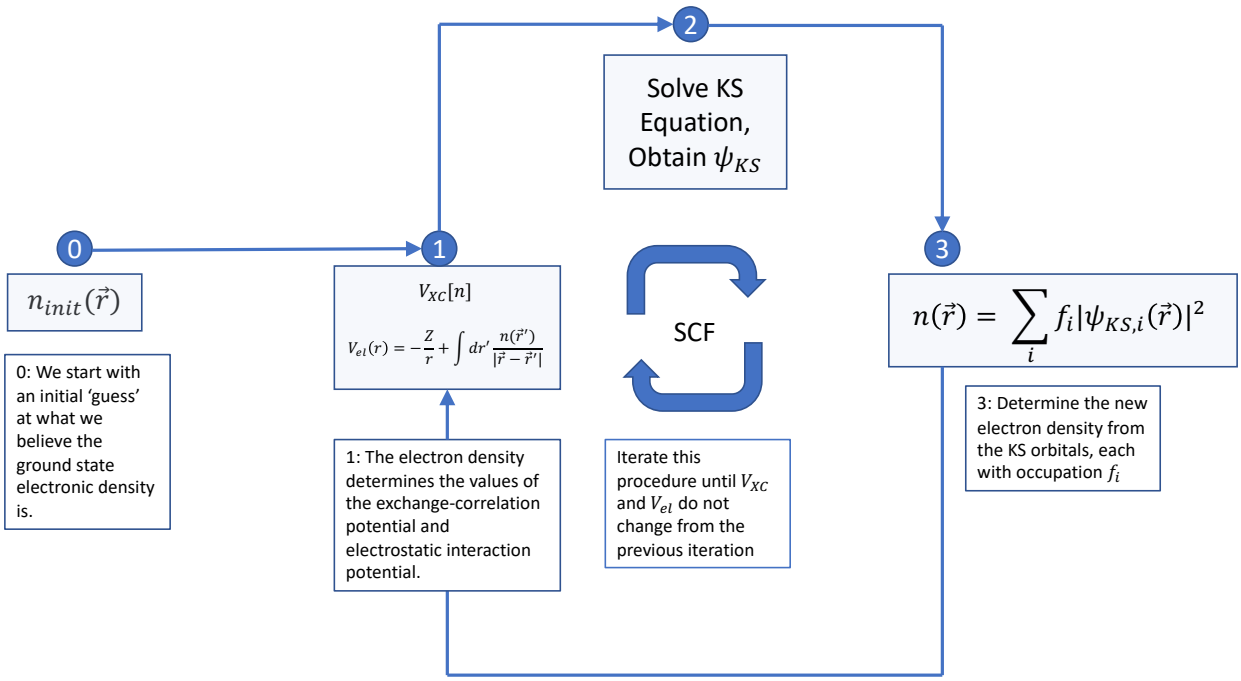

Figure 1.2: This diagram gives a basic illustration of the SCF procedure used to solve for the ground state electronic density within the DFT formalism. The better the initial guess at the electron density (Step "0" in the diagram), the fewer iterations of the solver are needed to converge on a final electron density.

section will briefly outline the history of the average atom model and introduce the form of that model that we built upon in this work.

The earliest rendition of the average atom model was the finite-temperature Thomas-Fermi model described by Feynman, Metropolis, and Teller [5, 23, 24]. This model represents an atom as a sphere immersed in a homogeneous electron gas neutralized by a uniform background of ions. This approach is semiclassical and only determines an electron density without effects from discrete bound electronic states. Nevertheless the Thomas-Fermi model provided the starting point for the first quantum average atom model developed by Rozsnyai [25]. Rozsnyai's model treated the bound electrons and the continuum electrons separately, with a fully quantum mechanical description of the bound states and the Thomas-Fermi description of the continuum electrons. This dual approach leads to discontinuities when determining thermodynamic quantities, but it still represented a first step in developing a quantum mechanical average atom model.

The first fully quantum mechanical average atom model was developed by Liberman [26], which uses a consistent quantum mechanical approach to determine both the bound and continuum electrons. Liberman's average atom model, as well as the Thomas-Fermi and Rozsnyai models, defines an ion-sphere as a sphere whose volume is equivalent to the average volume taken up by an ion in a plasma. Under this definition all that is needed to define the ion-sphere radius is the mass density of the plasma. At this ion-sphere radius, boundary conditions are imposed on the single-particle electron states calculated within the DFT formalism. In Liberman's model that boundary condition is that the interaction potential seen by the electrons beyond the sphere is identically zero. Furthermore, Liberman's model imposed charge neutrality within the ion-sphere. Exactly what boundary conditions are chosen and other imposed conditions on the system give rise to different flavors of average atom models.

The average atom model that underlies our work is pictorially depicted in Figure 1.3 and effectively follows the description developed by Liberman. Within the ion-sphere, the effective potential is generally nonzero and must be determined in the standard way through use of DFT. At the ion-sphere radius and beyond, the effective potential is forced to be zero. This imposed condition is meant to represent the screening of forces by the surrounding plasma, effectively

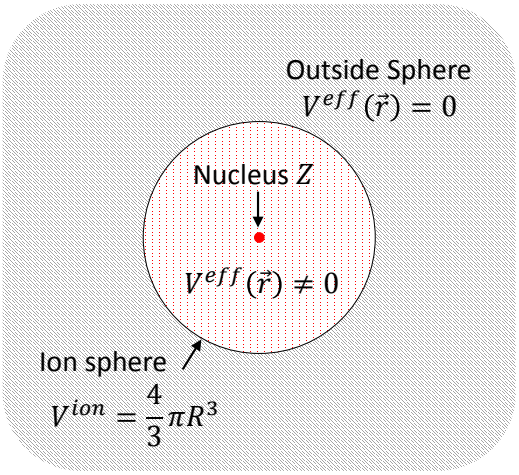

Figure 1.3: (This figure also appears in Chapter 3 of this work.) Schematic diagram of average atom physical model. Inside the ion sphere the electronic structure is determined with density functional theory. The boundary condition is that outside the sphere the effective electron-nucleus potential is zero.

creating a quantum analog of the Debye radius. In practice this imposes the boundary condition that all electronic states must match their zero potential form (e.g. functionally spherical Bessel functions in the case of spherically symmetric potentials like ours) at the ion-sphere boundary.

Beyond the definition of the ion-sphere and the imposed perfect screening of forces outside of the sphere, our model also imposes that the average atom remain neutral, i.e. that the total charge within the ion-sphere is zero. Since this model is a statistical model meant to represent the typical ion (and associated electronic density) seen within plasma, the condition of ion-sphere neutrality is meant to be representative of the conservation of charge within the plasma as a whole. This condition adds a statistical limit that must be included in the DFT self-consistent procedure used to determine the electronic density. This is illustrated in Figure 1.4.

1.2.2 Benefits and Difficulties of Average Atom Model Calculations

The definition of the ion-sphere, the imposition of the screened, neutralizing background, the choice of boundary conditions applied to the wavefunctions, and the condition of charge neutrality within the ion-sphere are collectively what define the average atom model. Though these are relatively simple concepts to understand, the impact that they have on the details of the electronic density calculation and on the resulting physics extracted from that calculation is more complicated. This section is meant to provide a qualitative overview of both the strengths and weaknesses of average atom calculations. Far greater detail on the actual calculations, as well as results of those calculations, is presented in Chapters 2 and 3.

Without further additions to the model, the plasma environment is only accounted for through the determination of the ion-sphere radius and the choice of boundary conditions. Though this may seem crude, this simple picture of plasma screening allows for the calculation of both bound and free electronic states to consistently account for density effects within the plasma. The finite size of the average atom restricts the number of existing bound states, which is physically expected in finite density systems. Further, the consistency in how the bound and free electronic states are determined naturally gives rise to resonant structures in the continuum density of states (see Chapter 2 for more details). These resonances are large features in the

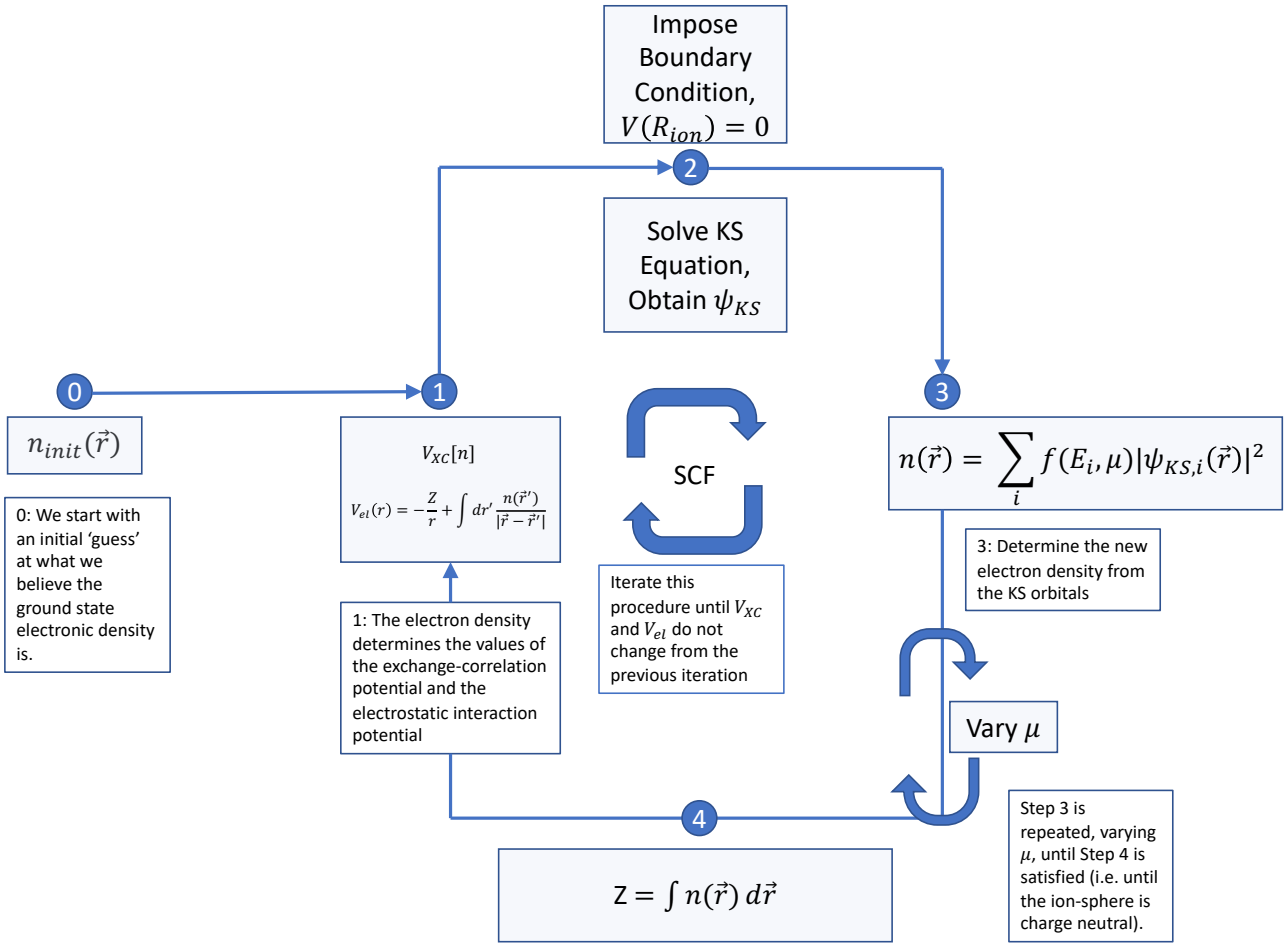

Figure 1.4: This diagram shows the iterative procedure used in order to determine the average atom electronic structure. In this diagram, the chemical potential of the electrons in the system, μ, must be varied in order to ensure that the integral of the electron density within the ion-sphere produces the same number of electrons as protons within the nucleus of the ion, Z.

density of states representing the existence of a large number free states within a small range of energies, usually centered around an energy near the ionization threshold. Effectively these so-called continuum resonances can be thought of as a bound state that was squeezed into being a tight distribution of free states by plasma density effects. Though representing these resonances accurately is a difficult computational task, they do have realistic physical meaning and the average atom model naturally gives rise to them without further additions to the underlying model.

Average atom simulations have the benefit of being computationally expedient. With only a single determination of the electronic density, most properties of interest can be simply extracted. The computational efficiency is largely due to how we treat the single average atom calculation as being a reasonable description of the plasma as a whole. A limitation of average atom models is that they are DFT-based calculations and therefore do not account for excited states and use fractional occupation values for the electronic structure. They also suffer because the Kohn-Sham eigenstates represent states of non-interacting quasiparticles (as opposed to being the true eigenstates of interacting electrons); thus the eigenvalues of these states do not correspond to the energies of actual electrons observed in nature. This limits the usefulness of average atom calculations for creating spectra directly comparable to experiment, though the models are still able to generate spectra useful for gaining insight into the impact of various physical effects on spectra. This latter point is demonstrated in showing the impact of accounting for ion correlations on the opacity spectra in Chapter 5.

Overall, average atom models allow for a fast, efficient, and physically reasonable calculation that can be used over a wide range of plasma temperatures and densities. The ability to run these simulations without the need for human input over a wide range of temperatures and densities makes average atom models ideal for generating large tables of Equation of State (EOS) data. The work shown in this dissertation represents a major step-forward in the ability of average atom models to be used to generate large tables or inform analytic fits.

1.2.3 Adaptation of Average Atom Models to Complex Applications

This section will describe some techniques which build additional physics onto an underlying average atom model. The fundamental average atom and its application to equation of state in the Tartarus model will be explained in great detail in Chapters 2 and 3, which is a standard average atom model that is improved upon by the use of a Green's function formalism as well as several other numerical techniques. The average atom model as implemented in Tartarus is capable of determining a reasonable electron density that gives good results when determining equation of state. However, as stated before, the basic average atom model only accounts for ionic correlations implicitly through the definition of the ion-sphere and the choice of boundary conditions applied at the edge of the sphere.

In order to more accurately and completely account for ion correlation within the plasma (including ion-ion and ion-electron correlations), the average atom model can be coupled to a plasma model that includes a more realistic description of the ion effects in the plasma. The next section will introduce the basics of an average atom model coupled to a two-component plasma model, the Average Atom Two Component Plasma (AA-TCP) model. This model is used to perform the work shown in Chapter 4 of this dissertation.

Statistical models such as a basic average atom and the AA-TCP model are able to determine a large number of statistical quantities of interest, but time-resolved simulations are often needed to access dynamic properties of plasmas. Molecular dynamics simulations are commonly used in classical plasma modeling and are also coupled with DFT simulations to model lower temperature warm dense matter systems. In the coming section we will introduce the Psuedoatom Molecular Dynamics (PAMD) approach, which extracts a classical pair interaction potential from the AA-TCP model and uses that to perform a molecular dynamics simulation. PAMD is used to perform the work shown in Chapter 5 of this dissertation.

Average Atom Two Component Plasma

Though the average atom model implicitly accounts for plasma density through the definition of the ion-sphere, it does not include an explicit modeling of ionic correlations. This information

is important in strongly coupled plasmas, where ion correlations can have a significant impact on many properties of the plasma. Further, the correlations between ions in the plasma is information that is accessible through x-ray Thomson scattering experiments, which provides a benchmark with which to test our models.

A function of interest when studying the plasma as a whole is the radial distribution function, $g(r)$. This function contains information on how the density changes around a reference particle (in our case, around the central ion of an average atom calculation). Effectively this function gives information on the probability of finding another particle a distance r away from the central particle. Being able to determine an ion-ion pair correlation function provides information on how the ions couple together in a system.

Though there are simple ways of approximating these correlations, to do so properly requires a quantum mechanical model for the plasma electrons that accounts for bound states of the ions as well as free electrons. Starrett and Saumon demonstrate such a model in References [27, 28, 1]. This model couples the electronic density calculation of an average atom model to a two component fluid description of the plasma. The resulting model is capable of accessing ion-ion (and ion-electron) correlations of the plasma while maintaining the influence of electronic bound states. Further, this information is obtained without the need for simulations such as molecular dynamics or path-integral Monte Carlo. The relevant data (e.g. $g(r)$, EOS, etc.) are obtained through the quantitites determined by the model itself.

The AA-TCP model is able to achieve demonstratably accurate pair correlation functions for warm to hot dense matter in a fraction of the time of competing approaches, making it preferred for the generation of large tables of data. It is able to do this in part through the definition of a pseudoatom, a neutral subsystem which allows for the separation of the electrons in the plasma into those "belonging" to one nucleus and those "belonging" to other ions in the plasma [29, 30, 31]. Though the author of this current work was not involved in the development of this model, it is used heavily in work done in Chapters 4 and 5, and we present here a basic overview of the definition of the pseudoatom for the reader's context in the coming chapters. For more information on the model, its validation, and specific results, the interested reader is referred to Reference [1].

The pseduoatom can be best defined through use of its characteristic electron density. This density is by design the electronic structure arising from the central nucleus alone. It is accessed by first performing a typical average atom calculation, whose resulting density, $n_e^{AA}(r)$, implicitly contains structure caused by the other ions within the plasma. In order to isolate the density belonging to the pseudoatom alone, we must remove the background structure caused by the ion distribution and surrounding electrons, $n_e^{ext}(r)$. This external density, $n_e^{ext}(r)$, is determined by solving the Kohn-Sham equations (or more generally whichever equation is descriptive of the electronic structure—the Kohn-Sham Schrodinger equation for nonrelativistic quantum mechanical electrons or the Thomas-Fermi equation for semiclassical electrons) without the potential influence from the central nucleus. This is done with a self-consistent approach, just as it would be for a system in the presence of the central nucleus (see Appendix B of Reference [28]). With these two densities defined, we can isolate the pseudoatom density:

$$n_e^{PA}(r) = n_e^{AA}(r) - n_e^{ext}(r) \tag{1.4}$$

where n_e^{PA} is the pseudoatom electron density.

The next important step in the calculation of the model is to isolate the so-called screening electrons from the total pseudoatom. These are the continuum electrons whose structure arises from the central nucleus. This is done by simply removing the ion's bound electronic structure from the total pseudoatom density:

$$n_e^{scr}(r) = n_e^{PA}(r) - n_e^{ion}(r) \tag{1.5}$$

where n_e^{scr} is the screening electron density and n_e^{ion} is the density of the bound states associated with the ions.

In determining n_e^{ion} there is some ambiguity in the definition of what parts of the electronic structure can be attributed as belonging to the central ion. Depending on the approached used to determine the electronic density, this structure can be determined semi-classically or in a fully quantum mechanical framework. For this work and discussion we will only focus on the fully quantum mechanical approach. From here we will provide a qualitative description of how this

ionic density is treated in our work. A more detailed mathematical description is shown in [28], and here we avoid replication of that detail for the sake of concision.

With the various electronic densities relevant to the plasma well-defined and determined with the use of reasonable, physically-informed modeling, the next step is to use those densities in a plasma fluid formalism. The two-component model of the plasma is built from the quantum version of the Ornstein-Zernike (QOZ) equations [27, 32, 33]. The two components of the plasma in this formulation are the classically treated ions (including their associated electrons) and the quantum mechanically treated electrons. For the sake of clarity and concision, the fluid equations themselves will be left out of this work, but are detailed in [28].

The fluid equations involve determining the correlations between the ions and other ions, the ions and the electrons, and the electrons and other electrons. This requires knowledge of five different correlation functions coupled together by two unique fluid equations. In order to solve this system, three additional relationships are needed.

The first is provided by approximating the electron-electron interactions as that of a so-called "jellium" model (i.e. an interacting quantum fluid of electrons in a uniform, neutralizing background of positive charge). In true plasmas with electrons forming bound states around nuclei (and thus correlating with the nuclei in a non-uniform way), the jellium model would provide a poor approximation to the electron-electron correlations. However, through the use of the pseudoatom, which allows for the definition and separation of the ions from the surrounding electrons, this jellium approximation can be applied with confidence. This approximation, though simple, does a good job of describing electron-electron correlations due to how AA-TCP defines the two components of the plasma as that of ions (i.e. nuclei and associated electrons) and electrons, as opposed to just nuclei and electrons.

The second needed relationship comes from the ion-ion closure relation, which provides a so-called bridge function to complete the definition of an effective ion-ion potential containing information on the ion-ion correlations. Application of this bridge function is a well-known approach applied in the study of liquids [34], and there are many choices for what bridge function can be used. When choosing to ignore the bridge function, you arrive at the commonly used Hypernetted-Chain (HNC) approximation. The HNC approximation is valid for plasmas

where the ion-ion correlations are relatively weak, but other choices of bridge function must be used for strongly coupled systems.

The final relationship provides information on the ion-electron correlations and is determined through use of the average atom model and pseudoatom definitions discussed previously. The screening density obtained from the average atom calculation is the necessary output from the pseudoatom calculation needed to close the quantum Ornstein-Zernike equations. The TCP model also uses the ionic distribution common to many average atom models—that of a step-function at the ion-sphere radius. For clarity a high-level overview of the algorithmic procedure used to solve this model is shown in Figure 1.5.

Pseudoatom Molecular Dynamics

Apart from static quantities (i.e. those quantities considered averaged over any fluctuations that occur in the plasma over time), dynamic information is needed for many applications. One function that contains such information is the ion-ion dynamic structure factor, $S_{ii}(k,\omega)$ (where k is the particle wavenumber and ω is the frequency associated with some external perturbation), which is a function that contains information on inter-ionic correlations and the evolution of those correlations under external influence. Accurate $S_{ii}(k,\omega)$ for systems in the warm dense regime requires a reasonable quantum mechanical description of the electrons surrounding each ion. Typically the correlations are determined via iterations of the ion positions in a molecular dynamics simulation. Importantly, the dynamic structure factor can be measured experimentally via x-ray Thomson scattering. This can provide a substantial validation of the models used to predict the plasma correlations.

The AA-TCP model generates all of the information needed to construct a pair potential that governs the interaction between the pseudoatom nuclei in the system. This potential can be used in a classical molecular dynamics simulation. This coupling of the AA-TCP model to a molecular dynamics simulation is PAMD. The pair potential can be written in terms of the quantities accessed from the AA-TCP calculation:

$$V_{pair}(k) = \frac{4\pi\bar{Z}}{k^2} + \frac{n_e^{scr}(k)^2}{\chi_e(k)} \tag{1.6}$$

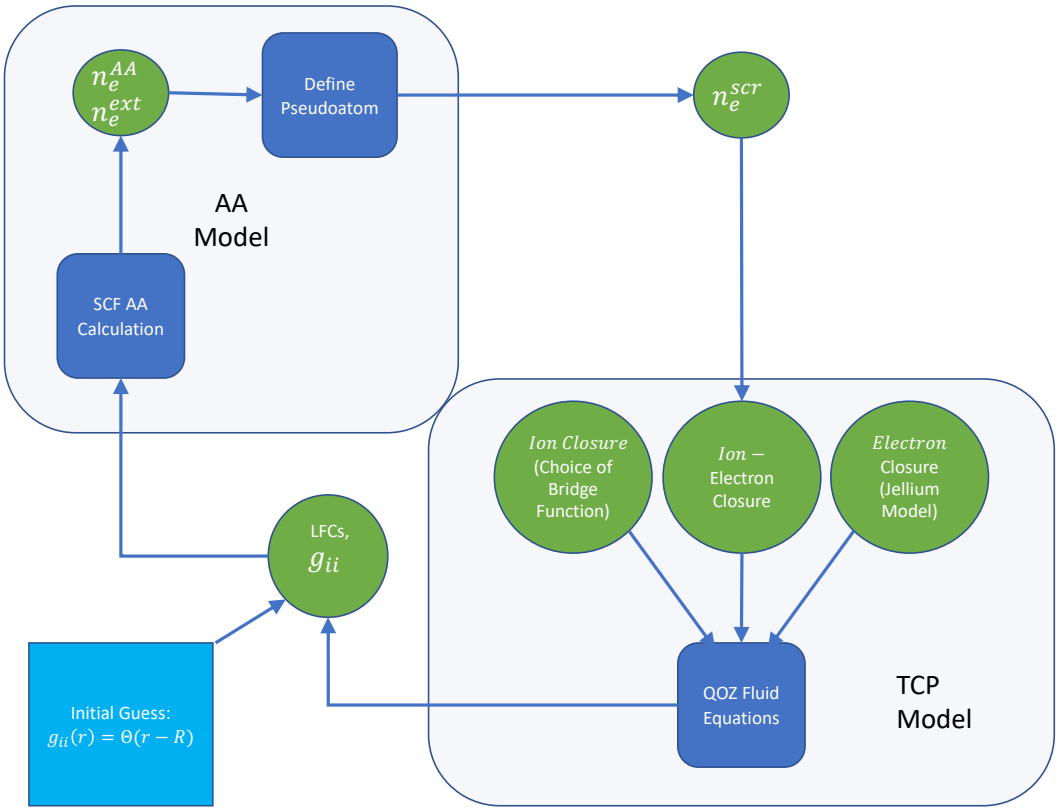

Figure 1.5: This diagram shows an overview of the general algorithm used to solve the AA-TCP model. An initial guess for the ion-ion pair distribution function, g_{ii}, as a step function at the ion-sphere radius is used to solve the AA/Pseudoatom model, which yields the screening electron density. This density, along with two other closure relations, allows for the determination of an ion-ion pair distribution function from the coupled AA-TCP model. This more informed distribution function can then be fed back into the AA calculation, and the two calculations can be iterated until converged. Starrett and Saumon showed that the g_{ii} resulting from the first iteration is largely unchanged over subsequent iterations [1].

where $\bar{Z} = \int d\vec{r}\, n_e^{scr}(r)$, χ_e is the electron response function obtained by AA-TCP, and the expression is given in Fourier space with particle wavenumber k due to the relative simplicity of the expression. Hence only the electron response and the screening potential associated with the pseudoatoms is needed to define the effective pair potential between the pseudoatoms in the plasma.

The pair potential between pseudoatom nuclei being used in the molecular dynamics simulation is why the model is named "pseudoatom" molecular dynamics, because the fictitious pseudoatoms are what are moved around in the simulation as opposed to the actual ionic nuclei. In this way PAMD constructs the plasma as existing as an assemblage of pseudoatoms. The total electron density of the plasma is obtained by PAMD through the use of the superposition approximation, which states the the plasma electron density, $n_e(\vec{r})$ (i.e. the electron density of the plasma as a whole, including all ions), is simply the sum of all of the pseudoatom electron densities:

$$n_e(\vec{r}) = \sum_i n_e^{PA}(|\vec{R}_i - \vec{r}|) \tag{1.7}$$

where the index i runs over all pseudoatoms in the simulation and $\vec{R}_i$ is the vector pointing to the nucleus of pseudoatom i. This plasma density utilizes the entirety of the pseudoatom density and therefore includes the screening electrons in the plasma.

A major strength of the PAMD simulation is that it is not limited to single-component (i.e. one atomic species) plasmas. The underlying AA-TCP method can access effective ion-ion pair potentials between ions of the same and different species. The ability to represent mixed plasmas is the main feature utilized in Chapter 5 of this work. Further, unlike other methods, PAMD is an all-electron model, meaning that it does not utilize model aspects with free or adjustable parameters. A weakness of the model is that, due to its inherent representation of the plasma as a system of pseudoatoms, it is unable to represent molecules or account for interatomic bonding.

1.2.4 Alternative Methods

Given the importance of studying dense plasma systems in the warm and hot plasma regimes, there are understandably many different approaches to modeling and simulating these systems. Ideally one would be able to use a fully *ab initio* approach to study these systems, but the complexity of these systems makes that currently impossible to do over a wide thermodynamic range. Here we will briefly discuss several methods that can give results generally considered to be of higher fidelity than the average atom based approaches discussed in this work, but these methods have a limited range of temperatures and densities, and typically require significantly more computational resources to complete. These methods are used here as benchmarks with which to check our model against.

DFT-MD

Kohn-Sham Density Functional Theory Molecular Dynamics (KS-DFT-MD) is a powerful simulation tool that uses the power of an *ab initio* electronic structure calculation that accounts for the interactions between ions in the plasma. This intensive type of calculation determines the inter-ionic forces at each timestep of the molecular dynamics simulation using DFT, and as such is presumed to capture the response of the bound and continuum electrons to plasma dynamics (at least in the case of a fully quantum mechanical calculation). The issue with this approach is that it scales very poorly in terms of computational efficiency as both the number of ions increases and as the temperature increases. This limits the approach to being used for low temperature systems. Further, in order to reduce the computational time, plane-wave DFT-MD simulations also apply pseudopotentials to the calculation of the electron-nuclei interactions. Pseudopotentials effectively limit the number of electrons that are actively treated by the DFT calculation, but this introduces a parameterization into the simulation that could unwittingly produce errors in the results.

Another DFT based approach is the Orbital Free Molecular Dynamics (OFMD) simulation. This type of simulation does not explicitly perform calculations using orbitals, but is still able to capture much of the important physics needed to describe the inter-ionic forces for the

molecular dynamics simulation. Though less physically accurate than QMD, OFMD does not scale poorly with increasing temperatures. However it still requries signficant computational resources and therefore faces limitations when performing simulations with many ions and large simulation "boxes" (the spatial extent of the simulation). OFMD is limited by the use of approximate kinetic energy functionals, which means there are no discrete bound states in these simulations [35, 36].

Path Integral Monte Carlo

The Path Integral Monte Carlo (PIMC) method uses a quantum mechanical description of both the nuclei and electrons, and the path integral formulation of statistical mechanics to describe the evolution of the plasma [37, 38]. Monte Carlo sampling is used to sample many different paths within the plasma. Though this approach is an ostensibly *ab initio* model, there are some approximations (e.g. the assumption of Boltzmann-like particles which leads to ignoring quantum mechanical exchange effects) that limit the range of the model's usefulness. Further, the well known Fermion sign problem requires the introduction of an approximation to the electron density matrix used in the calculations. PIMC simulations do a very good job of simulating plasmas at high temperatures (i.e. when $k_B T \gg E_F$), but the method scales poorly in terms of efficiency and accuracy at low temperatures and is limited to the calculation of equation of state information at this point in time.

1.3 Outline of Chapters

This section will serve to outline the chapters in this dissertation along with a brief description of some of the quantities of interest discussed in those chapters. With the exception of this introductory chapter and Chapter 6, the chapters of this work are directly adapted from papers published in peer reviewed journals. As such there will be slight overlap of the information presented in the introductions of those works, as is often necessary for publications within the same general field of study.

1.3.1 Chapter 2 - Tartarus Model Description

Chapter 2 focuses on the description of the Tartarus model, an average atom model that includes both a nonrelativistic and a relativistic description of the average atom electronic density based on the solution of the Dirac equation. Though the underlying physical model used in Tartarus does not deviate significantly from other average atom models, Tartarus is able to overcome many of the computational and algorithmic difficulties inherent in average atom calculations through use of a Green's function technique to study weakly bound and significantly structured continuum electrons, and an orbital based technique for higher energy continuum electrons and deeply bound core electrons. This model is applied in Chapter 2 to the study of the equation of state, which is validated through determination of the shock Hugoniot curve (a collection of EOS points characteristic of a system under an ideal shock). Chapter 2 mainly serves as a presentation of the relativistic theory of the Green's function average atom model, which allowed for demonstrating new results for heavier elements where relativistic effects are important.

My contribution to this work included developing the relativistic Green's function average atom formalism, which involved deriving the relativistic expressions needed to perform the self-consistent density calculation and the thermodynamic quantities extracted from the converged average atom system. Further, I took the proof-of-concept code used to generate results for the nonrelativistic Green's function average atom and adapted it into a large code package which could perform both relativistic and nonrelativistic calculations with analogous algorithmic form. This involved significant algorithm development, including schemes for handling the often numerically challenging small component of the Dirac wavefunction and for obtaining the Green's function at energies with large imaginary components. Finally I developed and implemented the hybrid orbital scheme in both relativistic and nonrelativistic modes of the code, which allowed for using the more easily obtainable continuum orbitals at high electron energies where the Green's function approach is no longer needed. The hybrid approach represents a significant improvement in robustness and computational efficiency at certain plasma conditions, but introduces no approximations to the model. Chapter 2 was published in High Energy Density Physics in 2017 [39].

1.3.2 Chapter 3 - Tartarus Code Package

Though Chapter 2 provides an overview of the underlying model used in Tartarus, that work was published after a functional code was formed that provided access to new results and demonstrated the overall concept that the hybrid relativistic Green's function-orbital approach worked. Chapter 3 goes into detail on the theoretical formulation of the model but also describes the development, refinement, and application of the complete Tartarus code package. After the work presented in Chapter 2, there were many improvements made to the algorithmic approaches used in Tartarus. These refinements include the implementation of a stable, fast convergence accelerator for the self-consistent field calculations. With a robust, well-tested code package, we were able to show a wide range of results as well as detail the computational efficiency of the Tartarus model at various plasma conditions.

My contributions to this work were in clarifying the relativistic theory (which I developed and initially presented in Chapter 2), developing refined algorithms for energy contour generation that greatly enhanced the robustness of the code, and assisted in both the theoretical and algorithmic implementation of the thermodynamic calculations that followed the converged average atom calculation. Chapter 3 was published in Computer Physics Communications in 2018 [40].

1.3.3 Chapter 4 - Mean Force Scattering Potential

Chapter 4 describes the utilization of the AA-TCP model to generate a mean-force (effective) potential which is used to incorporate information about the ionic structure into the calculation of the electrical conductivity and subsequently the opacity. The main driving force of this work was to determine how relevant ionic structure is to the opacity in the thermodynamic ranges relevant to recent opacity experiments.

My contributions to this work involved using the mean-force potential as a scattering potential in an average atom Kubo-Greenwood calculation of electrical conductivity and opacity. This required extensive data analysis, as the goal of this work was to assess the importance of ion correlations on radiative properties of plasmas. Due to warm and hot dense systems being

difficult to characterize generally, the major challenge here was determining at what plasma conditions ion correlations are important and in what ways the spectrum is affected by those correlations. In the end I was able to develop an adequate qualitative explanation of what aspects of radiative spectra are changed through the introduction of ion correlations as well as generate new data with ion correlations incorporated into the spectra. Chapter 4 was published in High Energy Density Physics in 2019 [41].

1.3.4 Chapter 5 - Dynamic Structure of Plasma Mixtures

Chapter 5 applies the PAMD method discussed previously to study the dynamic structure of mixed plasmas. The main focus of this chapter is the determination of $S(k, \omega)$ (discussed previously in the introduction of the AA-TCP model) for warm dense binary mixtures (i.e. plasmas composed of two different atomic species). This work demonstrated the first observance within simulations of the so-called "fast sound" phenomenon in warm dense plasmas. Chapter 5 further illustrates the strength of the average atom models and the methods built upon them to access highly complex information with reasonable fidelity.

My contribution to this work was to develop a code which could extract $S(k, \omega)$ from the PAMD simulation outputs. Further, I determined the structure factors relevant to ionic mixtures and analyzed that data to show the fast sound phenomenon. Chapter 5 was published in Physical Review E in 2015 [42].

1.3.5 Chapter 6 - Time-Dependent DFT and the Linear Response of Plasmas

Chapter 6 describes the ongoing work of the author in applying time-dependent DFT (TD-DFT) techniques to study the linear response of plasmas. This is done by studying the dynamic response of the electrons in an average atom model to a perturbing field (in the form of a single photon). Though TD-DFT has had extensive use in the study of solid state systems as well as neutral, cold gases, it has had far less use in the study of finite-temperature, dense systems. The work presented in Chapter 6 is the author's adaptation of previous attempts to apply TD-DFT to average atom systems and use the results to access electrical conductivity and opacity. This

work is still ongoing, and Chapter 6 will present the progress made so far including insights into the numerical challenges involved in implementing a TD-DFT calculation.

1.3.6 Conclusion and Appendices

This dissertation is finalized in Chapter 7 with a conclusive overview of the results presented in Chapters 2–6. Further information on the mathematical details used to construct the TD-DFT formalism can be found in Appendix A.

Chapter 2

Tartarus: A relativistic Green's function quantum average atom code

2.1 Abstract

A relativistic Green's Function quantum average atom model is implemented in the Tartarus code for the calculation of equation of state data in dense plasmas. We first present the relativistic extension of the quantum Green's Function average atom model described by Starrett [43]. The Green's Function approach addresses the numerical challenges arising from resonances in the continuum density of states without the need for resonance tracking algorithms or adaptive meshes, though there are still numerical challenges inherent to this algorithm. We discuss how these challenges are addressed in the Tartarus algorithm. The outputs of the calculation are shown in comparison to PIMC/DFT-MD simulations of the Principal Shock Hugoniot in silicon. We also present the calculation of the Hugoniot for silver coming from both the relativistic and nonrelativistic modes of the Tartarus code.

2.2 Introduction

There is a need for accurate calculation of equation of state (EOS) data for plasmas in a wide range of temperature and densities stemming from the study of astrophysical and laser generated plasmas. These dense plasmas exist at such high densities and temperatures that neither perturbative plasma or atomic physics approaches are able to fully describe the system. Average atom (AA) models attempt to account for the plasma environment while retaining a reasonable description of the electronic structure. These density-functional-theory-based average

atom models allow for the calculation of plasma thermodynamic properties at a wide range of temperature and density points without a large computational expense.

There are versions of AA models that do not account for the orbital nature of the electrons [5], but this lack of detail on the electronic structure leads to inaccuracies and loss of features in the resulting EOS calculations. AA models that account for orbital structure provide more physically accurate descriptions of the plasma but have long suffered from numerical challenges [26, 25, 44, 45, 28]. Chief among these difficulties has been the robust accounting for of resonance states in the continuum density of states. These so-called pressure ionized states are narrow in width and highly peaked, making them very important to the calculation of the electron structure. Robust and sophisticated algorithms have been developed to deal with these resonances by tracking their location and densely populating the integration grid in their vicinity [46].

In order to circumvent the numerical complexity and computational time added to fully treat the resonances in the continuum density of states, Starrett developed a nonrelativistic Green's function based AA model that utilizes the properties of Green's function to broaden any features in the density of states, which can include bound state features as well [43]. The need to carry out EOS calculations for heavy elements (high Z) requires a fully relativistic treatment of the electrons. In this chapter, we outline the theory needed to transition from the nonrelativistic to the relativistic formalism and the numerical implementation of that model in the form of the Tartarus code. Though the main qualitative features of the model remain unchanged, the transition is not trivial. We especially focus on the details of the calculation of thermodynamic properties of the plasma using this formalism. Since the typical orbital approaches work well for higher angular momentum states where resonances do not occur, Tartarus uses a hybrid approach with the Green's function calculation applied to the lower angular momentum states, where resonances are prevalent, and orbital calculations used elsewhere.

As a means of validation, we present the consistency of the plasma pressure calculated by Tartarus via the virial theorem and numerical differentiation of the free energy. This shows the results are consistent with what has been seen in previous AA calculations [47]. Though Tartarus is able to quickly and robustly generate EOS data for a wide range of plasma species and

conditions, the underlying AA model is not without approximations. More physically representative models use Kohn-Sham Density Functional Theory Molecular Dynamics (DFT-MD) to capture the electronic structure and ionic positions [48, 49, 50]. These methods lead to physically accurate results, but require simulations involving many separate atomic sites iterated over many time steps, with computational times scaling sharply with the temperature. This makes these calculations computationally expensive and unsuited for the generation of large sets of EOS data. Another high fidelity modeling approach is Path Integral Monte Carlo (PIMC) [37, 2]. This method is also very expensive computationally, and computation time increases as temperature is lowered. These methods provide benchmark calculations with which to compare the results of less computationally expensive calculations. In the last part of the chapter we show the comparison of a shock Hugoniot generated from a Tartarus EOS with simulations done using DFT-MD/PIMC calculations. This illustrates both the strengths and physical inaccuracies of the AA model. Tartarus in its current version is well tested for generating EOS data of plasmas ranging from 0.1 eV to 40,000 eV and for densities ranging from one-fifth of solid density to well over eight times solid density. Hartree atomic units ($\hbar = m_e = e = 1$) are used throughout the rest of the chapter unless otherwise noted.

2.3 Theory

2.3.1 Average Atom Model and DKS-DFT Orbitals

The average atom model as it is implemented in this work approximates the typical atom in a plasma with a sphere of radius $R = (\frac{3}{4\pi n_{ion}})^{\frac{1}{3}}$ which defines the atomic sphere volume, V, where n_{ion} is the ion number density of the plasma, and has at its center a nucleus of charge Z. Outside of the atomic sphere the effective potential seen by the electrons is zero. The sphere is required to be charge neutral.

Inside the sphere the electron density is determined using finite temperature relativistic density functional theory [22, 51, 52]. The Dirac-Kohn-Sham (DKS) electron orbitals are defined by the eigenvalue equation

$$\hat{H}_D \vec{\psi}_\epsilon = \epsilon \vec{\psi}_\epsilon \tag{2.1}$$

where ϵ is the electron energy. The DKS-DFT Hamiltonian, H_D, is defined as

$$\hat{H}_D = \hat{T} + (\hat{\beta} - I_4)mc^2 + \hat{V}^{eff} \tag{2.2}$$

where $\hat{T}$ is the kinetic energy operator defined as

$$\hat{T} = c\vec{\alpha} \cdot \vec{p} \tag{2.3}$$

with

$$\alpha = \begin{bmatrix} 0 & \vec{\sigma} \\ \vec{\sigma} & 0 \end{bmatrix} \tag{2.4}$$

Here $\vec{\sigma}$ are the Pauli matrices, $\vec{p}$ is the electron momentum, I_j is the identity matrix of size j, $\hat{\beta}$ is defined as

$$\hat{\beta} = \begin{bmatrix} I_2 & 0 \\ 0 & -I_2 \end{bmatrix} \tag{2.5}$$

and $\hat{V}^{eff}$ is the effective DKS potential operator, $\hat{V}^{eff} = V^{eff}(\vec{r})I_4$, with $V^{eff}(\vec{r})$ defined as

$$V^{eff}(\vec{r}) = (V^{el}(\vec{r}) + V^{xc}(\vec{r})) \tag{2.6}$$

where the electrostatic part is

$$V^{el}(\vec{r}) = -\frac{Z}{r} + \int_V d\vec{r}' \frac{n_e(\vec{r}')}{|\vec{r} - \vec{r}'|} \tag{2.7}$$

and the exchange and correlation part is

$$V^{xc}(\vec{r}) = \frac{\delta F^{xc}}{\delta n_e(\vec{r})} \tag{2.8}$$

with F^{xc} as the exchange and correlation free energy.

The DKS-DFT orbitals are vectors of size 4, commonly written as a two component vector,

$$\vec{\psi}_\epsilon = \begin{bmatrix} \vec{\psi}_\epsilon^A \\ \vec{\psi}_\epsilon^B \end{bmatrix} = \sum_{\kappa,m} \begin{bmatrix} g_\kappa(r,\epsilon)\vec{\chi}_{\kappa,m}(\hat{r}) \\ if_\kappa(r,\epsilon)\vec{\chi}_{-\kappa,m}(\hat{r}) \end{bmatrix} \tag{2.9}$$

where κ is the relativistic angular momentum quantum number, m is an index representing both the magnetic and spin quantum numbers, $\vec{\chi}_{\kappa,m}(\Omega)$ are the well known spherical spinors, $\vec{\psi}_\epsilon^A$ and $\vec{\psi}_\epsilon^B$ are the big and small components of the wavefunction, respectively, and g_κ and f_κ are the big and small components of the radial wavefunction, respectively, which are the solutions of the radial Dirac equations:

$$\begin{aligned} [\epsilon - V^{eff}(r)]g_\kappa(r) + \hbar c\frac{1}{r}\{\frac{d}{dr} - \frac{\kappa}{r}\}(rf_\kappa) = 0 \\ -\hbar c\frac{1}{r}\{\frac{d}{dr} + \frac{\kappa}{r}\}(rg_\kappa(r)) + [\epsilon - V^{eff}(r) + 2mc^2]f_\kappa(r) = 0 \end{aligned} \tag{2.10}$$

We can take advantage of the spherical symmetry in the model to analytically reduce the calculations of interest. In the orbital formalism, the radial electron number density can then be expressed as [46]

$$n_e(r) = \int_{-\infty}^{\infty} d\epsilon f(\epsilon,\mu) \sum_\kappa 2|\kappa|[g_\kappa^2(r,\epsilon) + f_\kappa^2(r,\epsilon)] \tag{2.11}$$

where $f(\epsilon,\mu)$ is the Fermi-Dirac occupation factor with chemical potential μ, and the integral from $-\infty$ to 0 reduces to a summation over the discrete bound states.

In order to solve Equations 2.1-2.11, we use a self-consistent field (SCF) scheme. This requires repeated evaluation of the electron density, which consists of integration over the continuum energy spectrum as well as a search for bound states at negative energies. For an orbital based calculation, this requires resonance tracking for continuum states and a dense energy grid in order to resolve sharp features in the integrand, adding considerable computational time and complexity to the calculation. The Green's function (GF) approach avoids this burden by ensuring that the functions to be integrated are smooth and vary slowly in energy. Surprisingly, the

integrals can be extended to negative energies, thus including bound states, with the integrand remaining smooth.

2.3.2 Green's Function Formalism

The transition to the Green's function formalism in the average atom model is straightforward. The SCF procedure remains unchanged, but now the electron density is calculated via the GF approach by

$$n_e(r) = -\frac{1}{\pi}\Im \int_{-\infty}^{\infty} dz f(z,\mu) TrG(r,r,z) \tag{2.12}$$

where $z = \epsilon + i\gamma$ is the complex energy (with $\gamma = 0$ for the integration in Equation 2.12), Tr denotes the trace operation, and $G(r,r,z)$ is the single-site, one-electron Green's function with spherical symmetry already applied. This is exactly the same expression as is used in the nonrelativistic formalism [43], and only the form of the GF changes for the relativistic model. The spherically symmetric trace of the relativistic GF can be written as

$$\begin{aligned} TrG(r,r,z) &= -ip(1+\frac{z}{2mc^2}) \\ &\times \sum_{\kappa} \frac{2|\kappa|}{4\pi} [g_\kappa^R(r) g_\kappa^I(r) + f_\kappa^R(r) f_\kappa^I(r)] \end{aligned} \tag{2.13}$$

where $p = \sqrt{2z(1+\frac{z}{2mc^2})}$ is the magnitude of the momentum and the superscripts R and I refer to the regular and irregular solutions of the radial Dirac-Kohn-Sham equations, respectively, and the, in general complex, energy dependence of the solutions is left implicit. The regular solution is obtained by integrating outward from the origin and diverges at infinity, whereas the irregular solution is obtained by integrating inward from the atomic sphere boundary and diverges at the origin [53].

Calculating the GF requires both the regular and irregular solutions of the radial DKS equations, which on the face of it complicates the problem compared to the orbital approach. However, the GF is analytic in the complex plane, allowing us to create a complex contour of integration for the energy. As described in reference [43], the advantage to the GF method is that integrations can be calculated in the complex plane where sharp resonances and bound

states are broadened by an amount of our choosing. The expression for the electron density remains unchanged from the nonrelativistic model [43]:

$$\begin{aligned} n_e(r) = \frac{1}{\pi}\Im \int_C dz f(z,\mu) TrG(r,r,z) \\ + 2k_B T \Re \left\{ \sum_j TrG(r,r,z_j) \right\} \end{aligned} \tag{2.14}$$

where the integration along the contour, C, is taken in the counter-clockwise direction, T is the plasma temperature, and $j = 1, 2, \ldots, N_M$, where N_M is the number of matsubara poles enclosed by the contour, which are defined at energies $z_j = \mu + (2j-1)\pi k_B T$. Another quantity of interest that remains unchanged from the nonrelativistic model is the electronic density of states (DOS):

$$\chi(z) = -\frac{1}{\pi}\Im \int_V d\vec{r} TrG(r,r,z) \tag{2.15}$$

The calculation of $n_e(r)$ with equation 2.14 instead of equation 2.11 is the only change required to solve the AA model with GFs instead of orbitals. All other parts of the model remain unchanged. In particular we note that the EOS expressions are unchanged in the transition to the GF model.

2.3.3 Thermodynamic Quantities

Perhaps the main purpose for implementing this formalism is to calculate quantities needed for equation of state data. The general GF forms of these quantities, namely the internal energy and electron pressure, are analogous to their forms in the orbital representation. Here we start by presenting the orbital representations for the theoretical expressions, after which the transition to the GF representation will be much clearer.

A useful quantity needed for both the internal energy and pressure calculations is the expectation value of the kinetic energy operator, $\hat{T}$, namely

$$\langle \hat{T} \rangle_{\psi_\epsilon} = \int_V d\vec{r} [(\epsilon - V^{eff}(r))\psi_\epsilon^\dagger \psi_\epsilon + 2mc^2 \psi_\epsilon^{B\dagger} \psi_\epsilon^B] \tag{2.16}$$

where the dagger indicates Hermitian conjugation and the integration over $d\vec{r}$ is shorthand for an integration over the atomic sphere of volume V.

The electron kinetic contribution to the internal energy [54, 47], U_{ke}, is

$$\begin{aligned} U_{ke} &= \int_{-\infty}^{\infty} d\epsilon f(\epsilon,\mu) \int_V d\vec{r}\psi_\epsilon^\dagger \hat{H}_0 \psi_\epsilon \\ &= \int_{-\infty}^{\infty} d\epsilon f(\epsilon,\mu)[\langle\hat{T}\rangle_{\psi_\epsilon} - 2mc^2 \int_V d\vec{r}\psi_\epsilon^{B\dagger}\psi_\epsilon^B] \\ &= \int_{-\infty}^{\infty} d\epsilon f(\epsilon,\mu) \int_V d\vec{r}[(\epsilon - V^{eff}(r))\psi_\epsilon^\dagger\psi_\epsilon] \\ &= \int_{-\infty}^{\infty} d\epsilon f(\epsilon,\mu)\chi(\epsilon)\epsilon - \int_V d\vec{r}V^{eff}(r)n_e(\vec{r}) \end{aligned} \tag{2.17}$$

where $\hat{H}_0 = \hat{H}_D - \hat{V}^{eff}$ is the Hamiltonian of free states and ψ_ϵ are the eigenfunctions of $\hat{H}_D$, and where we have used the orbital form of the DOS

$$\chi(\epsilon) = \int_V d\vec{r}\psi_\epsilon^\dagger\psi_\epsilon \tag{2.18}$$

and Equation 2.11.

The pressure can be obtained through the virial theorem, where it is given as [47, 55]

$$P_{vir} = \frac{n_{ion}}{3}(\mathcal{T} + F_{el}) + P_{xc} + P_{ion} \tag{2.19}$$

where F_{el} is the electrostatic contribution to the free energy, and P_{xc} is the exchange and correlation contribution to the pressure, defined respectively as

$$F_{el} = \frac{1}{2}\int_V d\vec{r}[V^{el}(\vec{r}) - \frac{Z}{r}]n_e(\vec{r}) \tag{2.20}$$

$$P_{xc} = n_{ion}[-F^{xc} + \int_V d\vec{r}n_e(\vec{r})V^{xc}(\vec{r})] \tag{2.21}$$

P_{ion} is the ideal ion contribution to the pressure, and $\mathcal{T}$ is defined by

$$\begin{aligned}\mathcal{T} &= \int_{-\infty}^{\infty} d\epsilon f(\epsilon,\mu)\langle\hat{T}\rangle_{\psi_\epsilon} \\ &= \int_{-\infty}^{\infty} d\epsilon f(\epsilon,\mu)\epsilon\chi(\epsilon) + \int_V d\vec{r}[-V^{eff}(r)n_e(\vec{r}) + 2mc^2 n_e^B(\vec{r})]\end{aligned} \tag{2.22}$$

where we have defined $n_e^B(\vec{r}) = \int_{-\infty}^{\infty} d\epsilon f(\epsilon,\mu)\psi_\epsilon^{B\dagger}\psi_\epsilon^B$ as the contribution of the small component to the electron density.

With the thermodynamic quantities of interest now expressed in terms of the DOS and the electron density, the transition to the GF formalism is straightforward. The electron density can be calculated from the GF according to Equation 2.14, and the DOS can be replaced with its complex energy-dependent form in a way that is analogous to the transition from Equation 2.12 to Equation 2.14, giving us our final forms for the kinetic contribution to the internal energy and $\mathcal{T}$:

$$\begin{aligned}U_{ke} &= \int_C dz f(z,\mu)z\chi(z) \\ &+ 2k_BT\Re\left\{\int_V d\vec{r}\sum_j z_j TrG(r,r,z_j)\right\} - \int_V d\vec{r}V^{eff}(r)n_e(\vec{r})\end{aligned} \tag{2.23}$$

$$\begin{aligned}\mathcal{T} &= \int_C dz f(z,\mu)z\chi(z) + 2k_BT\Re\left\{\int_V d\vec{r}\sum_j z_j TrG(r,r,z_j)\right\} \\ &+ \int_V d\vec{r}[-V^{eff}(r)n_e(\vec{r}) + 2mc^2 n_e^B(\vec{r})]\end{aligned} \tag{2.24}$$

where n_e^B is calculated in the same way as n_e is determined in Equation 2.14, but using the lower-component Green's function, G^B, in place of the the full Green's function, whose trace is defined as

$$TrG^B(r,r,z) = -ip(1+\frac{z}{2mc^2})\sum_\kappa \frac{2|\kappa|}{4\pi} f_\kappa^R(r)f_\kappa^I(r) \tag{2.25}$$

The relativistic GF formalism must of course reduce to the nonrelativistic formalism at small energies (or when one takes the limit as $c \to \infty$), and this must be true of the thermodynamic quantities as well. The form of the kinetic contribution to the internal energy does not change from the relativistic to the nonrelativistic case, so long as the appropriately calculated DOS and electron density are used in each case. However, for the case of the pressure, the limiting behavior is not so obvious.

Using the radial Dirac equations, one can determine a relationship between the large and small component of the wavefunction. The resulting expression is

$$2mc^2\psi_\epsilon^{B\dagger}\psi_\epsilon^B = [\epsilon - V^{eff}(r)](\psi_\epsilon^{A\dagger}\psi_\epsilon^A - \psi_\epsilon^{B\dagger}\psi_\epsilon^B) \tag{2.26}$$

When it is noted that ψ_ϵ^B becomes negligibly small compared to mc^2 and $\psi_\epsilon^\dagger\psi_\epsilon \approx \psi_\epsilon^{A\dagger}\psi_\epsilon^A$ in the nonrelativistic limit, we then see that

$$\begin{aligned}(\mathcal{T})_{nonrel} =& 2\int_C dz f(z,\mu) z\chi(z) + 4k_B T\Re\left\{\int_V d\vec{r}\sum_j z_j TrG(r,r,z_j)\right\} \\ &- 2\int_V d\vec{r}V^{eff}(r)n_e(\vec{r}) = 2(\mathcal{T})_{relativistic}\end{aligned} \tag{2.27}$$

which then provides the usual nonrelativistic expression when applied to Equation 2.19 [47, 55].

2.4 Numerical Details

2.4.1 Wavefunction Normalization, Complex Spherical Bessel Functions and Choice of Contour

Though the GF approach circumvents numerical issues that are present in orbital-based average atom implementations, there are still some numerical challenges that must be addressed. The radial DKS equations are normalized to free particle solutions at the sphere boundary, $r = R$ [53, 56]:

$$R_\kappa(R) \quad = \quad \begin{bmatrix} g_\kappa^R(R) \\ if_\kappa^R(R) \end{bmatrix} \quad = \quad \begin{bmatrix} j_l(pR) - iph_l(pR)t_l \\ \frac{ipcSgn(\kappa)}{z+2mc^2}(j_{\bar{l}}(pR) - iph_{\bar{l}}(pR)t_l) \end{bmatrix} \tag{2.28}$$

$$H_\kappa(R) = \begin{bmatrix} g_\kappa^I(I) \\ if_\kappa^I(R) \end{bmatrix} = \begin{bmatrix} h_l(pR) \\ \frac{ipcSgn(\kappa)}{z+2mc^2}h_{\bar{l}}(pR) \end{bmatrix} \tag{2.29}$$

where j_l is the spherical Bessel function, h_l is the spherical Hankel function, t_l is the t-matrix common in scattering problems (which is solved for during the normalization procedure), l is the angular momentum quantum number, and $\bar{l} = l - sgn(\kappa)$, where sgn returns the sign of the argument. Where in the nonrelativistic case, normalization involves matching of the solutions and their derivatives at the atomic sphere boundary [43, 53], the matching of the relativistic two-component radial solutions with their free particle counterparts provides the necessary number of equations for normalization, i.e. the derivatives are not needed.

This boundary condition means that we must evaluate the spherical Bessel functions at the complex argument pR. We have used the complex spherical Bessel function routine by Kodama [57]. The calculation of the Bessel functions suffers from numerical problems when the imaginary part of the argument is large. The imaginary part of the momentum is introduced when there is a negative real energy (i.e. bound states) and when we use a complex energy along the contour. Furthermore, the additional factor of R in the argument exacerbates the issue for large atomic spheres (corresponding to lower density plasmas). This makes choosing a general contour generation scheme difficult. Tartarus employs a scheme consistent with that of Reference [43], with the contour generated again at each step of the SCF procedure. This is done to ensure that no bound states are missed from one iteration to the next as significant shifts in the eigenvalues of these states can occur when the potential changes dramatically over the iterations. These shifts are mostly significant at higher temperatures and for heavier elements.

2.4.2 High Angular Momentum States

The limitations of the complex Bessel function routine become more severe for higher angular momentum states. In order to reduce the number of partial states that must be accounted for, and thus reduce the maximum angular momentum l_{max} considered in Equation 2.13, we implement a scheme for calculating the continuum electron density common in average atom models [58]. This method is described by the following expression:

$$n_{ctm}(\vec{r}) = \sum_{l=0}^{\infty} n_l(\vec{r}) \approx \sum_{l=0}^{l_{max}} [n_l(\vec{r}) - n_l^0(\vec{r})] + n_e^0 \tag{2.30}$$

where n_{ctm} is the desired continuum electron density, which we define as the electron density due to electrons with energies greater than ϵ_{min} (see Reference [43]), n_l is the partial contribution to the electron density coming from the lth term of the implicit sum in Equation 2.14, n_l^0 is the partial contribution for free particles, and n_e^0 is the free particle electron density, which can be efficiently calculated using the relativistic Fermi integrals [58]. The difference between the calculated contribution and the free particle contribution to the electron density is calculated at each value of l (noting that κ can be considered as a sum over spin and angular momentum states), and when this difference becomes smaller than some numerical tolerance, we no longer increase l, thus defining an l_{max}. The remaining partial states that are not considered directly are accounted for by adding the analytical value for the total free contribution to the electron density [58]. This procedure is illustrated in Figure 2.1.

In order to determine n_e^0 at specific plasma conditions, the relativistic Fermi integrals must be carried out. These integrals have the form

$$F_n = \int_0^{\infty} dx \frac{x^n \sqrt{1+\beta x}}{e^{x-\eta}+1} \tag{2.31}$$

where $\beta = \frac{k_B T}{mc^2}$ and $\eta = \frac{\mu}{k_B T}$. The routine used to calculate these integrals is found in Reference [59].

Besides the issue with normalization at the atomic sphere boundary, higher l states can also cause issues with the calculation of the irregular solution $H_\kappa(r)$ needed to construct the GF. The

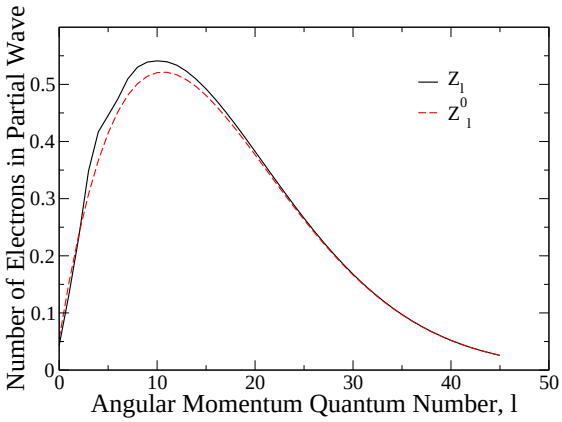

Figure 2.1: Comparison of the number of electrons in each calculated partial wave, $Z_l = \int_V n_l d\vec{r}(\vec{r})$, for both the numerically determined waves (Z_l) and the known free waves (Z_l^0) in aluminum at solid density and 1000 eV.

irregular solution requires integrating inward from the sphere boundary and is divergent at the origin, thus the solution is prone to numerical instability when the value at the boundary is large. A practical solution to this issue is to simply use the orbital expressions for the high angular momentum states. We can safely use a fixed energy grid for these states if we switch from the GF approach to orbitals at large l (we use $l = 30$) since resonance states do not appear for those high angular momentum states for plasma conditions in which we are interested.

It is worth noting again that since the GF method introduces no additional approximations, this composite scheme results in the same answer as either a full GF method with numerical issues resolved or a full orbital method with resonance tracking and adaptive grids.

2.4.3 Calculation Speed

The length of time that a calculation takes depends on plasma temperature, density, and element. As the plasma becomes more degenerate (i.e. at higher densities and lower temperatures) the calculation time generally reduces. At very high temperatures we find that the calculation time further reduces due to a combination of the improved accuracy of the initial guess (Thomas-Fermi model) and the use of Equation 2.30.

As with all numerical calculations, the accuracy and stability of the results is highly dependent on the numerical parameters chosen for the simulation. In this calculation the number of points in the spatial grid, the energy grid, and the convergence tolerance for the SCF scheme are the main parameters affecting the speed of any given calculation. For a consistent and robust choice of parameters (2000 radial grid points and 412 points in the energy contour), the calculation times for simulating an aluminum average atom plasma at solid density (2.7 g/cm^3) are 13 m 46 s, 21 m 18 s, 18 m 53 s, 11 m 43 s, and 9 m 0 s for a 5 eV, 100 eV, 500 eV, 1000 eV, and 5000 eV temperature plasma. These individual calculations could be carried out in a much shorter time with no loss of accuracy by reducing grid resolution, but the parameters used in the previous examples would ensure convergence of the calculation for all temperatures and densities within the code's intended usage, thus allowing for the code to run without manual adjustment of the parameters in different regions of the equation of state.

2.5 Results

2.5.1 Thermodynamic Consistency

The virial expression for the electron pressure was given by Equation 2.19. The pressure can also be obtained through a simple numerical differentiation of the Helmholtz free energy with respect to volume at constant temperature:

$$P_{thermodynamic} = -\left.\frac{\partial F}{\partial V}\right|_T \tag{2.32}$$

We use a comparison of these two pressures as a means of validating the calculation and determining where the model generates the least trustworthy results. For aluminum, we see in Figure 2.2 thermodynamic consistency in agreement with Reference [47], which shows that the model becomes less reliable at lower temperatures. The same trend is seen for silicon, as the poor consistency between the two pressures disappears at higher temperatures. This unreliability at low T is due to Friedel oscillations which extend outside the ion sphere and are thus not treated correctly [58, 47]. These oscillations are damped at higher temperatures. We note that there is no known thermodynamically consistent ion-in-a-sphere model [60]. The VAAQP model solves this issue, reconciling the thermodynamic consistency between the two pressures at low temperatures, by correctly accounting for the plasma outside the sphere. There is no obvious reason why the Green's function approach described here could not be adapted to the VAAQP model [47]. In all of our calculations we have used zero-temperature local density approximation for the exchange and correlation potential [61], which means that the differences shown between the relativistic and nonrelativistic results are due to the non-interacting kinetic energy function (i.e. Dirac-Kohn-Sham or Kohn-Sham).

2.5.2 Shock Hugoniots

The equation of state is often used to generate a shock Hugoniot for a particular plasma. The information contained within the Hugoniot is useful for comparing the results of different models as well as comparing to experimentally obtained data. Here we present Hugoniots determined

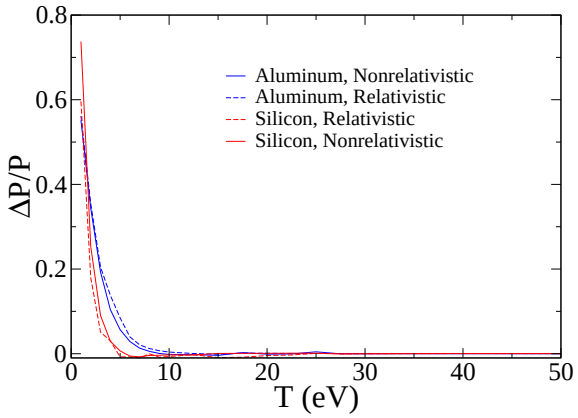

Figure 2.2: Thermodynamic consistency of the plasma pressure in silicon and aluminum (both at solid density) as calculated using the virial theorem and differentiation of the free energy. $\Delta P/P = \frac{P_{virial} - P_{thermodynamic}}{P_{virial}}$, where P_{virial} is the pressure obtained through use of the virial theorem and $P_{thermodynamic}$ is the pressure obtained from numerical differentiation of the free energy.

from both relativistic and nonrelativistic Tartarus EOS data. In Figure 2.3 we can see the two Tartarus modes compared to Path Integral Monte-Carlo (PIMC/DFT-MD) simulations done by Militzer et al [2] for silicon. Both the PIMC and average atom models show pronounced features in the Hugoniot arising from ionization of the bound states, and the nonrelativistic and relativistic Tartarus calculations are consistent with each other up to very high pressures, where the atoms become fully ionized and the electrons behave like a free gas. The features in the Hugoniot near 350 Mbar and 3500 Mbar deviate little between the relativistic and nonrelativistic calculations. This is expected as the bound states in silicon have nearly the same eigenvalues whether determined relativistically or nonrelativistically. At high temperatures we begin to see the sharp turn back of the Hugoniot expected from relativistic systems due to the increasingly relativistic nature of the free electron gas when $\beta = \frac{k_B T}{mc^2}$ becomes appreciable.

For heavier elements, we should expect to see a more pronounced difference in the nonrelativistic and relativistic calculations. For the case of silver ($Z = 47$) in Figure 2.4, we again see agreement between the two modes at low pressure and for features caused by bound states ionizing. The nonrelativistic Hugoniot should asymptotically approach a compression ratio of 4, which is a behavior we see for the nonrelativistic mode of Tartarus. For the relativistic mode, we see the characteristic turn-back of the Hugoniot towards the relativistic limit of a compression ratio of 7 [46]. For further validation at low pressure and compression, experimental data from the Rusbank database are also shown, which has marginally better agreement with the relativistic result.

2.6 Discussion

The need to be able to quickly and robustly generate EOS data for a variety of elements requires the use of models with high computational efficiency. The average atom model provides a means of approximating the EOS data in the form of a fast, single atomic site calculation for a wide range of plasma temperatures and densities. Numerical difficulties with the average atom model come from properly accounting for resonances in the continuum density of states arising from pressure ionization in the plasma. The Green's function approach accurately accounts for

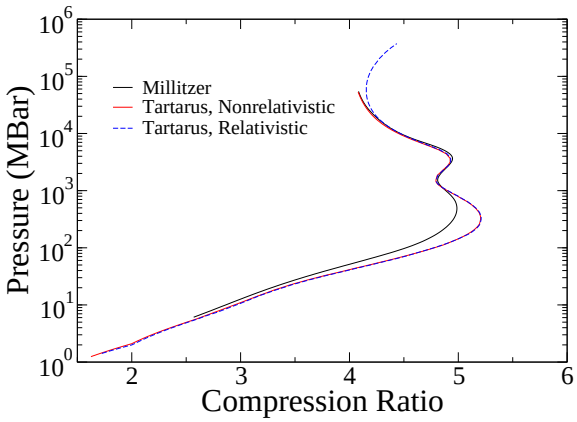

Figure 2.3: Comparison of the principal shock Hugoniot determined by the nonrelativistic and relativistic modes of Tartarus and the PIMC/DFT-MD method of Militzer et al. The compression ratio is the shocked density divided by the nominal density, $\rho_0 = 2.33$ g/cm^3 [2]

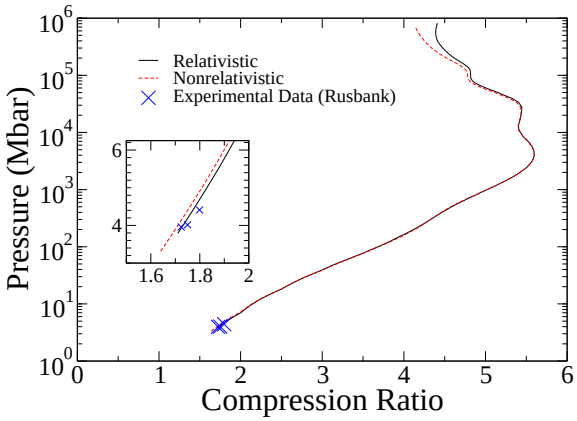

Figure 2.4: Comparison of the nonrelativistic and relativistic modes of the Tartarus calculation for silver, with $\rho_0 = 10.49$ g/cm^3. No error was given in the sources for the experimental data [3, 4].

the effects of resonances and even loosely bound states without the need for adaptive meshes or large numbers of quadrature points.

The GF formulation has been implemented in the Tartarus code. The robustness of the GF algorithm allows for Tartarus to generate an EOS without the need of manual parameter adjustment. The relativistic mode requires more computational effort, but is shown to produce results consistent with the nonrelativistic mode at lower temperatures and for elements of low atomic number. These comparisons demonstrate Tartarus' ability to be run in the more expedient nonrelativistic mode for lighter elements and lower plasma temperatures but still able to use the full relativistic calculation to obtain accurate data on the plasma properties at high temperatures and for heavier elements.

Chapter 3

Wide Ranging Equation of State with `Tartarus`: a Hybrid Green's Function/Orbital based Average Atom Code

3.1 Abstract

Average atom models are widely used to make equation of state tables and for calculating other properties of materials over a wide range of conditions, from zero temperature isolated atom to fully ionized free electron gases. The numerical challenge of making these density functional theory based models work for *any* temperature, density or nuclear species is formidable. Here we present in detail a hybrid Green's function/orbital based approach that has proved to be stable and accurate for wide ranging conditions. Algorithmic strategies are discussed. In particular the decomposition of the electron density into numerically advantageous parts is presented and a robust and rapid self consistent field method based on a quasi-Newton algorithm is given. Example application to the equation of state of lutetium (Z=71) is explored in detail, including the effect of relativity, finite temperature exchange and correlation, and a comparison to a less approximate method. The hybrid scheme is found to be numerically stable and accurate for lutetium over at least 6 orders of magnitude in density and 5 orders of magnitude in temperature.

3.2 Introduction

Average atom models are computationally inexpensive and are used to provide rapid equation of state and other material properties with reasonable physical fidelity. While more accurate models exist, average atom models are popular not only because of their relative rapidity, but

also because they are reasonably accurate for a wide range of conditions, ranging from isolated atom to free electron gas, from zero temperature to thousands of eV.

However, while average atom models can in principle be used for any conditions, their numerical implementation is far from trivial. Designing a generally robust and stable algorithm that works for any material, or conditions, is a formidable challenge. In this work we discuss in some detail a hybrid orbital/Green's function implementation that we have developed in the Tartarus code.

This implementation is borne by the exploratory ideas presented in references [43, 39], but builds on the much larger base of average atom literature. The original presentation of the physical model was given Liberman in references [26, 62]. This particular model was then expanded on and explored in more detail by other authors, including references [58, 63, 46, 64, 54, 60, 65, 66, 67]. However, many other average atom like models with their own advantages and disadvantages were also developed. Some include treatments of band structure (missing in Liberman's model) [25, 68]. Others include a more realistic treatment of ionic structure [29, 69, 32, 28].

We present a detailed description of the model and its implementation, including a very efficient self consistent field solution method. We discuss the advantages of the hybrid approach and the weakness of using purely orbitals or Green's functions. Example is made of the equation of state of lutetium (Z=71). We explore the effect of a fully relativistic versus non-relativistic treatment, as well as the effect of recent finite temperature exchange and correlation potentials versus temperature independent potentials. Comparison is made to a less approximate model in the low temperature region where such models are available. Finally, unsavory features of the model like thermodynamic inconsistency are discussed.

3.3 Average Atom Model

3.3.1 Model Description

We consider an ensemble of electrons and nuclei in local thermodynamical equilibrium. These can form a gas, liquid, solid or plasma. In the average atom model we define a sphere, with a

volume equal to the average volume per nucleus (V^{ion}), with a nucleus of charge Z placed at the center (the origin). The sphere is required to be charge neutral and the boundary condition at the edge of the sphere is that the effective electron-nucleus interaction potential $V^{eff}(\boldsymbol{r}) = 0$, and the electrons wavefunctions therefore match to the known analytic solution at this boundary. We must also set $V^{eff}(\boldsymbol{r}) = 0$ outside the sphere for reasons that will become clear later. This situation is summarized in figure 3.1.

The electron density $n_e(\boldsymbol{r})$ and $V^{eff}(\boldsymbol{r})$ inside the sphere are determined by solving the relativistic or non-relativistic density functional theory (DFT) [22, 21, 51, 52] equations. The procedure is as follows [63]: starting from an initial guess at $V^{eff}(\boldsymbol{r})$ the Schrödinger or Dirac equation is solved for either the eigenfunctions $\psi_\epsilon(\boldsymbol{r})$ or Green's functions $G(\boldsymbol{r}, \epsilon)$ and the electron density is constructed

$$n_e(\boldsymbol{r}) = \int_{-\infty}^{\infty} d\epsilon\, f(\epsilon, \mu)\psi_\epsilon^\dagger(\boldsymbol{r})\psi_\epsilon(\boldsymbol{r}) \tag{3.1}$$

$$= -\frac{1}{\pi}\Im\int_{-\infty}^{\infty} d\epsilon f(\epsilon, \mu) Tr G(\boldsymbol{r}, \epsilon) \tag{3.2}$$

where (non-)relativistically G is (2×2) 4×4 matrix, and ψ is a (1×2) 1×4 column vector. The practical formulae for evaluation of $n_e(\boldsymbol{r})$ are given is section 3.4.3. $f(\epsilon, \mu)$ is the Fermi-Dirac occupation factor which depends on the electron energy ϵ and chemical potential μ as well as the plasma temperature T. μ is determined by requiring the ion-sphere to be charge neutral

$$Z - \int_{V^{ion}} d^3r\, n_e(\boldsymbol{r}) = 0 \tag{3.3}$$

With $n_e(\boldsymbol{r})$ so determined a new $V^{eff}(\boldsymbol{r})$ is found

$$V^{eff}(\boldsymbol{r}) = V^{el}(\boldsymbol{r}) + V^{xc}(\boldsymbol{r}) \tag{3.4}$$

where the electrostatic part is

$$V^{el}(\boldsymbol{r}) = -\frac{Z}{r} + \int_{V^{ion}} d\boldsymbol{r'}\, \frac{n_e(\boldsymbol{r'})}{\mid \boldsymbol{r} - \boldsymbol{r'} \mid} \tag{3.5}$$

and the exchange and correlation part is

$$V^{xc}(\boldsymbol{r}) = \frac{\delta F^{xc}}{\delta n_e(\boldsymbol{r})} \tag{3.6}$$

where F^{xc} is the chosen exchange and correlation free energy. Equations (3.1) to (3.6) are then repeatedly solved until self-consistent. In section 3.4.4 a rapid and robust strategy for this self-consistent field (SCF) problem is presented. The system is spherically symmetric about the origin and as a result $n_e(\boldsymbol{r}) \to n_e(r)$ and $V^{eff}(\boldsymbol{r}) \to V^{eff}(r)$.

3.3.2 Poisson Equation

Spherical symmetry simplifies the solution of the Poisson equation (equation (3.5))

$$V^{el}(r) = -\frac{Z}{r} + \frac{1}{r}\int_0^r dr'\, r'^2 n_e(r') + \int_r^R dr'\, r' n_e(r') \tag{3.7}$$

This result is obtained by using a Spherical Harmonic expansion of $1/|\boldsymbol{r} - \boldsymbol{r}'|$.

3.3.3 Electron density

On applying spherical symmetry to the Dirac equation, $n_e(r)$ can be written in terms of orbitals [46, 47]

$$\begin{aligned} n_e(r) &= \sum_{i \in B} f(\epsilon_i, \mu) \frac{2|\kappa_i|}{4\pi r^2} [P^2_{\kappa_i}(r, \epsilon_i) + Q^2_{\kappa_i}(r, \epsilon_i)] \\ &+ \int_0^\infty d\epsilon f(\epsilon, \mu) \sum_{\substack{\kappa=-\infty \\ \kappa \neq 0}}^{+\infty} \frac{2|\kappa|}{4\pi r^2} [P^2_{\kappa}(r, \epsilon) + Q^2_{\kappa}(r, \epsilon)] \end{aligned} \tag{3.8}$$

where the sum over i runs over all bound states and $P_\kappa(r, \epsilon)$ ($Q_\kappa(r, \epsilon)$) is the large (small) component of the radial Dirac equation. ϵ is the energy minus the rest mass of the electron so that it is directly comparable to the energy appearing in the Schrödinger equation. For the

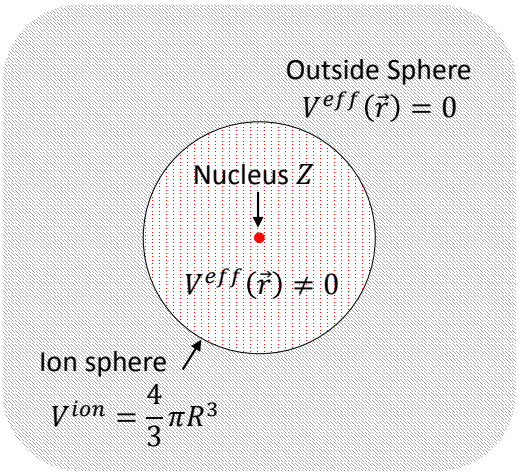

Figure 3.1: Schematic diagram of average atom physical model. Inside the ion sphere the electronic structure is determined with density functional theory. The boundary condition is that outside the sphere the effective electron-nucleus potential is zero.

Schrödinger equation the expression for $n_e(r)$ reads

$$\begin{aligned} n_e(r) &= \sum_{i\in B} f(\epsilon_i,\mu)\frac{2(2l_i+1)}{4\pi r^2}[P^2_{l_i}(r,\epsilon_i)] \\ &+ \int_0^\infty d\epsilon\, f(\epsilon,\mu)\sum_{l=0}^{\infty}\frac{2(2l+1)}{4\pi r^2}[P^2_l(r,\epsilon)] \end{aligned} \tag{3.9}$$

where P_l is now the solution to the radial Schrödinger equation. Note that the sum over κ in equation (3.8) can be converted into a sum over orbital angular momentum index l with

$$\sum_{\substack{\kappa=-\infty\\ \kappa\neq 0}}^{+\infty} \rightarrow \sum_{l=0}^{\infty}\delta_{\kappa,-l-1} + \sum_{l=1}^{\infty}\delta_{\kappa,l} \tag{3.10}$$

where δ is the Kronecker delta. Using this, and setting the small components $Q_\kappa = 0$, one recovers the expression the non-relativistic expression (3.9) from the relativsitic one (3.8).

In terms of the Green's function the expression for $n_e(r)$ is identical for both the relativistic and non-relativistic cases

$$n_e(r) = -\frac{1}{\pi}\Im\int_{-\infty}^{\infty} d\epsilon f(\epsilon,\mu) TrG(r,\epsilon) \tag{3.11}$$

Relativistically the Green's function is given by

$$\begin{aligned} TrG(r,\epsilon) &= -\imath p(1+\frac{\epsilon}{2mc^2})2m \\ &\times \sum_{\substack{\kappa=-\infty\\ \kappa\neq 0}}^{+\infty}\frac{2|\kappa|}{4\pi r^2}[P^R_\kappa(r,\epsilon)P^I_\kappa(r,\epsilon) + Q^R_\kappa(r,\epsilon)Q^I_\kappa(r,\epsilon)] \end{aligned} \tag{3.12}$$

where

$$p = \sqrt{2m\epsilon\left(1+\frac{\epsilon}{2mc^2}\right)}, \tag{3.13}$$

is the magnitude of momentum, P^R (P^I) is the large component, regular (irregular) solution to the radial Dirac equation, and Q^R (Q^I) the corresponding small components (see section 3.3.4).

Non-relativistically, the trace of the Green's function becomes

$$TrG(r,\epsilon) = -\imath p 2m \sum_{l=0}^{\infty} \frac{2(2l+1)}{4\pi r^2}[P_l^R(r,\epsilon)P_l^I(r,\epsilon)] \tag{3.14}$$

where P^R (P^I) is the regular (irregular) solution to the radial Schrödinger equation, and

$$p = \sqrt{2m\epsilon}. \tag{3.15}$$

3.3.4 Boundary Conditions

The boundary conditions at the sphere are that the wavefunctions must match the solution to the Dirac or Schrödinger with $V^{eff}(r) = 0$, where both equations reduce to the spherical Bessel equation. Relativistically, for negative energy ($\epsilon < 0$ i.e. the bound states), the radial wavefunctions must match

$$P_\kappa(R,\epsilon) = A_{\epsilon,\kappa} R\, \imath^l\, h_l(pR) \tag{3.16}$$

$$Q_\kappa(R,\epsilon) = A_{\epsilon,\kappa} R\, \imath^l\, \mathrm{sgn}(\kappa) \sqrt{\frac{\epsilon}{\epsilon + 2mc^2}}\, h_{\bar{l}}(pR) \tag{3.17}$$

with h_l the spherical Hankel function and $\bar{l} = l - \mathrm{Sgn}(\kappa)$, where Sgn returns the sign of the argument, and $A_{\epsilon,\kappa}$ is a constant of proportionality that is determined by the normalization integral

$$\int dr[P^2_{\kappa_i}(r,\epsilon_i) + Q^2_{\kappa_i}(r,\epsilon_i)] = 1 \tag{3.18}$$

It is for this normalization integral that we must assume $V^{eff}(r) = 0$ for $r \geq R$. For positive energies

$$P_\kappa(R,\epsilon) = \sqrt{\frac{p}{\pi\epsilon}} pR\, [\cos\delta_\kappa j_l(pR) + \sin\delta_\kappa \eta_l(pR)] \tag{3.19}$$

$$Q_\kappa(R,\epsilon) = -\mathrm{sgn}(\kappa)\sqrt{\frac{\epsilon}{\epsilon + 2mc^2}} \times \sqrt{\frac{p}{\pi\epsilon}} pR\, [\cos\delta_\kappa j_{\bar{l}}(pR) + \sin\delta_\kappa \eta_{\bar{l}}(pR)] \tag{3.20}$$

where j_l (η_l) is the spherical Bessel (Neumann) function. δ_κ is the energy dependent phase shift. The numerical P_κ and Q_κ have arbitary normalization. To recover the correct physical normalization (equations (3.19) and (3.20)) they are mutiplied by a constant. This constant and δ_κ are determined by requiring the numerical the boundary conditions to be satisfied.

Non-relativistically, for negative energies, we have

$$P_l(R,\epsilon) \;=\; A_{\epsilon,l} R\, \imath^l\, h_l(pR) \tag{3.21}$$

with $A_{\epsilon,l}$ determined by

$$\int dr[P_{l_i}^2(r,\epsilon_i)] = 1 \tag{3.22}$$

and for positive energies

$$P_l(R,\epsilon) \;=\; \sqrt{\frac{2mp}{\pi}} R\left[\cos\delta_l j_l(pR) + \sin\delta_l \eta_l(pR)\right] \tag{3.23}$$

where δ_l and the normalization constant for the numerical P_l are determined by requiring the numerical value of $P_l(r)$ and its first derivative with respect to r to satisfy the boundary condition (3.23) and its derivative.

Relativisitcally, for the regular solutions used to construct the Green's function (equation (3.12)), the boundary conditions are

$$P_\kappa^R(R,\epsilon) \;=\; R\left[j_l(pR) - \imath p h_l(pR) t_l(p)\right] \tag{3.24}$$

$$\begin{aligned} Q_\kappa^R(R,\epsilon) \;&=\; \mathrm{sgn}(\kappa)\sqrt{\frac{\epsilon}{\epsilon+2mc^2}} \\ &\quad \times R\left[j_{\bar{l}}(pR) - \imath p h_{\bar{l}}(pR) t_l(p)\right] \end{aligned} \tag{3.25}$$

where t_l is the energy dependent t-matrix that is determined by matching the numerical solution to this boundary condition. It is worth noting that for real energies ϵ the phase shifts and the

t-matrix are simply related [53]. For the irregular solutions

$$P^I_\kappa(R,\epsilon) = Rh_l(pR) \tag{3.26}$$

$$Q^I_\kappa(R,\epsilon) = \mathrm{sgn}(\kappa)\sqrt{\frac{\epsilon}{\epsilon+2mc^2}}Rh_{\bar{l}}(pR) \tag{3.27}$$

The boundary conditions for the non-relativistic case are

$$P^R_\kappa(R,\epsilon) = R\left[j_l(pR) - \imath p h_l(pR)t_l(p)\right] \tag{3.28}$$

$$P^I_\kappa(R,\epsilon) = Rh_l(pR) \tag{3.29}$$

3.3.5 Density of States

Relativistically the density of states $\chi(\epsilon)$ in terms of orbitals is

$$\begin{aligned}\chi(\epsilon)=&\sum_{i\in B}\delta(\epsilon_i-\epsilon)\int_0^R dr\, 2|\kappa_i|[P^2_{\kappa_i}(r,\epsilon_i)+Q^2_{\kappa_i}(r,\epsilon_i)]\\ &+\sum_\kappa 2|\kappa|\int_0^R dr\,[P^2_\kappa(r,\epsilon)+Q^2_\kappa(r,\epsilon)]\Theta(\epsilon)\end{aligned} \tag{3.30}$$

where δ is the Dirac delta function, and Θ is the Heaviside step function. Non-relativistically the density of states is

$$\begin{aligned}\chi(\epsilon) = &\sum_{i\in B}\delta(\epsilon_i-\epsilon)\int_0^R dr\, 2(2l_i+1)[P^2_{l_i}(r,\epsilon_i)]\\ &+\sum_l 2(2l+1)\int_0^R dr\,[P^2_l(r,\epsilon)]\Theta(\epsilon)\end{aligned} \tag{3.31}$$

In terms of the Green's function, the expression is identical for both the relativistic and non-relativistic cases

$$\chi(\epsilon) = -\frac{1}{\pi}\Im\int_{V^{ion}} d^3r\, TrG(r,\epsilon) \tag{3.32}$$

3.3.6 Equation of State

The electronic free energy F and internal energy U per atom are

$$F = F^{el} + F^{xc} + F^{ks} \tag{3.33}$$

$$U = F^{el} + U^{xc} + U^{k} \tag{3.34}$$

F^{el} is the electrostatic contribution

$$F^{el} = \frac{1}{2}\int_{V^{ion}} d^3r \left[V^{el}(r) - \frac{Z}{r}\right] n_e(r) \tag{3.35}$$

F^{xc} (U^{xc}) is the exchange and correlation free (internal) energy and F^{ks} is the kinetic and entropic term

$$F^{ks} = U^{k} - TS \tag{3.36}$$

where U^k is the electron kinetic energy contribution to the internal energy

$$U^{k} = \int_{-\infty}^{\infty} d\epsilon f(\epsilon,\mu)\chi(\epsilon)\epsilon - \int_{V^{ion}} d^3r V^{eff}(r) n_e(r) \tag{3.37}$$

and S is the entropy

$$\begin{aligned} S &= -\int_{-\infty}^{\infty} d\epsilon \chi(\epsilon) \\ &\times \left[f(\epsilon,\mu)\ln(f(\epsilon,\mu)) + (1-f(\epsilon,\mu))\ln(1-f(\epsilon,\mu))\right] \end{aligned} \tag{3.38}$$

The electronic pressure P calculated using the virial theorem is

$$P = \frac{1}{V^{ion}}\left[\frac{\mathcal{T} + F^{el}}{3}\right] + P^{xc} \tag{3.39}$$

where

$$P_{xc} = \frac{1}{V^{ion}}\left[-F^{xc} + \int_V d^3r\, n_e(r) V^{xc}(r)\right] \tag{3.40}$$

and $\mathcal{T}$ is

$$\mathcal{T} = 2\int_{-\infty}^{\infty} d\epsilon f(\epsilon,\mu)\chi^A(\epsilon)\epsilon - 2\int_{V^{ion}} d^3r V^{eff}(r) n_e^A(r) \tag{3.41}$$

Here the superscript A means the quantity due only to the large component. For the relativistic case this means setting $Q_\kappa = 0$ in the expressions for the density (3.8) and density of states (3.30), and in the Green's function (3.12) which is then used in expressions (3.11) and (3.32). For the non-relativistic case, there is no small component, so $n_e(r) = n_e^A(r)$ and $\chi(\epsilon) = \chi^A(\epsilon)$.

3.3.7 Summary

In this section we have given formulae that both define the model and can be use to evaluate it numerically. In the following section we present practical strategies for solution of the model over a wide range of densities, temperatures and elements based on these expressions.

3.4 Numerical Methods

3.4.1 Numerical Solution of the Schrödinger and Dirac Equations

The radial Dirac equations are

$$(V^{eff}(r) - \epsilon)P_\kappa + c(\frac{d}{dr} - \frac{\kappa}{r})Q_\kappa = 0 \tag{3.42}$$

$$-c(\frac{d}{dr} + \frac{\kappa}{r})P_\kappa + (V^{eff}(r) - \epsilon - 2mc^2)Q_\kappa = 0 \tag{3.43}$$

and the radial Schrödinger equation is

$$\frac{d^2P_l}{dr^2} + 2\left(\epsilon - V^{eff}(r) - \frac{l(l+1)}{2r^2}\right)P_l = 0 \tag{3.44}$$

These can be solved numerically with a variety of methods. We recommend using the Adams methods, as explained in detail in reference [56] (also used in [70]). We have used the fifth order formula. This is a predictor-corrector method, but solves the predictor-corrector loop analytically. A robust method for obtaining the necessary four point starting values for outward integration is also presented in [56] and is straightforwardly adapted for the inward integrations.

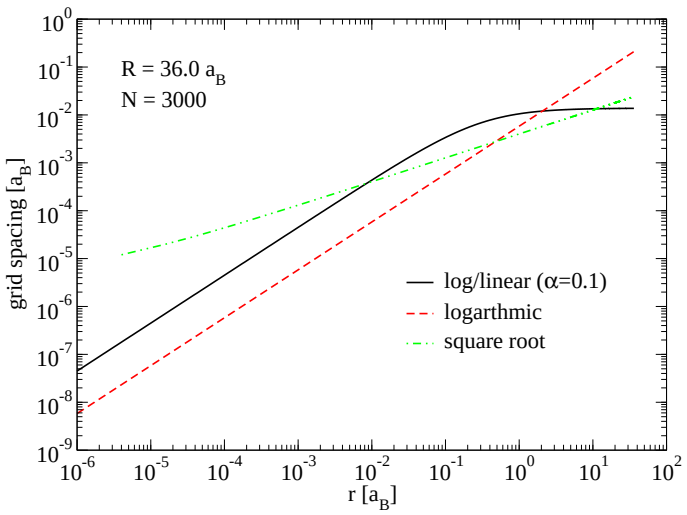

Figure 3.2: Grid spacing $r_{i+1} - r_i$ for various grid generation methods described in the text.

Inward integrations (i.e. from R to 0) for bound states and the irregular solutions start from the boundary condition values.

For the radial grid we have tried one based on $\sqrt{r}$. A disadvantage is that this does not allow one to vary the total number of grid points N independently from the value of r at the first grid point r_1. Since the value of r at the end of the grid is fixed by the ion-sphere radius R, $r_1 = R/N^2$. This lack of flexibility is problematic. We have also tried a grid based on $\log r$ [70], which allows such flexibility, but for low densities requires many of grid points to maintain resolution near the sphere boundary. Finally, we settled on the log-linear grid presented in [71]. This is logarithmic near the origin and so has enough points to resolve wavefunctions which can vary rapidly for small r, and switches to linear spacing as r increases. We have found this grid to be generally accurate from low to high density, and from low Z to high Z. We have found $r_1 = 1.0 \times 10^{-6}\, a_B$ and $N = 3000$ to be robust for the applications presented here. The log-linear grid also requires a parameter α to be chosen which determines how quickly it switches from logarithmic to linear. We have found $\alpha = 0.1$ to be generally reasonable. Note that $\alpha = 0$ corresponds to a purely logarithmic (exponential) grid.

Examples of the grid spacing from these three grid choices are shown in figure 3.2. For this case (lutetium at 0.01 g/cm^3, grid independent of temperatures) we find that r_1 and the grid spacing for the $\sqrt{r}$ grid are too large for accurate convergence. We also find that the $\log\, r$ grid is too sparse for large r. Only the log-linear grid has the resolution everywhere that is needed. Note that we have implemented the Adams method so that `Tartarus` can use any grid provided that r can be transformed onto a linearly spaced grid x and dr/dx is smooth and can be calculated [56, 70].

3.4.2 Contour Integrals for Green's Functions

The main advantage of using the Green's function is that it is analytic in the complex plane, allowing energy integrals along the real energy axis to be deformed to complex energy z using

Cauchy's integral theorem. The electron density can be calculated thus

$$\begin{aligned} n_e(r) &= \frac{1}{\pi}\Im\int_C dz f(z,\mu) TrG(r,z) \\ &\quad +2k_BT\Re\left\{\sum_{j=1}^{N_{mat}} TrG(r,z_j)\right\} \end{aligned} \tag{3.45}$$

C refers to a contour that closes when joined to the real axis [43], and the sum over j is a sum over the N_{mat} poles (known as Matsubara poles) of the Fermi-Dirac function enclosed by this closed contour, at energies $z_j = \mu + \imath\pi(2j-1)k_BT$. Similarly, for equation of state calculation we can use

$$\begin{aligned} \int_{-\infty}^{\infty} d\epsilon f(\epsilon,\mu)\chi(\epsilon)\epsilon &= \frac{1}{\pi}\Im\int_{V^{ion}} d^3r \int_C dz f(z,\mu)\, z\, TrG(r,z) \\ +2k_BT\Re&\left\{\int_{V^{ion}} d^3r \sum_{j=1}^{N_{mat}} z_j\, TrG(r,z_j)\right\} \end{aligned} \tag{3.46}$$

The advantage of carrying out the energy integrals in the complex plane is twofold: 1) sharp features in the integrand that occur for real energies are broadened in the complex plane. Hence resonances in the positive energy states that need to be tracked and resolved on the real energy axis are broad and smoothly varying in the complex plane. This point was explored in detail in [43] (also see figure 3.5), and 2) negative energy (or bound) states are treated in exactly the same way as positive energy states. The search for bound states is tricky to make generally robust, and states with very small energies (eg. $|\epsilon| < 1 \times 10^{-4} E_h$) can be especially hard to accurately represent. By designing the contour C so that it returns to the real axis at a large negative energy, the search for bound states could be avoided altogether. However, since deeply bound states are very sparse in energy space, it makes sense to treat these more deeply bound states with the usual orbital approach, and the more weakly bound states with Green's functions (see section 3.4.3).

We have used a rectangular contour, as in reference [43]. To find ϵ_{min}, the energy at which the contour rejoins the real energy axis, we first solve for the bounds states using standard search methods (eg. reference [56]), and look for the highest lying (least negative) energy gap

≥ 10 E_h between two states in an energy ordered list. ϵ_{min} is then set to be 1 E_h less than the eigenenergy of the state on the higher lying side of that gap. This is done at each iteration of the SCF procedure to avoid double counting bound states. It may seem that since we are already finding the bound eigenstates we should just set $\epsilon_{min} = 0$ E_h. In many cases this would work, but as mentioned above inaccuracies would occur if our search algorithm missed bound states, or if bound states had very small energies. The Green's function approach avoids both of these pitfalls and as a result is very stable.

ϵ_{max} is set by requiring $f(\epsilon_{max}, \mu) \approx 10^{-10}$. We split the integration into panels and use a 4 point Gauss-Legrende scheme in each. Care is taken to resolve the Green's function near the Fermi-edge, which is important for highly degenerate cases, i.e. when $k_B\,T/E_F << 1$ (E_F is the Fermi energy). The total number of points used is dependent on ϵ_{min}, ϵ_{max} and μ, but typical values are 1000 to 2000 energy points.

While any contour can be used to carry out the energy integrals above, calculation of the entropy is special. Due to the many valued logarithm in (3.38) the contour cannot pass the branch-cut parallel to the first Matsubara pole at $\Im z = \pi k_B T$. For sufficiently high temperature $\pi k_B T$ is greater than the imaginary part of the energy anywhere on the contour and so the SCF contour can be used for S. Typically this is so for $k_B T \gtrsim 10$ eV. For temperatures less than this we have decided to use a purely orbital based density of states calculation, only for the entropy at the end of the SCF procedure. Hence we use all bound orbitals and a resonance tracker [46] for the positive energy states. Fortunately, at such relatively low temperatures resonance tracking is less challenging and we have found this to be accurate enough for S. Note that even for these low T cases Green's functions are still used in the SCF procedure where we find they offer enhanced stability.

3.4.3 Density Construction

Electron density $n_e(r)$ is the key quantity in density functional theory and must be constructed accurately. While it is in principle possible to construct $n_e(r)$ directly from the Green's function or the orbitals, it is very difficult to do this robustly over a wide range of temperatures or

densities and materials. Instead we have used the following hybrid decomposition

$$\begin{aligned} n_e(r) =& n_e^{core}(r) + n_e^{GF}(r, l_{max}) + n_e^{ctm}(r, l_{max}) \\ & - n_e^{free}(r, l_{max}) + n_e^0 \end{aligned} \tag{3.47}$$

Here $n_e^{core}(r)$ is the density due to bound states with $\epsilon < \epsilon_{min}$ (from equation (3.8))

$$n_e^{core}(r) = \sum_{i \in B, \epsilon_i < \epsilon_{min}} f(\epsilon_i, \mu) \frac{2|\kappa_i|}{4\pi r^2} [P_{\kappa_i}^2(r, \epsilon_i) + Q_{\kappa_i}^2(r, \epsilon_i)] \tag{3.48}$$

$n_e^{GF}(r, l_{max})$ is calculated using (from equation (3.11))

$$n_e(r) = -\frac{1}{\pi} \Im \int_{\epsilon_{min}}^{\epsilon_{max}} d\epsilon f(\epsilon, \mu) TrG(r, \epsilon) \tag{3.49}$$

with $TrG(r, \epsilon)$ calculated using (from equation (3.12))

$$\begin{aligned} TrG(r, \epsilon, l_{max}) &= -\imath p (1 + \frac{\epsilon}{2mc^2}) 2m \\ \times \sum_{l=0}^{l_{max}} \sum_{\kappa} & \frac{2|\kappa|}{4\pi r^2} [P_\kappa^R(r, \epsilon) P_\kappa^I(r, \epsilon) + Q_\kappa^R(r, \epsilon) Q_\kappa^I(r, \epsilon)] \end{aligned} \tag{3.50}$$

where the sum over κ runs over the allowed values of κ for a given l, i.e. for $l > 0$, $\kappa = \{l, -l-1\}$ and for $l = 0$, $\kappa = -1$.

$n_e^{ctm}(r, l_{max})$ is the density given by (from equation (3.8))

$$\begin{aligned} n_e^{ctm}(r, l_{max}) = & \int_0^{\epsilon_{max}} d\epsilon f(\epsilon, \mu) \sum_{l=l_{max}+1}^{l_{con}} \sum_{\kappa} \\ & \times \frac{2|\kappa|}{4\pi r^2} [P_\kappa^2(r, \epsilon) + Q_\kappa^2(r, \epsilon)] \end{aligned} \tag{3.51}$$

$n_e^{free}(r, l_{max})$ is given by

$$\begin{aligned} n_e^{free}(r, l_{max}) = & \int_0^{\epsilon_{max}} d\epsilon f(\epsilon, \mu) \sum_{l=0}^{l_{con}} \sum_{\kappa} \\ & \times \frac{2|\kappa|}{4\pi r^2} [P_\kappa^{0\,2}(r, \epsilon) + Q_\kappa^{0\,2}(r, \epsilon)] \end{aligned} \tag{3.52}$$

where the superscript 0 on the orbitals indicates solution to the Dirac equation with $V^{eff}(r) = 0$, i.e. the "$free$" solution. l_{con} is determined [58] by incrementing l and evaluating

$$\begin{aligned} &\int_0^R dr \int_0^{\epsilon_{max}} d\epsilon f(\epsilon,\mu) \sum_\kappa 2|\kappa| \\ &\times \left\{ [P_\kappa^2(r,\epsilon) + Q_\kappa^2(r,\epsilon)] - [P_\kappa^{0\,2}(r,\epsilon) + Q_\kappa^{0\,2}(r,\epsilon)] \right\} \\ &< \texttt{TOL} \end{aligned} \tag{3.53}$$

until for two consecutive l's this condition is true. We have found $\texttt{TOL} = 10^{-4}$ to be robust. n_e^0 is the free electron gas density for temperature T and chemical potential μ. It is used to correct the electron density that has had $n_e^{free}(r)$ removed and the l sum truncated at l_{con}

$$\begin{aligned} n_e^0 &= \int_0^\infty d\epsilon f(\epsilon,\mu) \sum_{l=0}^\infty \sum_\kappa \frac{2|\kappa|}{4\pi r^2} [P_\kappa^{0\,2}(r,\epsilon) + Q_\kappa^{0\,2}(r,\epsilon)] \\ &= c_{TF} \left[F_{\frac{1}{2}}(\mu/k_BT, k_BT/mc^2) + \frac{k_BT}{mc^2} F_{\frac{3}{2}}(\mu/k_BT, k_BT/mc^2) \right] \end{aligned} \tag{3.54}$$

where $c_{TF} \equiv \sqrt{2}(k_BT)^{\frac{3}{2}}/\pi^2$ and

$$F_n(\eta,\beta) = \int_0^\infty dx \frac{x^n \sqrt{1 + \frac{1}{2}\beta x}}{e^{x-\eta} + 1} \tag{3.55}$$

are the relativistic Fermi-Dirac integrals [59]. Hence electrons in states with $l > l_{con}$ are treated as free electrons. The convergence of equation (3.53) ensures that this approximation is accurate.

l_{max} controls which states are treated with Green's functions, and which are treated with orbitals. Typically we choose $l_{max} \approx 40$, which ensures any resonances in these angular momentum channels are correctly integrated. For $n_e^{ctm}(r)$ and $n_e^{free}(r)$ we use a fixed energy grid, based on a linearly spaced $\sqrt{\epsilon}$ grid and typically use 400 points. Using orbitals on this fixed energy grid is very rapid, more so than the Green's function evaluation which uses a denser energy grid. Moreover the Green's function requires both the regular and irregular solutions, whereas the orbital only requires one solution of the Dirac equation. The above decomposition

is robust for the cases studied here. The non-relativistic decomposition is identical and can be obtained from the above by setting $Q_\kappa = 0$, $k_B T/mc^2 = 0$ and $\epsilon/2mc^2 = 0$.

This decomposition scheme is also use to evaluate U^k and $\mathcal{T}$. Note that, analgous to n_e^0, the free electron gas kinetic energy density k_e^0 is

$$\begin{aligned} k_e^0 &= \int_0^\infty d\epsilon f(\epsilon,\mu)\chi^0(\epsilon)\epsilon \\ &= c_{TF} k_B T \left[F_{\frac{3}{2}}(\mu/k_B T, k_B T/mc^2) \right. \\ &\left. + \frac{k_B T}{mc^2} F_{\frac{5}{2}}(\mu/k_B T, k_B T/mc^2) \right] \end{aligned} \tag{3.56}$$

where $\chi^0(\epsilon)$ is the free electron density of states. For $\mathcal{T}$ we have

$$\begin{aligned} k_e^{0,A} &= \int_0^\infty d\epsilon f(\epsilon,\mu)\chi^{A^0}(\epsilon)\epsilon \\ &= c_{TF} k_B T \left[F_{\frac{3}{2}}(\mu/k_B T, k_B T/mc^2) \right] \end{aligned} \tag{3.57}$$

One problem in solving for the Green's function is that at high l the solution near the origin becomes inaccurate because it results from the multiplication of a very small regular solution and a diverging irregular solution. We have found that this does not present a problem for solution of the SCF problem where small r dependence is suppressed with an r^2 from the Jabobian. However, for evaluation of the equation of state integrals like $\int d^3r\, n_e(r)/r$ are required (eg. equation (3.35)). Hence the result is more sensitive to the small r behavior of $n_e(r)$. Thus for equation of state only, we have found it useful to replace $n_e(r)$ for $r < 10^{-4}$ a$_B$ with an orbital only calculation of the density. Fortunately since we only need the small r part of this density and it is not needed in the SCF calculation, it does not need to be highly accurate. Hence we use a purely orbital based calculation for this part of the density for such integrals only. As for entropy at low temperature, we use all core orbitals and a resonance tracker to replace the Green's function calculation.

3.4.4 Self Consistent Field Acceleration

Let us denote as $|x\rangle$ a vector generated from $V^{eff}(r)$ or equivalently $n_e(r)$, where the components of the vector correspond to the grid points in no particular order. The SCF procedure is

1. Begin with an initial guess of $|x\rangle$.
2. Generate output vector $|x^{out}\rangle$. For example, if $|x\rangle$ is $V^{eff}(r)$ we would solve the Dirac equation, generate $n_e(r)$, and then calculate an output potential $V^{eff,out}(r) = |x^{out}\rangle$ by solving the Poisson equation and adding the exchange and correlation potential.
3. Calculate $|F\rangle = |x^{out}\rangle - |x\rangle$.
4. SCF convergence is achieved when $|F\rangle = |0\rangle$. If not achieved, generate new $|x\rangle$ and return to step 2.

In the frequently used simple mixing method the new $|x\rangle$ in step 4 is generated with

$$|x^{(m+1)}\rangle = |x^{(m)}\rangle + \alpha|F^{(m)}\rangle \tag{3.58}$$

where m labels the SCF iteration number. α is a mixing parameter that can be adaptive, or fixed. Typically a small value $\alpha = 0.1$ is needed for robust convergence and perhaps 80-100 iterations is necessary. A much more robust scheme that greatly reduces the number of iterations required to reach convergence has been given in the work of Eyert [72]. To our knowledge this has not been explored for average atom models before. Eyert's work is a correction and extension of the more famous Anderson mixing scheme [73]. In this scheme $|x\rangle$ is generated with

$$|x^{(l+1)}\rangle = |x^{(l)}\rangle + \alpha|F^{(l)}\rangle - \sum_{m=l-M}^{l-1} \gamma_m^{(l)} \left[|\Delta x^{(m)}\rangle + \alpha|\Delta F^{(m)}\rangle\right] \tag{3.59}$$

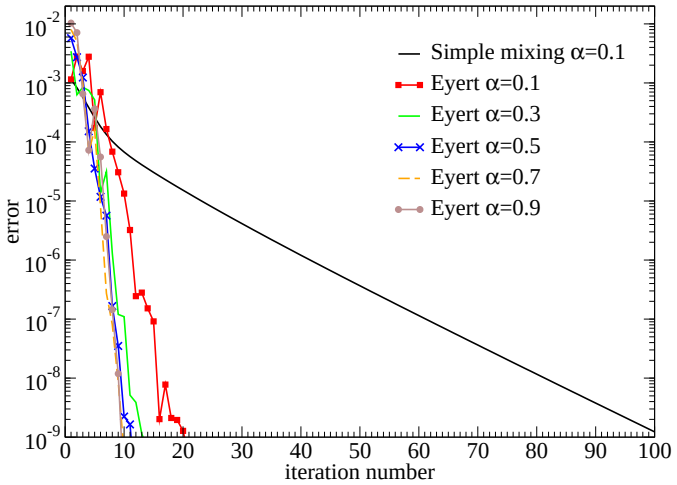

Figure 3.3: Example of SCF acceleration for lutetium at 10 eV and 10 g/cm^3. We compare simple mixing to Eyert's method with $M = 5$, as a function of the mixing parameter α.

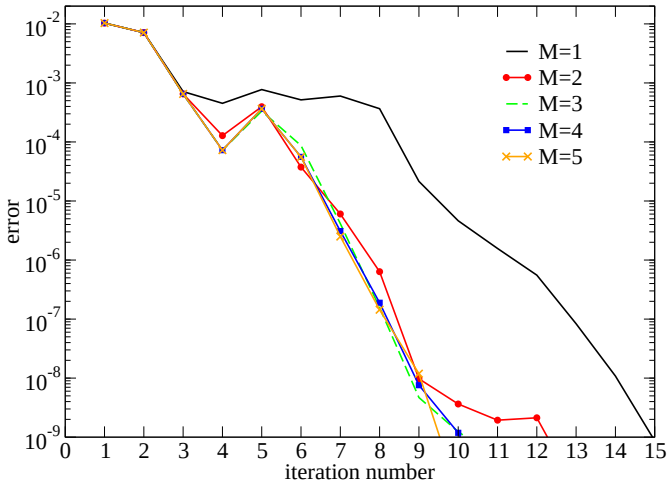

Figure 3.4: Example of SCF acceleration for lutetium at 10 eV and 10 g/cm^3. We compare Eyert's method with $\alpha = 0.9$ as a function of the order M.

where M is the order of the mixing (an input choice), the $\gamma_m^{(l)}$ are coefficients to be determined, and

$$|\Delta x^{(m)}\rangle = |x^{(m+1)}\rangle - |x^{(m)}\rangle \tag{3.60}$$

$$|\Delta F^{(m)}\rangle = |F^{(m+1)}\rangle - |F^{(m)}\rangle \tag{3.61}$$

For $M = 0$ equation (3.59) recovers the simple mixing formula above. For $M \geq 1$ we take into account the input and output vectors from the previous M iterations. To find the coefficients $\gamma_m^{(l)}$ we solve a matrix equation

$$\underline{\gamma} = \underline{B}^{-1}\underline{A} \tag{3.62}$$

where $\underline{\gamma} = [\gamma_m^{(l)}]$ is an $M \times 1$ matrix with $m = l - M, \ldots, l - 1$, $\underline{A}$ is an $M \times 1$ matrix with elements $\langle \Delta F^{(n)} | F^{(l)} \rangle$ ($n = l - M, \ldots, l - 1$). $\underline{B}$ is an $M \times M$ matrix with elements [1]

$$B_{nm} = (1 + w_0^2 \delta_{nm}) \langle \Delta F^{(n)} | \Delta F^{(m)} \rangle \tag{3.63}$$

Note that $\underline{B}$ is a symmetric matrix. Due to saturation of improvements for higher orders, M is taken to be 5 or 6 at maximum [72]. Hence the inversion of the matrix $\underline{B}$ is rapid. w_0^2 is a small parameter that breaks the symmetry (and thus removes linear dependences in Anderson's original method), it is fixed at 10^{-4}.

Eyert's method is a quasi-Newton method. It is exactly equivalent to Broydens [74, 75] method. The mixing parameter α for Eyert's method can be larger than for simple mixing. In practice we set $|x\rangle = V^{eff}(r) \times r/Z$, and calculate an error using the maximum value of the absolute value of $|F\rangle$. We require error $< 10^{-9}$ for two consecutive iterations. In figure 3.3 we show an example of this, comparing the simple mixing method with the safe choice of $\alpha = 0.1$ to Eyert's method for various α. The reduction in number of iterations, even with the same α is remarkable, and results in a corresponding reduction in computational time. Larger values of α lead to improved errors, though the effect saturates by $\alpha = 0.9$. It is important to note that not only is Eyert's method faster but it is also more stable than simple mixing, which can fail to

[1] The notation $\langle \Delta F^{(n)} | F^{(l)} \rangle$ means the inner product of the vectors.

converge in certain cases requiring manual reduction of α. Indeed setting $\alpha = 0.9$ and running this case with simple mixing the SCF loop fails to converge. In figure 3.4 we show the effect of the order of Eyert's method on the error. The advantages saturate by $M = 5$. Our default choice in `Tartarus` is $M = 5$, $\alpha = 0.9$. We have found this to be very stable, requiring no adjustment for any of the results presented here.

3.5 Example

3.5.1 Density of States

In figure 3.5 the density of states $\chi(z)$ as a function of complex energy z is shown for lutetium at 10 eV and 10 g/cm^3. For $\Im(z) = 0$ the calculation is purely in terms of orbitals. We used a bound state search algorithm, and the bound states appear in the figure as vertical lines at negative energies, representing the $\delta(\epsilon_i - \epsilon)$. For positive energy states we used a resonance tracker, and a resonance appears at ~ 0.2 E$_h$. For $\Im(z) > 0$ the calculation is purely in terms of Green's functions. We see Lorentzian like line shapes around each bound state energy and around the resonance. For $\Im(z) = 0.5$ E$_h$ the features are well smoothed out and integrating over them is accurate and does not need adaptive mesh refinement, as a resonance tracker does. This is the principal advantage of using Green's functions.

In figure 3.6 the density of states $\chi(z)$ along the 10 eV isotherm, from $\sim 1/100^{th}$ to 100 times solid density is shown. At the lowest density the most bound states exist (more appear at more negative energies). A few have been labeled in the figure to show that as density increases the bound states move toward the continuum (positive energy) and eventually disappear (pressure ionize). A resonance appears if a state with $l > 0$ is nearly bound. On reducing the density this resonance will transition to being a bound state with negative energy. The resonance is a result of the centrifugal barrier term, $-l(l+1)/r^2$ in the Schrödinger equation. Hence there are no resonances associated with $l = 0$ states.

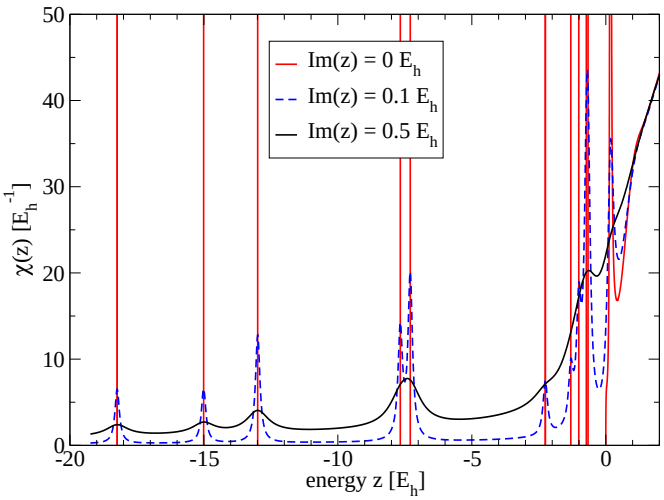

Figure 3.5: Density of states $\chi(z)$ for lutetium at 10 g/cm^3 and 10 eV. The solid red line is calculated using orbitals along the real energy axis. Using Green's functions we can evaluate $\chi(z)$ for complex energy z. Increasing the imaginary part of z features, including the discrete bound states and a continuum resonance, are broadened, making them easy to integrate over. Note $\Im z = 0.5$ E$_h$ is typical for the horizontal part of our integration contour.

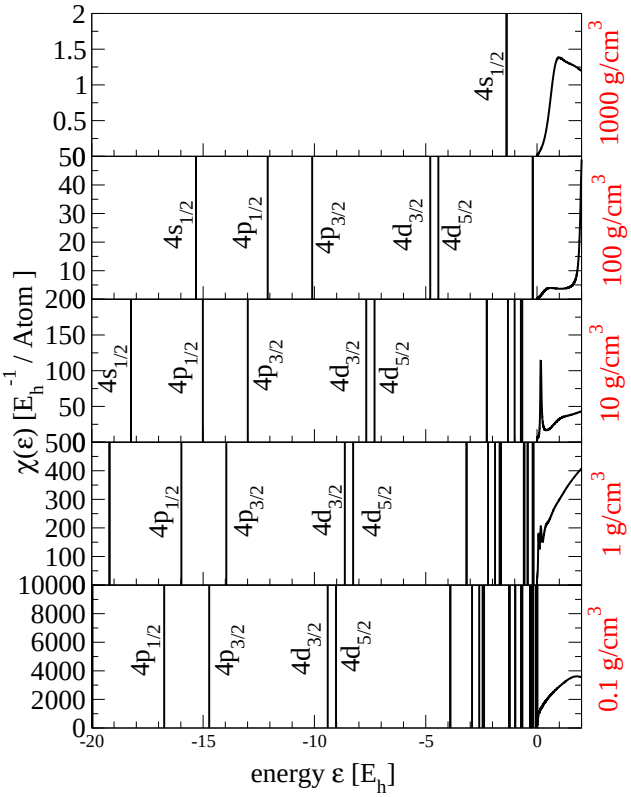

Figure 3.6: Density of states $\chi(\epsilon)$ for lutetium at 10 eV for real energy ϵ.

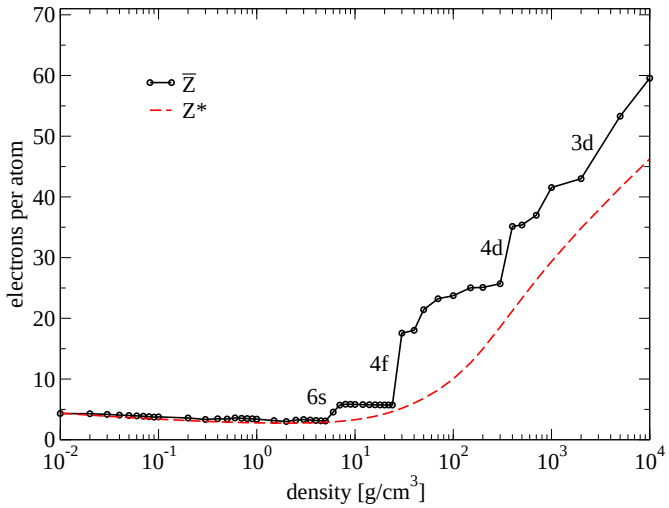

Figure 3.7: Average ionization of lutetium at 10 eV. Two definitions are explored. Note that the definition choice does not affect in any way the properties of the average atom, for example, the equation of state does not depend on the definition. For $\bar{Z}$ the more prominent ionization features are labelled.

3.5.2 Extraction of Ionization

A quantity of interest is the average ionization in the plasma. This is quantity is not uniquely definable, but given a definition it can be calculated from `Tartatus`. We stress that the ionization definition has no bearing on the model, it does not influence in any way the results for the self-consistent solution or the equation of state. Here we explore two definitions. The first is the number of positive energy electrons $\bar{Z}$, defined as

$$\begin{aligned}\bar{Z} &= Z - \int_0^R dr \sum_{i\in B} f(\epsilon_i,\mu) 2|\kappa_i|[P^2_{\kappa_i}(r,\epsilon_i) + Q^2_{\kappa_i}(r,\epsilon_i)] \\ &= \int_0^R dr \int_0^\infty d\epsilon f(\epsilon,\mu) \sum_{\substack{\kappa=-\infty \\ \kappa\neq 0}}^{+\infty} 2|\kappa|[P^2_\kappa(r,\epsilon) + Q^2_\kappa(r,\epsilon)] \end{aligned} \tag{3.64}$$

The second definition is the number of free electrons per atom Z^*, i.e. given μ, T and V^{ion}, the number of electrons per atom in a free electron gas. This is given by $Z^* = n_e^0 V^{ion}$, where n_e^0 is given by equation (3.54). The first definition $\bar{Z}$ has the benefit that it gives the expected ionization in seemingly clear cut cases: for example $\bar{Z} = 3$ for aluminum under normal conditions. However it has the major disadvantage that it is generally discontinuous across a pressure ionization. When a state is ionized it ceases to be included in the bound state sum, and instantly is counted in $\bar{Z}$. In reality the ionized state retains some of its bound like character if it appears as a resonance. These meta-stable resonance states are treated as fully ionized in the $\bar{Z}$ definition. In figure 3.7 such discontinuities are observed for a lutetium 10 eV isotherm.

The second definition does not recover the expected ionization in cases like normal density aluminum, where $Z^* \approx 2$. However it is smooth across a pressure ionization because the chemical potential μ is smooth, as it must be (figure 3.7). Depending on the application one can choose the definition that best suits. But it important to keep in mind that the ionization depends on the definition.

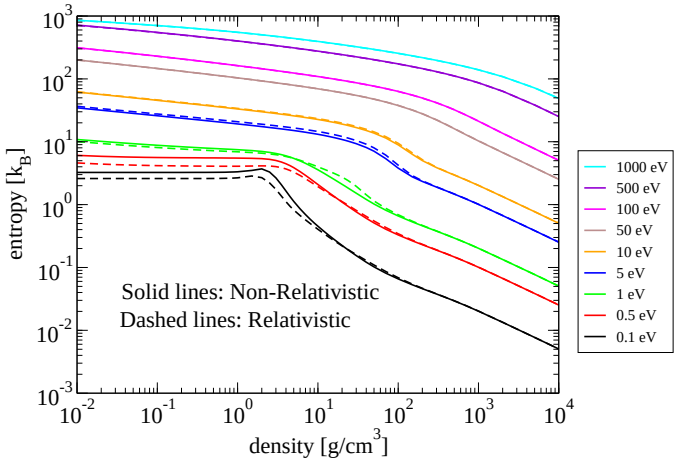

Figure 3.8: Isotherms of entropy of lutetium plasma from `Tartarus`. Both non-relativistic (solid lines) and relativistic (dashed lines) are shown for temperatures from 0.1 eV to 1 keV. For any given density the entropy increases with temperature, as expected.

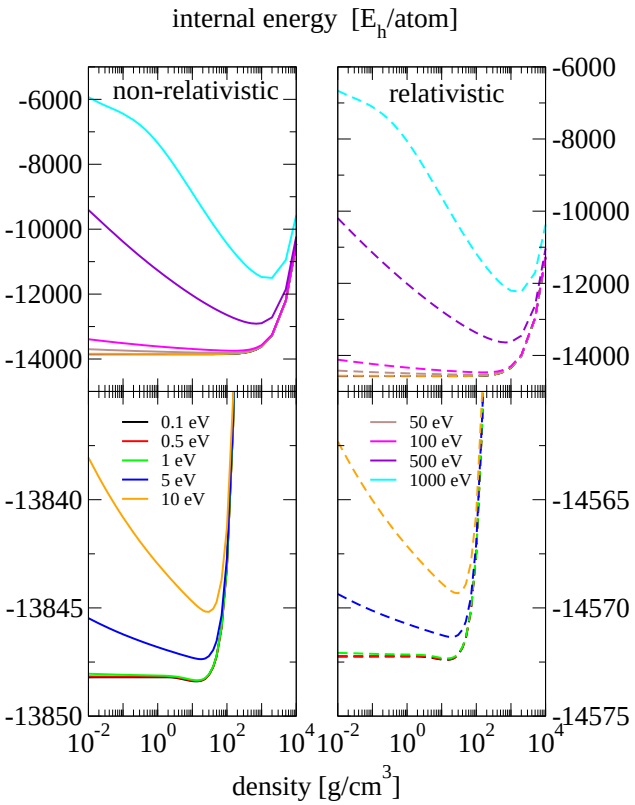

Figure 3.9: Isotherms of internal energy of lutetium plasmas from `Tartarus`. Both non-relativistic (solid lines) and relativistic (dashed lines) are shown for temperatures from 0.1 eV to 1 keV.

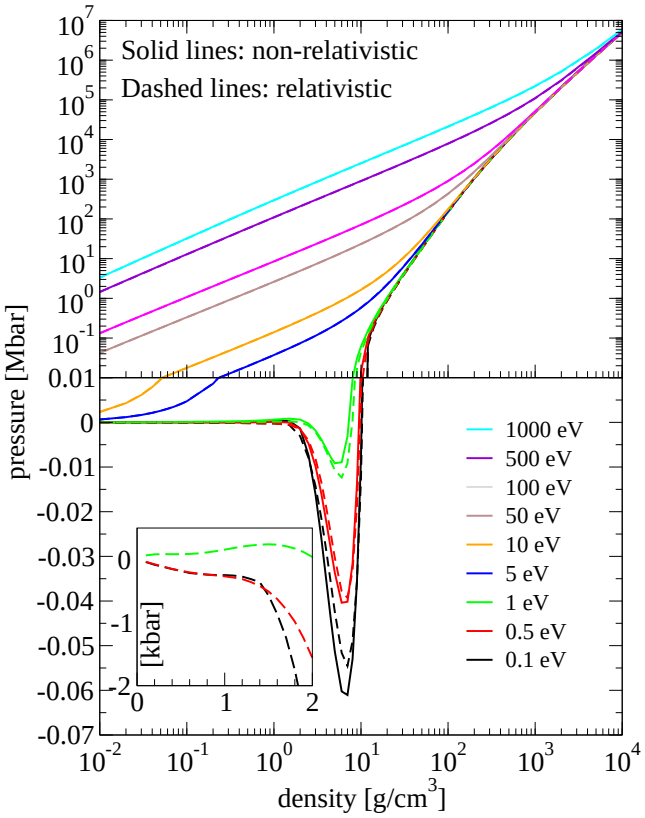

Figure 3.10: Electron pressure of lutetium plasmas along isotherms. Both relativistic and non-relativistic results are shown. The inset also shows electron pressure but focused on the low temperature region where entropy increases with density for fixed temperature. The result is a region where pressure increases as temperature is lowered, for a fixed density.

3.6 Case Study: Equation of State of Lutetium

We now focus of an application of `Tartarus` to the equation of state of a high Z material (lutetium, Z = 71), from 0.1 to 1000 eV and $1/1000^{th}$ to 1000 times solid density ($\approx$ 10 g/cm^3).

In figure 3.8 entropy (S) isotherms are shown for both relativistic and non-relativistic calculations. For a given density S increases with temperature, as expected. For $k_BT \geq 1$ eV S always decreases as density is increased, again as expected. However for $k_BT < 1$ eV there is a region near normal density where the model predicts that S increases with density. This physically unexpected behavior is not numerical inaccuracy but a consequence of the physical assumptions of the model [76]. This behaviour is caused by the inconsistency between the normalization integral (3.18), which is over all space, and the cell neutrality condition (3.3). When a bound state has significant probability outside the ion sphere, the number of electrons that bound state can contain becomes less that $2(2l + 1)$ (non-relativistically). The left-over electrons are forced into the positive energy states leading to an increase in S. When the temperature is high enough this effect still occurs but is overwhelmed by the entropy of the other ionized electrons.

The effect of relativity is generally modest, but it does make a significant difference at low temperatures and densities. This is because S is dominated by the density of states near $\epsilon = \mu$ at low temperature. For low densities the splitting of spin degeneracy in the Dirac equation results in the non-relativistic $5p$ state becoming a $5p_{\frac{1}{2}}$ and $5p_{\frac{3}{2}}$, resulting in a change in the eigenvalue and therefore μ. For higher densities, but still at low temperatures, $\mu > 0$ and the splitting has a smaller effect since the eigenvalues are continuous.

For internal energy the results are shown in figure 3.9. There is a significant change in going from non-relativistic to relativistic due to significant relativistic effects on the most tightly bound states. At 0.1 eV, 10 g/cm^3 the eigenenergy of the $1s$ state changes from -2146.4 E$_h$ to -2318.8 E$_h$. Note that $|\epsilon_{1s}|/mc^2 \approx 0.12$, so a significant relativistic effect is expected.

In figure 3.10 the pressure due to electrons (i.e. no ideal ion contribution is added) is shown. In the top panel the relativistic and non-relativistic results are barely distinguishable

on the log-log scale. The bottom panel shows the same data but on a linear pressure scale and focused on the low pressure region. For $k_B T \leq 1$ eV there is a region of negative pressure akin to the Van der Waal's loops phenomena, and is indicative of unstable liquid-gas coexistence. In figure 3.11 the electron pressure divided by that of a fully ionized ideal electron system is shown. The maximum value that this quantity can take is 1. Even at 10^{-2} g/cm^3 and 1000 eV the normalized pressure is only ≈ 0.85. Under these conditions the $1s_{1/2}$ and $2s_{1/2}$ states have eigenvalues of -2514.132 E_h and -575.749 E_h respectively and μ = -420.128 E_h, so that the Fermi-Dirac occupation factors are 1.000 and 0.986, i.e. nearly completely full. Hence the reduction in pressure from the fully ionized gas.

The Maxwell relation

$$\left.\frac{\partial S}{\partial V}\right|_T = \left.\frac{\partial P}{\partial T}\right|_V \tag{3.65}$$

implies that the increase in S with density for low temperatures observed in figure 3.8 should correspond to a region where the pressure P decreases as temperature increases, at constant density. In the inset in figure 3.10 such an effect is observed. It is only seen for low temperatures and only over the limited region in which $\left.\frac{\partial S}{\partial V}\right|_T$ is negative. Such a behavior is likely to be an artifact of the model. This low temperature metal-to-nonmetal transition region is difficult to model accurately and the present one-atom, spherically symmetric model cannot be expected to fully capture this physics, though it clearly captures the gross effect.

In figure 3.11 we also observe a minimum in the normalized pressure. This corresponds to a minimum in ionization Z^* (see figure 3.13). Ionized electrons are the main cause of electronic pressure [58]. The ionization increases with density for high densities due to pressure ionization, a process analogous to the raising of energy levels in a square well potential as the length of the square well is decreased. Bound states disappear with increasing density and there are insufficient bound states to hold all the electrons, so they are forced into positive energy states, i.e. ionized. At low densities, average ionization increases as density is lowered. In this case there are enough electron states to hold all the electrons but their Fermi-Dirac occupation factors become < 1. This arises from the fact that the bound states approach their isolated atom limit, and hence become insensitive to changes in density, however, the chemical

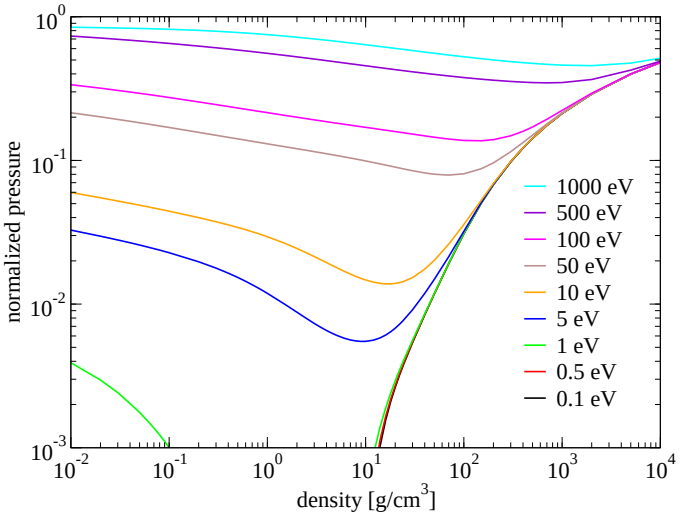

Figure 3.11: Electron pressure for lutetium divided by the pressure of a non-interacting, relativistic, quantum electron gas with electron density Z/V^{ion}.

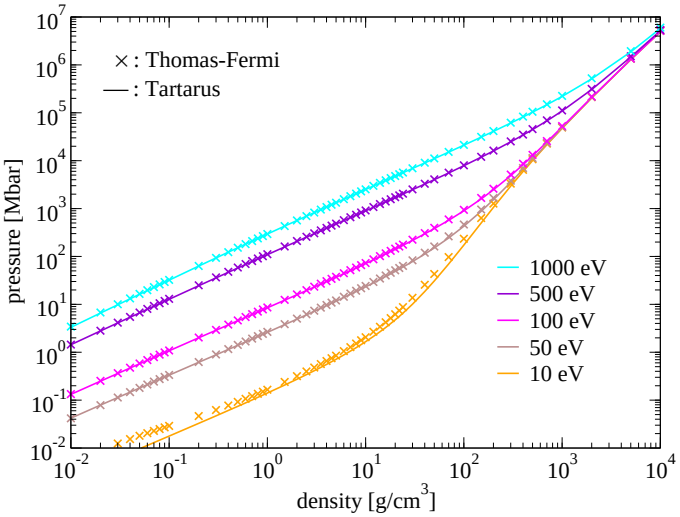

Figure 3.12: Electron pressure for lutetium from `Tartarus` (relativistic) compared the Thomas-Fermi model's prediction [5]. Note we have used the same exchange and correlation potential for both [6].

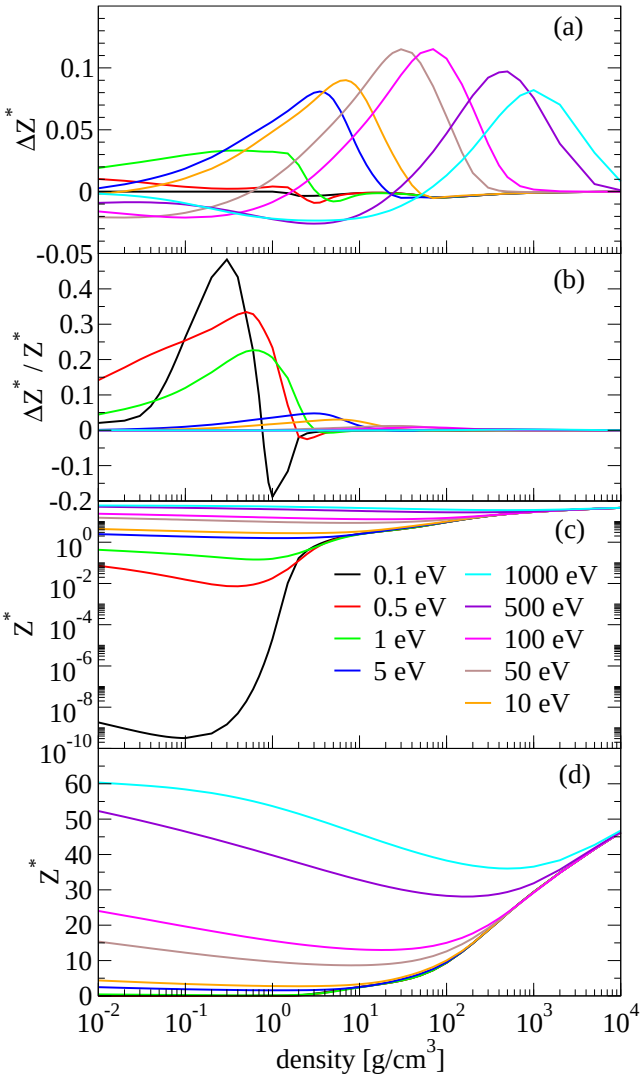

Figure 3.13: The effect of finite temperature exchange and correlation on the average ionization per atom Z^*. We compare the zero temperature Perdew-Zunger (PZ) functional [6] to the recent finite temperature functional [7] (here labeled QMC17). In the panel (a) we show $\Delta Z^* = Z^*$(PZ) - Z^*(QMC17), in panel (b) we show $\Delta Z^*/Z^*$, where Z^* is calculated with PZ. The bottom two panels (c) and (d) show the same Z^*(PZ) but on different scales.

potential continues to decrease, leading to smaller Fermi-Dirac occupations factors for the same state. The physical process underlying this is photo ionization. Though there are no radiation fields explicitly included in the model's Hamiltonian, the assumption of local thermodynamical equilibrium implies that the radiation temperature is equal to the electron temperature. This is embedded in the Fermi-Dirac occupation factor, which does appear explicitly in the model.

In figure 3.12 we compare the electron pressure from `Tartarus` to the generalized Thomas-Fermi (TF) model [5], using the same exchange and correlation potential [6]. The TF model is commonly used to construct equation of state tables [77, 78], however it has a number of well known drawbacks. For example, it does not have shell structure and as a consequence its internal energy is quite inaccurate. However it is expected to give the correct pressure at high temperatures and densities. In the figure we observe good agreement of the `Tartarus` electron pressure with the TF model for high temperatures and densities, in line with this expectation. Note that for truly free electrons the two models become identical. For the lowest temperature in the figure, 10 eV, significant deviations between the models is seen due to the neglect of shell structure in the TF model. The agreement between `Tartarus` and the TF model is a validation of our implementation in those limits.

All of the results so far presented have used a zero temperature local density approximation (LDA) exchange and correlation functional F^{xc} [6]. Recently, new temperature dependent LDA functionals have become available [79, 7]. This temperature dependence has shown a correction of several percent in the total pressure for some low Z systems in the warm dense matter regime [80]. In figure 3.13 the effect on Z^* of using a temperature dependent F^{xc} is plotted. We have used the functional of Groth *et al* [7]. The top panel shows the absolute change in Z^* (in number of electrons per atom). The effect is generally quite modest, with $|\Delta Z^*| \lessapprox 0.1$. In panel (b) the relative change in Z^* is plotted. For $k_B > 50$ eV the effect is $\lessapprox 1$ %. At high temperatures exchange and correlation effects become relatively small, compared to the kinetic energy, as the system becomes more ionized and therefore more like an ideal non-interacting quantum electron gas. At lower temperatures the relative effect of F^{xc} is quite large, approaching 50 % at 0.1 eV. However, in this region the absolute size of Z^* is very small (see panels (c) and (d)). The most significant effect is at ≈ 1 eV and near solid density where

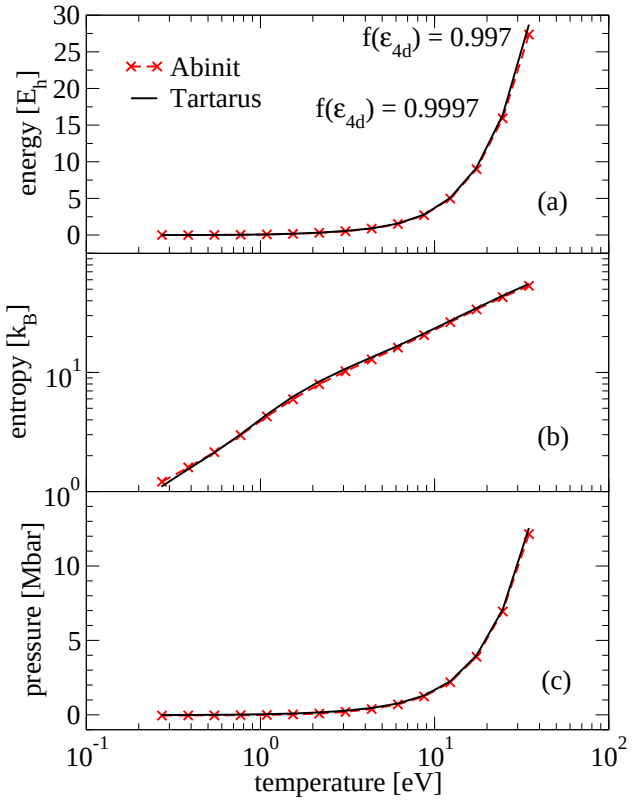

Figure 3.14: Isocore (9.773 g/cm^3) of lutetium comparing results from the Abinit plane wave code using a HCP crystal structure to Tartarus results.

both the relative and absolute change in Z^* are appreciable. This is sometimes called the warm dense matter regime, and is characterized by significant changes in electronic structure brought about by pressure ionization.

We now turn to a comparison with a less approximate method. We have used the plane wave code Abinit [81, 82] to simulate HCP lutetium. This is a DFT based code that does not assume spherical symmetry. It has two principle drawbacks for making EOS tables: First, it uses a pseudopotential to represent the core electrons. We have used the PAW pseudopotential [83, 84] and converged our results with respect to number of bands and cutoff radius. In this pseudopotential the electron core states up to and including 4d are included. The Pseudopotential is used to reduce the computational cost of the method and should be accurate provided the states in the pseudopotential are not active (eg. not significantly ionized or the eigenvalue of the state has not changed significantly). Hence there is always a region of accuracy for a given pseudopotential and results outside this range are unreliable. Second, the method becomes increasingly expensive with increasing temperature and eventually this become prohibitive.

In figure 3.14 we compare equation of state from Tartarus to Abinit for lutetium at solid density for temperature from ≈ 0.25 eV to ≈ 25 eV. Overall, there is a remarkable level of agreement between the to methods. For internal energy (panel (a)) some differences appear at the two highest temperature points. For these points we have noted the value of the Fermi-Dirac occupation factor as calculated in Tartarus for the 4d state. Clearly this state is beginning to be temperature ionized, indicating that the pseudopotential used in the Abinit calculations is near the limit of its validity, and is likely the cause of the difference seen. For entropy (panel (b)) small differences between the models are apparent. It is not surprising that the spherically symmetric average atom model that does not explicitly account for crystal structure fails to exactly reproduce the less approximate plane wave code. Nevertheless, despite these approximations the level of agreement seen is very good. For pressure (panel (c)) the agreement is again excellent, with the only significant differences appearing at high temperature, again likely due to the pseudopotential.

In figure 3.15 we again compare Tartarus to Abinit. Here we compare the so-called cold curve. This is an isotherm at room temperature (0.0285 eV). A common method in making

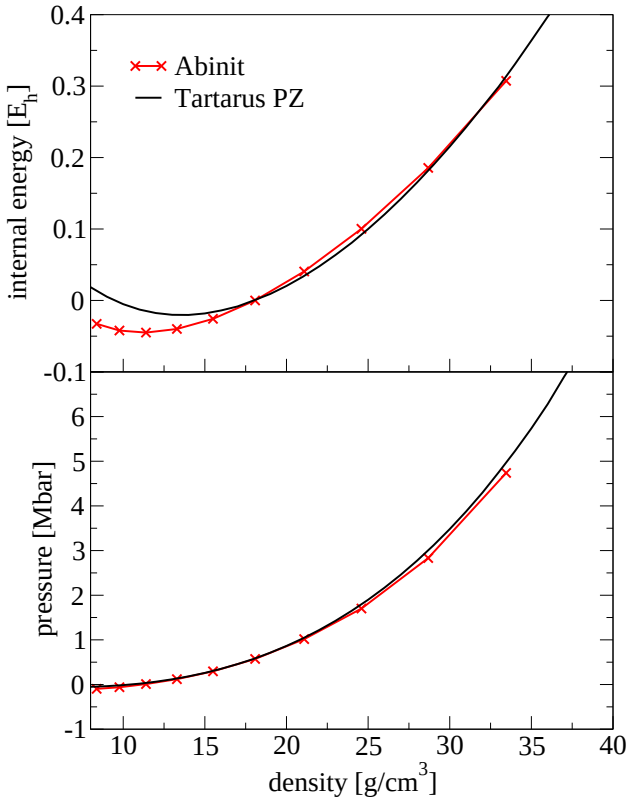

Figure 3.15: Isotherm (0.0285 eV) for lutetium compared to the plane wave code Abinit using the HCP crystal structure.

EOS tables is to use average atom calculations for the change in the EOS due to increase in temperature (for a given density) only. To do this the cold curve is subtracted from the average atom model and a calculation using a more realistic model designed to accurately calculate the EOS at room temperature is added back in. In the figure we can see that there are significant differences between the models for internal energy, approaching 0.04 E_h at normal density. Perhaps more importantly is that the trends as a function of density are not well reproduced by the simpler model. It is worth noting that such absolute differences would not be apparent if plotted on the same scale as figure 3.14. The point being that while `t`artarus clearly gets large scale trends correct, smaller scale trends may be incorrect.

For pressure, figure 3.15, the agreement is reasonable on the scale of the figure. The pressure shown is calculated using the virial expression, equation (3.39). It is also possible to calculate the pressure by taking a numerical derivative of the free energy F

$$P = -\left.\frac{\partial F}{\partial V}\right|_T \tag{3.66}$$

As is well documented [39, 47], the physical model that `T`artarus uses does not guarantee the these two pressures will be identical. In figure 3.16 we show the pressure calculated both these ways for three isotherms of lutetium. For the cold curve (0.0285 eV) significant differences are observed. By 10 eV the differences are largely gone but show up at the highest densities. At 50 eV the agreement between the two pressures is very good. Generally differences appear where oscillations in the electron density have not died out by the sphere boundary. Such oscillations are a consequence of a sharp Fermi-Dirac distribution which occurs in degenerate systems and are called Friedel oscillations. The figure reflects this: the larges differences are seen for the most degenerate systems (i.e. low temperature and high density).

Such an inherent thermodynamic inconsistency may or may not be problematic depending on the application of the model. A practical solution is to just use the free energy to generate the entire EOS through numerical derivatives. Such an approach generates other problems, principally that the free energy must be smooth enough for the derivatives to be accurate. For

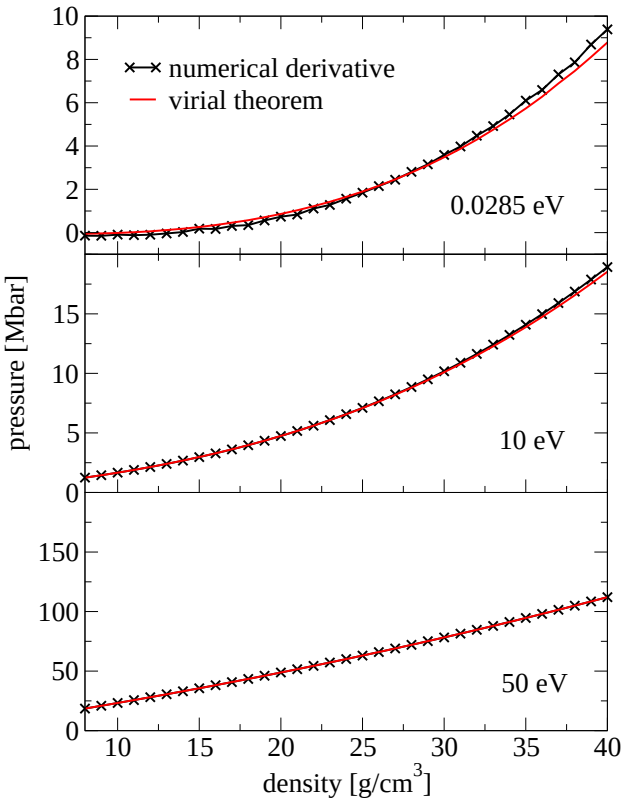

Figure 3.16: Comparison of pressures from Tartarus for lutetium calculated with the virial expression (3.39) and via a numerical differentiation of the free energy $P = -\partial F/\partial V|_T$.

many applications however, such inconsistency is not particularly problematic. We note that a thermodynamical consistent average atom is possible [44, 47].

3.7 Conclusions

We have presented a detailed discussion of the physics model and numerical implementation of the Tartarus average atom code. The model is based on a hybrid orbital and Green's function implementation and the advantages of such a scheme are presented. A numerically efficient method of solving the self consistent field problem is also given. It is hoped that this presentation may guide others in their own implementations.

We then focus on the application of the model to a lutetium plasma for a wide range of conditions. We use this example to explain concepts such as broadening of the density of states in the complex energy plane, and prediction of ionization. The effect of relativity on the wide ranging EOS is also presented. It is found that relativity is generally a small effect, but is important for internal energy, and for entropy at low temperature and density.

The effect of finite temperature exchange and correlation potentials is also investigated. It is found the effect is generally small, but becomes relatively significant for warm dense matter conditions, i.e. near normal density and temperature around 1 eV.

A comparison of the model to a more physically realistic model at low temperatures reveals the Tartarus model is generally in excellent agreement with the more physically accurate model, but that smaller scale deviations are apparent.

Some oddities of the model are discussed. We find that an increase in entropy near normal density along at low temperature isotherm corresponds to a region where pressure decreases as temperature increases, for fixed density. This artifact of the model occurs in a small region, at low temperature where the material is transitioning from metal to non-metal. Also, thermodynamic inconsistency for highly degenerate materials is discussed.

In summary, the hybrid orbital/Green's function approach to the average atom model was found to be very stable numerically and is recommended for future implementations.

Chapter 4

Mean-Force Scattering Potential for Calculating Optical Properties of Dense Plasmas

4.1 Abstract

We assess the relative importance of ionic structure on the opacity of dense plasmas by using the potential of mean force as a scattering potential within the Kubo-Greenwood formalism. We compare results from the potential of mean force, which includes realistic ionic structure, to results using an average atom potential, which includes only a crude treatment of ionic structure. Comparisons with less approximate but more expensive DFT-MD simulations for aluminum plasma reveal that the mean force generally improves agreement for DC conductivity. We also see improvement when applying the mean force to free-free transitions, whereas for bound-bound and bound-free transitions the mean force leads to poorer agreement on transition energies. Further, we assess the impact of accounting for correlations within the plasma at the temperature and density conditions relevant to iron opacity measurements at Sandia's Z machine facility [Bailey et al., Nature 517:56-59, 2015] and find that these correlations do not account for the discrepancy between the measurements and leading opacity calculations.

4.2 Introduction

The radiative properties of dense matter are important for many active areas of research, including the solar composition problem [85, 86, 87], simulations of white dwarf stars [88], and simulations of inertial confinement fusion experiments [10, 89]. Calculating these properties, such as the electrical conductivity and the opacity, in dense systems has proven challenging. At

high material densities and for temperatures below the Fermi temperature, one type of physically robust calculation involves using the Kubo-Greenwood formalism within a density functional theory molecular dynamics (DFT-MD) simulation [90, 91, 49, 92, 10, 8]. Though these calculations are considered accurate, they are computationally expensive and therefore there is need for more computationally efficient calculations applicable to a wide range of systems.

Recent experiments at the Sandia Z machine [12] have revealed a large discrepancy with state-of-the-art opacity calculations [93, 94, 95, 96], with the calculations consistently underpredicting the observed data. This has led to a search for physics that may be missing from the opacity models. One such effect that is not fully explored in modern opacity calculations is the impact of the other ions in the plasma on the electronic structure and resulting radiative properties. The optical properties of the plasma change continuously as the density of the plasma increases, meaning that effects such as continuum lowering must be modeled. Further the effects of collisions with other ions must be accounted for to fully characterize the impact of the plasma environment.

Average atom and other closely related models are computationally efficient, DFT based models that have long been used to determine various plasma properties [26, 47, 46, 97, 67, 98]. The average atom model accounts for continuum lowering self-consistently through its definition of the ion sphere and consistent treatment of bound and continuum electronic states.

Using the average atom model developed by Starrett and Saumon [28, 1], a realistic ionic structure that compares well to experiment [99] and DFT-MD simulations can be determined. It was shown by Starrett [9] that, using this average atom model as a basis, a potential of mean force could be developed that gives accurate values for the zero frequency (DC) conductivity. This potential is formed using the quantum Ornstein-Zernike equations with the electronic structure determined by the average atom calculation [28, 9] and accounts for the correlations with the surrounding electrons and ions in the plasma. Given the impact that use of the potential of mean force has on the DC conductivity, it is natural to think it may have a considerable impact on the frequency-dependent AC conductivity and the opacity. In this work we assess the importance of correlations with other ions in the plasma by using this potential of mean

force. We use this potential to determine the electronic states and associated matrix elements needed in the calculation of conductivity within the Kubo-Greenwood formalism.

As the calculations presented are only semi-quantitative due to the reliance on DFT and the average atom model [100], we will be looking at trends of behavior that can indicate the importance of accounting for a realistic ionic structure. We do this by comparing the results for the opacity calculated with the average atom potential to those with the potential of mean force which has the ionic structure built into it. By determining the differences in the behavior of the opacity results from the average atom and mean force approaches, we can gain insight into the effect of ionic structure on the opacity. In particular we assess the impact of those correlations for the iron plasma at conditions relevant to the Bailey et al. experiment.

This chapter is organized in the following way. In Section 2 we present the main expressions that define the scattering potentials used in this work, namely the average atom potential and the potential of mean force as described in Reference [9]. From there we give the Kubo-Greenwood expression for the conductivity and describe how the opacity is determined from the conductivity. In Section 3 we first compare our results for the DC conductivity to DFT-MD simulations. Next we present the AC conductivity of our methods compared to DFT-MD. We then show that both the average atom model and mean force calculations obey the f-sum rule. Finally we present the opacity calculated with the mean force potential compared to the average atom model. We do this for several temperatures and densities of aluminum, deuterium, and iron.

4.3 Theory

4.3.1 Average Atom Potential

In our average atom calculations, the effective electronic potential is solved for self-consistently within the confines of an ion sphere whose volume is defined according to

$$n_i^0 = V_{ion}^{-1} = \left(\frac{4\pi}{3} R_{is}^3\right)^{-1} \tag{4.1}$$

where n_i^0 is the ion density of the plasma and R_{is} is the radius of the ion sphere [1, 26, 46], which is required to be charge neutral. The potential arising from this self-consistent calculation is given by

$$V_{eff}^{AA}(r) = -\frac{Z}{r} + \int_{V_{ion}} d\vec{r'} \frac{n_e^{AA}(r')}{|\vec{r} - \vec{r'}|} + V^{xc}[n_e^{AA}(r)] \tag{4.2}$$

where Z is the nuclear charge, n_e^{AA} is the electron number density coming from the average atom electronic wavefunctions, and V^{xc} is the exchange correlation potential arising from the choice of exchange-correlation functional. V_{eff}^{AA} represents the effective potential seen by the electrons within the ion sphere and is enforced to be zero for $r > R_{is}$. This has been used to calculate the opacity previously [100]. Though the model provides reasonable results, it has only a crude treatment of the surrounding ions through the definition of the ion sphere.

4.3.2 Potential of Mean Force

In order to more realistically account for the influence of the surrounding ions in the plasma, we use the quantum Ornstein-Zernike equations to determine a potential of mean force that is felt by the electrons. This potential accounts for the interaction of the electron with the central ion as well as ions and electrons in the surrounding plasma, and by the nature of the ionic correlations, this potential is not confined to the ion-sphere. The expression for the resulting scattering potential is given as

$$V^{MF}(r) = V_{ie}(r) + n_i^0 \int d\vec{r'} \frac{C_{ie}(|\vec{r} - \vec{r'}|)}{-\beta} h_{ii}(r')$$

$$+ \bar{n_e^0} \int d\vec{r'} \frac{C_{ee}(|\vec{r} - \vec{r'}|)}{-\beta} h_{ie}(r') \tag{4.3}$$

where V_{ie} is the potential that includes interactions between the electron and the central nucleus and other electrons in the central ion, $\bar{n_e^0}$ is the free electron density, $C_{ie}(C_{ee})$ is the electron-ion (-electron) direct correlation function from the quantum Ornstein Zernike equations, $\beta = \frac{1}{k_B T}$, and $h_{ii}(h_{ie})$ is the pair correlation function corresponding to the ion-ion (-electron) pair. The

pair correlation function is simply related to the radial distribution function $g_x(r)$ by

$$h_x(r) = g_x(r) - 1 \tag{4.4}$$

Additionally, the pair correlation function can be easily used to determine the structure factor of the system

$$S_{ii}(k) = 1 + n_i^0 h_{ii}(k) \tag{4.5}$$

where S_{ii} is the ion-ion structure factor and $h_{ii}(k)$ is the Fourier transform of the real-space ion-ion pair correlation function, dependent on wave number k. Thus through h_{ii} the ionic structure is implicitly included in the potential of mean force. Details on the determination of V^{MF} and how it differs from V_{eff}^{AA} can be found in Ref [9].

Though all of the components used to construct V^{MF} in equation 4.3 are determined self-consistently, V^{MF} and the resulting electronic states are not self-consistent. This is due to the difficulty in defining a set of physical constraints within which V^{MF} can be self-consistently determined. Unlike V_{eff}^{AA}, which is determined within the confines of a charge neutral sphere of radius R_{is}, V^{MF} extends throughout all space, having a nonzero value within the volumes of other ions in the plasma. Self-consistent definitions of a potential of mean force have been developed, namely by Chihara [32]. However, such chemical models suffer from issues when applied to plasmas.

4.3.3 Optical Properties

The main interest of this chapter is to address the effect that accounting for ion correlations through the effective electronic potential has on the optical properties of the plasma, namely the opacity and the optical conductivity. The optical conductivity $\sigma(\omega)$ can be determined from the average atom model via the Kubo-Greenwood formalism [63] by the following expression

$$\sigma_1(\omega) = \frac{1}{\omega^2+\gamma^2}\frac{2\pi n_i^0}{\omega}\sum_{ij}\Big(f(E_i,\mu) - f(E_j,\mu)\Big) \times \left|\langle\psi_j|\frac{\partial V_{eff}}{\partial r}|\psi_i\rangle\right|^2 \delta(E_j - E_i - \omega) \quad (4.6)$$

where we have represented the matrix element in the acceleration gauge, the index $i(j)$ corresponds to the initial (final) state of the electron within the context of a photoexcitation of energy $\hbar\omega$, and γ is a renormalization constant that accounts for a finite lifetime of the scattered state. The renormalization constant is determined by forcing the following sum rule to be satisfied

$$\int_0^\infty \sigma^{ff}(\omega)d\omega = \frac{\pi e^2 \bar{n}_e^0}{2m_e} \quad (4.7)$$

where σ^{ff} is the part of the conductivity arising from free-free transitions and m_e is the mass of the electron [63, 101].

The conductivity is dependent on both the electronic wavefunctions and the spatial variation of the effective potential seen by the electrons. When comparing the optical conductivity as calculated by the average atom model and the mean force model, we need only determine the orbitals resulting from each potential and calculate the matrix element in Equation 4.6:

$$\langle\psi_j^{AA}|\frac{\partial V_{eff}^{AA}}{\partial r}|\psi_i^{AA}\rangle \rightarrow \langle\psi_j^{MF}|\frac{\partial V^{MF}}{\partial r}|\psi_i^{MF}\rangle \quad (4.8)$$

Equation 4.6 can also be formulated with explicit dependence on the ionic structure factor (see, for example, Ref [102]). When using the potential of mean force, the structure factor is implicitly present in the structure of the potential and thus does not need to be explicitly included in equation 4.6. In the V_{eff}^{AA} calculation with explicit $S(k)$ dependence, only the free-free profile is modified by the ionic structure of the plasma, but the implicit inclusion of ionic structure within the mean force potential means that both the continuum and bound states are affected consistently by the other ions in the plasma. Except where otherwise noted, the

average atom model results presented in this work set $S(k) = 1$ so that we can gain a clearer understanding of the true importance of the plasma's ionic structure.

So far we have presented the method for determining the real part of the optical conductivity, σ_1, but in order to determine the opacity from this calculation we also require the imaginary part of the conductivity, σ_2. This can be obtained from the real part of the conductivity via a Kramers-Kronig relation [63, 100]. With both the real and imaginary parts of the conductivity available, we can determine the dielectric function ϵ via

$$\epsilon(\omega) = 1 + \imath \frac{4\pi\sigma(\omega)}{\omega} \tag{4.9}$$

where $\sigma = \sigma_1 + \imath\sigma_2$ is the complex optical conductivity. With the complex dielectric function determined, we can determine the index of refraction, $n(\omega)$ for the plasma

$$n(\omega) = \sqrt{\frac{\Re\epsilon(\omega) + |\epsilon(\omega)|}{2}} \tag{4.10}$$

Finally we can use the index of refraction to determine the absorption coefficient $\alpha(\omega)$ which, in media where intensity loss from scattering can be ignored such as those we are dealing with in this work, is equivalent to the opacity. The absorption coefficient is related to the real part of the optical conductivity and the index refraction according to

$$\alpha(\omega) = \frac{4\pi\sigma_1(\omega)}{n(\omega)c} \tag{4.11}$$

where c is the speed of light in vacuum [63, 100].

Throughout this chapter, our calculations are done using the exchange-correlation functional developed by Groth et al. [7] and is labeled "qmc17" in our figures.

4.4 Results

4.4.1 DC Conductivity

Using the Kubo-Greenwood average atom and mean force formalisms as detailed in the previous section, we have calculated the optical conductivity at $\omega = 0$, i.e. the DC conductivity. We compare our results to the less approximate but costly DFT-MD calculations of Witte et al. [8] in figure 4.1 as a function of temperature. The V_{eff}^{AA} results generally show a significant over-prediction of the DC conductivity compared to the DFT-MD results, however there is a clear improvement in agreement as temperature increases. With explicit use of $S(k)$ in the V_{eff}^{AA} calculation, we see worse agreement than when we set $S(k) = 1$.

When we compare the results of our calculation using the mean force scattering potential, we see much better agreement with the DFT-MD results for the higher temperatures. Above 3 eV the mean force calculation has excellent agreement with both the HSE and PBE DFT-MD results. The choice of exchange-correlation functional becomes less important to the DC conductivity in this regime as the two DFT-MD results become practically indistinguishable. We also see the dependence on exchange-correlation functional becoming less important at higher temperatures in our results (not shown in the figure).

For both the V_{eff}^{AA} and V^{MF} calculations, we still see large discrepancies at temperatures below 3 eV. This is possibly due to the renormalization of the Kubo-Greenwood integrals used in both models, as described in the previous section. When we use the mean force scattering potential in the relaxation time approximation as described in Reference [9], we see results that stay consistent with the DFT-MD results even at low temperatures. The relaxation time approximation does not use explicit renormalization, but is only applied to zero frequency calculations. Given that the scattering potential is the same in our Kubo-Greenwood calculation and the relaxation time approximation, this adds credence to the argument that our Kubo-Greenwood calculations have inaccurate behavior at low temperatures due to the renormalization introduced in the formalism used. The renormalization becomes less important at higher temperatures where the assumed Drude form used in the method is more physically representative of the system.

4.4.2 AC Conductivity

In figure 4.2 we compare our calculations with DFT-MD simulations [8] for the AC conductivity of aluminum at solid density. For the low temperature case of .5 eV, the V_{eff}^{AA} and V^{MF} calculations have qualitative agreement with the DFT-MD results. At 6 eV, V^{MF} yields an AC conductivity that is significantly different from V_{eff}^{AA}, but without significantly improved agreement with the DFT-MD results. As the temperature increases to 12 eV, the mean force calculation becomes more similar to the DFT-MD results and is a marked improvement over V^{AA} at practically all frequencies.

Let us address the position of the 2p-free edge in the top inset of figure 4.2. Clearly the V^{MF} results are in poorer agreement with DFT-MD than the V_{eff}^{AA} results. The choice of exchange-correlation functional could cause a difference in eigenvalues which would present itself as a frequency shift in the conductivity, though we expect that the results obtained using qmc17 should be close to the DFT-MD results obtained with PBE, and the same functional is used for both the V_{eff}^{AA} and V^{MF} calculations. Ideally we would use the same functional, but it is not currently possible to use PBE in our code. The likely source of the differences in the edge position seen in figure 4.2 could be the lack of self-consistency between V^{MF} and the resulting electronic states. This could lead to inaccurate eigenvalues for the electronic states and thus could explain the shift in the spectra for V^{MF} that we see.

There is also a difference in how we broaden our bound states compared to the DFT-MD calculations. Specifically this leads to an apparently missing 2s to 2p bound-bound feature (near 40 eV in the DFT-MD results) in our 12 eV temperature results in figure 4.2. Though this transition is seen in our calculations, the method we have implemented for broadening the bound states uses the average lifetime of the free states [63] and leads to an over-broadening of the transition. With this method the transition is too weak to show up on the scale used in figure 4.2. In the bottom inset of figure 4.2 we have forced the broadening of the bound states to be such that the conductivity resulting from the 2s to 2p resonance is comparable to that of Ref [8]. With this we see that our calculations do capture the bound-bound feature.

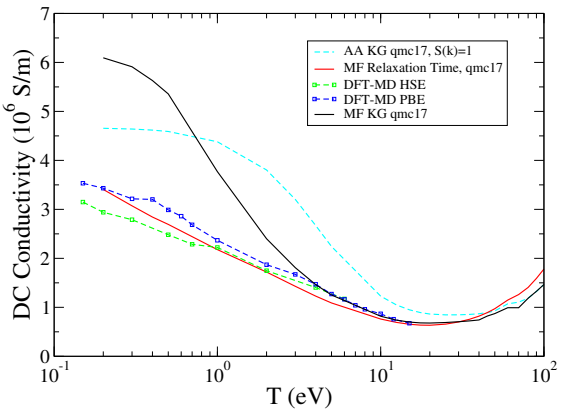

Figure 4.1: Here we compare the DC conductivity calculated with the average atom and mean force potentials with the results obtained by Witte et al. [8] for aluminum at solid density (2.7 g/cm^3). Witte et al. used finite-temperature DFT-MD with both the HSE and PBE functionals. We also show the results of a relaxation time approximation as is done in Ref [9] in the results labeled MF Relaxation Time.

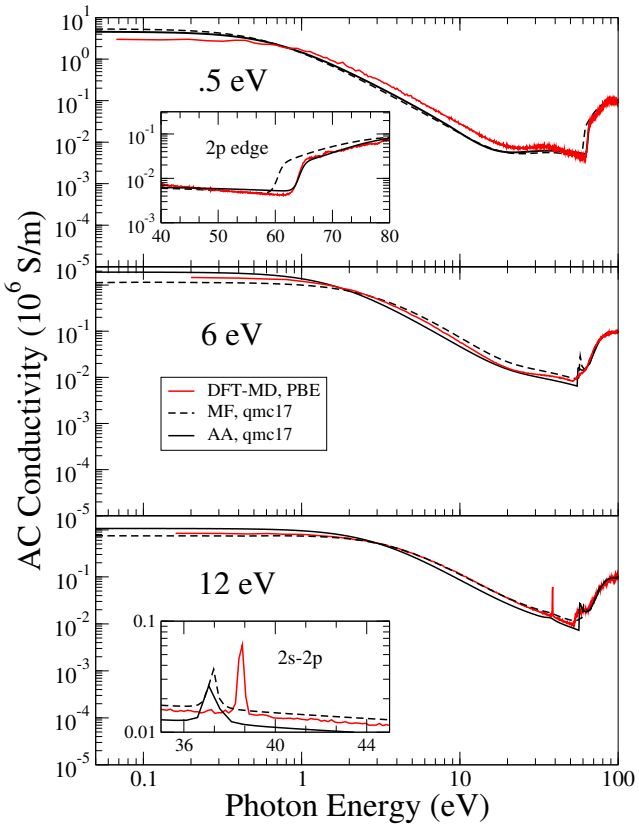

Figure 4.2: We compare the results of the V_{eff}^{AA} and V^{MF} calculations with the DFT-MD results of Witte et al. [8] for the AC conductivity of aluminum at solid density over several temperatures. The top inset shows the location of the 2p edge for the .5 eV case. We can see from this how the V^{MF} eigenvalues differ significantly from the DFT-MD and V^{AA} values. The bottom inset shows the mean force results with a broadened bound state width comparable to the DFT-MD results for the 12 eV case. The difference in the frequency location of the bound-bound transition feature is due to the different exchange-correlation functionals used in the two calculations. The inset axes are the same units as the main plot.

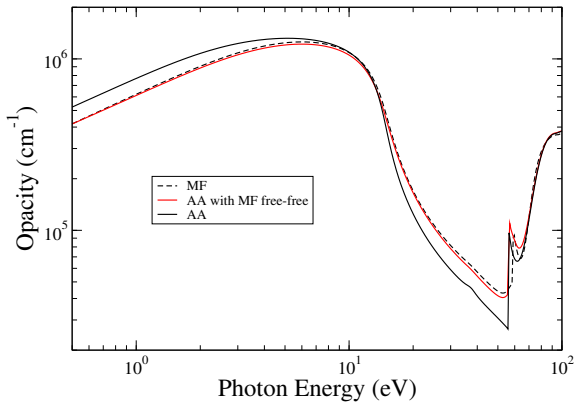

Figure 4.3: We compare the opacity as calculated with V_{eff}^{AA} and V^{MF} for aluminum at 10 eV and solid density. The red curve labeled "AA with MF free-free" uses the free-free part of the opacity calculated with V^{MF} and V_{eff}^{AA} bound-bound and bound-free parts of the opacity. We can see that the bound-bound and bound-free transitions are generally weakly affected by use of V^{MF}, and therefore have a small effect on the total opacity in contrast to the effect on free-free transitions.

4.4.3 Opacity

Deeply bound states are too tightly bound both spatially and energetically to see any significant changes due to ions in the plasma. High energy electrons see the surrounding ions as perturbative and thus show no significant changes in their electronic structure. As such the effects of ion correlations are most prominently seen in loosely bound states and low energy continuum states. In figure 4.3 we show the opacity for aluminum at 10 eV and solid density calculated with V^{MF}, V_{eff}^{AA}, and using the V_{eff}^{AA} results for the bound-bound and bound-free transitions with the V^{MF} free-free transitions. This illustrates the relative impact of the ion correlations on the free-free transitions as compared to the bound-bound and bound-free transitions. Though use of V^{MF} changes both the continuum and bound electronic states, we can see in figure 4.3 that the matrix elements associated with transitions between or from bound states are less affected by ion correlations, as expected from the above physical argument.

In figure 4.4 we show the opacity of deuterium plasma compared to the DFT-MD results of Hu et al [10]. For all cases tested the V^{MF} calculation yields results with improved agreement to the DFT-MD calculation compared with the V_{eff}^{AA} opacity. In particular, agreement in the most non-degenerate case (5.388 g/cm^3, 43.1 eV) is markedly improved, as was the case for aluminum (12 eV). The opacity shown here for deuterium arises entirely from free-free transitions in the plasma. The results in figure 4.4 and the previous results for AC and DC conductivity indicate that the V^{MF} calculation generally results in more accurate results for the free-free transitions. However, for bound-bound and bound-free transitions it is not clear that V^{MF} leads to any improvement.

An important test of any opacity model is that the f-sum rule for the imaginary part of the dielectric function is satisfied [103]

$$Z = \lim_{\omega\to\infty} \frac{1}{2\pi^2 n_i^0} \int_0^\omega d\omega' \omega' \Im\epsilon(\omega') \tag{4.12}$$

which can also be formulated in terms of the opacity, α, and the index of refraction, n, as

$$Z = \lim_{\omega\to\infty} \frac{c}{2\pi^2 n_i^0} \int_0^\omega d\omega' n(\omega')\alpha(\omega') \tag{4.13}$$

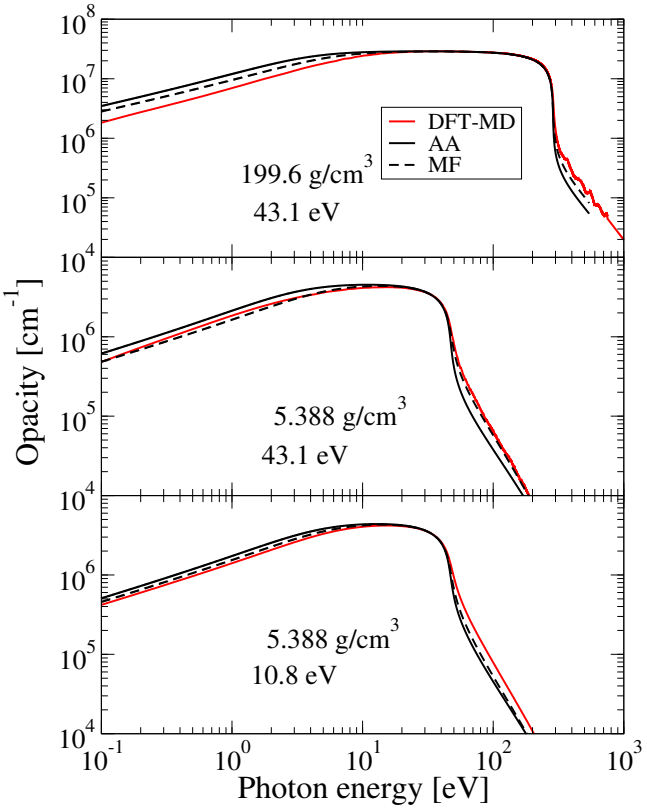

Figure 4.4: Opacity for deuterium at various densities and temperatures as compared to the DFT-MD results found in reference [10]. The V^{MF} results show improved agreement with the DFT-MD results compared to the V_{eff}^{AA} opacity. The opacity in this case is entirely due to free-free transitions.

In figure 4.5 we have shown the integral in equation 4.12 as a function of ω for aluminum at 1 eV and solid density. We can see that the correct number of electrons is being approached as $\omega \to \infty$ for both the V_{eff}^{AA} and V^{MF} calculations. The slight differences in the eigenvalues between the two calculations causes a small shift in the frequencies where integer number of electrons are reached, but otherwise the two calculations converge almost simultaneously to the correct number of total electrons.

4.4.4 Temperature and Density Effects on Ion-Correlation Features

In figure 4.6 we see the mass absorption coefficient (the opacity divided by the plasma mass density) for aluminum at various densities and temperatures. The influence of V^{MF} on the opacity is seen to have a complex relationship with the plasma environment. For solid density aluminum, we see very little effect at 1 eV, but the ion correlations begin to significantly change the free-free part of the opacity as the temperature is increased to 10 eV. When the temperature further increases to 20 eV, the V^{MF} results begin to approach the V_{eff}^{AA} results once again. At these higher temperatures, the electron's thermal energy is so high that they begin to see the fields from other ions in the plasma as weak perturbations.

Figure 4.6 also shows how the density influences the strength of ion correlations in the plasma. Though we see little impact from V^{MF} for the 1 eV, 2.7 g/cm^3 case, use of V^{MF} for the 1 eV, .027 g/cm^3 case shows a more significant effect on the opacity. At the highest temperatures the influence of V^{MF} is lessened as the electrons are less coupled to the surrounding plasma. The low density cases are marked by larger spacing between the ions thus leading to weaker coupling between the electrons and surrounding ions. Hence we expect the influence of ion correlations to be weaker on the absolute opacity, though there can still be significant impact on low-lying bound states which reappear in the low density cases. It is worth noting that in figure 4.6, the mass absorption coefficient is shown and the low frequency features in the .027 g/cm^3 case are due to the reappearing of a state that did not exist in the higher density system.

The plasma degeneracy factor, Θ, (the ratio of the thermal energy to the Fermi energy) and the plasma coupling parameter, Γ, (the ratio of the average Coulombic coupling to the thermal

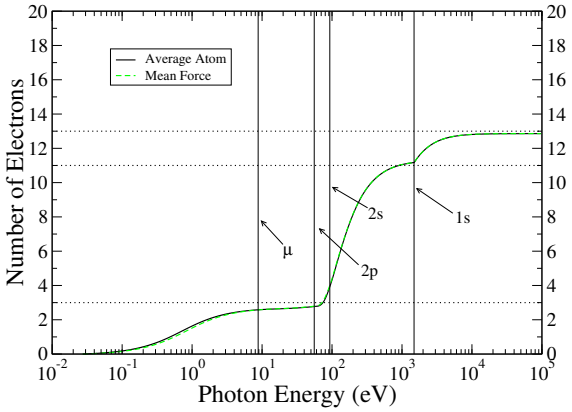

Figure 4.5: We show the f-sum rule for the opacity as a function of frequency for aluminum at 1 eV and solid density. The high frequency limit is the total number of electrons. The eigenvalues of the average atom electronic states are shown, as well as the chemical potential, μ, of the system, which is the same in both the V_{eff}^{AA} and V^{MF} calculation.

energy) are useful to quantify the plasma conditions where we see significant ion correlations. We show these parameters for the cases presented in figure 4.6, but the importance of the ion correlations do not follow any discernible trend among the degeneracy and plasma coupling parameters. These parameters do not sufficiently characterize the system as to indicate when ionic correlations at the level we account for them will be of relevance for optical properties.

In figure 4.7 we show the mass absorption coefficient for iron at various temperatures and densities. By looking at the solid density (7.874 g/cm^3), 3 eV and 10 eV cases, we can see that the V_{eff}^{AA} and V^{MF} results are vastly different. The results of Fu et al. [104] show that the DC conductivity for iron from 10^4 K to 3x10^4 K should be around 2x10^6 S/m, and the experimental measurements of Powell give the conductivity of liquid iron at the melting point to be approximately .719x10^6 S/m [105]. Our V^{MF} results for iron at 3 eV are 5.30x10^6 S/m whereas the V_{eff}^{AA} results are .046x10^6 S/m, indicating that the V^{MF} calculations are more accurate than the V_{eff}^{AA} results in these lower temperature, solid density cases. The under-predictive behavior of the V_{eff}^{AA} results is also in line with similar results obtained for tungsten and gold by Ovechkin et al [67] at low temperatures, where it was explained as being due to not including ion correlations in their calculations, a conclusion supported by our results.

Finally we present the results of our calculation for iron at 182 eV and .4 g/cm^3 in figure 4.8. This case was chosen because it corresponds to the conditions thought to describe the experiment at Sandia's Z machine, which shows a dramatic difference with current state-of-the-art opacity calculations [12]. We do not see any significant difference between the V^{MF} and V_{eff}^{AA} calculations for this density and temperature and certainly no differences that could account for any of the discrepancies between the experiment and current high-fidelity opacity calculations. A comparison of the V_{eff}^{AA} and V^{MF} opacities at the wavelength range of the Bailey et al. experiment is shown in figure 4.9. This qualitatively corresponds to similar findings using a different model for the ion-correlations found by Krief et al. [11]. It is worth pointing out however, that the effect of multiple scattering (i.e. a multi-center calculation) is not included here, in either the average atom or potential of mean force approaches. To our knowledge, such a calculation is not possible with current techniques.

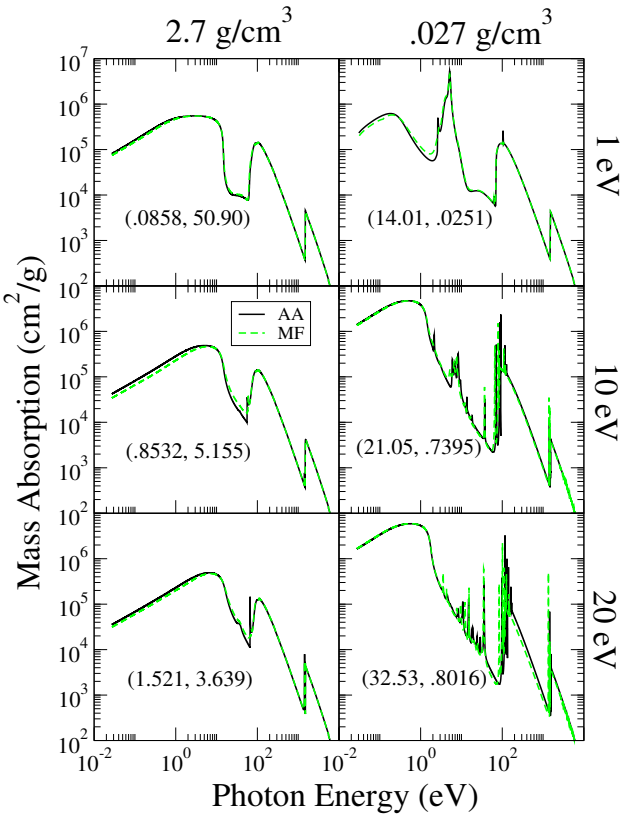

Figure 4.6: Mass absorption coefficient for various densities and temperatures of aluminum, which is the opacity divided by the mass density of the plasma. The V_{eff}^{AA} results are in black with the V^{MF} results in dashed green. The values of the electron degeneracy parameter, Θ, and the plasma coupling parameter, Γ, are shown as (Θ, Γ) for each temperature and density.

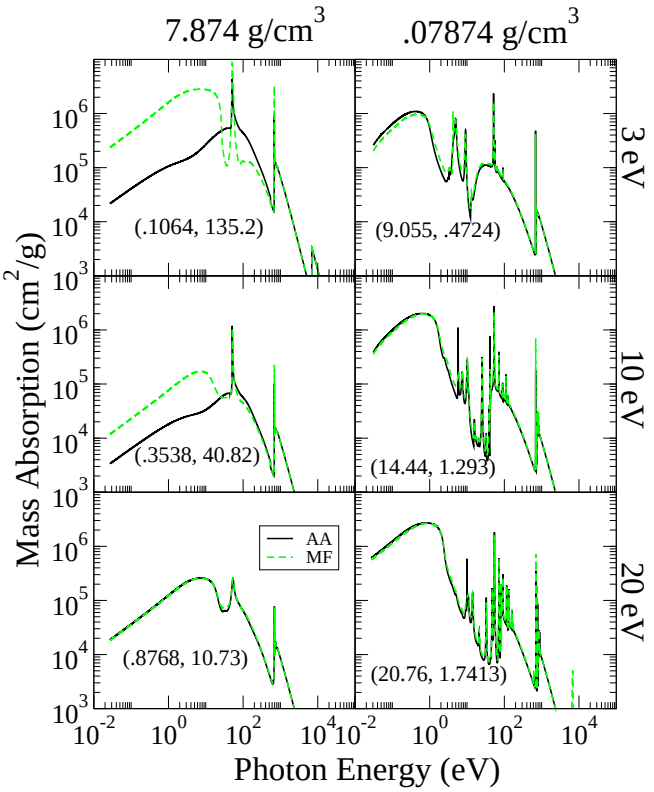

Figure 4.7: Mass absorption coefficient for various densities and temperatures of iron. The V_{eff}^{AA} results are in black with the V^{MF} results in dashed green. The values of the electron degeneracy parameter, Θ, and the plasma coupling parameter, Γ, are shown as (Θ, Γ) for each temperature and density. The low temperature, solid density results show that the average atom calculation has difficulties fully capturing the free-free opacity.

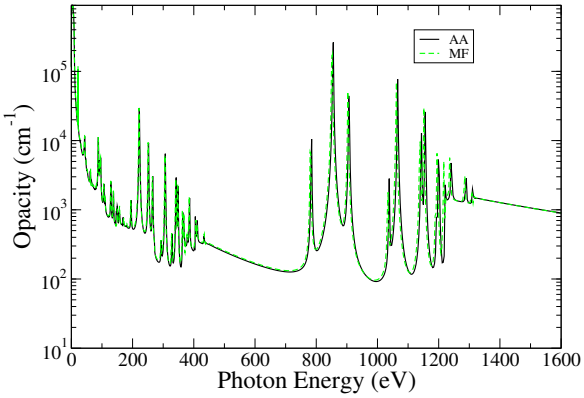

Figure 4.8: We show the calculation of the iron opacity at 182 eV and .4 g/cm^3. The differences between the V_{eff}^{AA} and V^{MF} calculations are small, and only has appreciable difference in the 400 eV to 800 eV range, though we see far less of a significant difference in this frequency range when compared to Krieff et al [11].

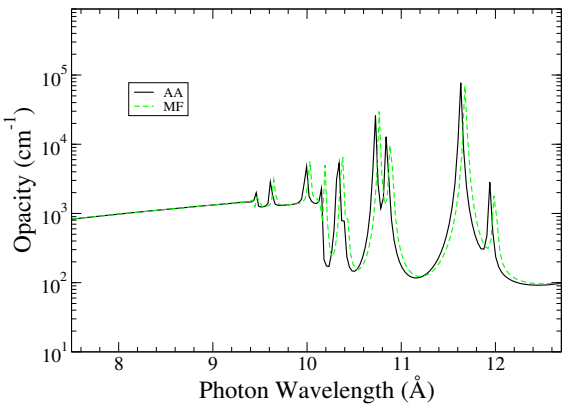

Figure 4.9: We show the calculation of the iron opacity at 182 eV and .4 g/cm^3 in the range accessible by the Bailey et al. experiment [12]. The differences we see between the two calculations are negligible compared to the discrepancies highlighted by the experiment, indicating that the effect of ion correlations does not account for the missing opacity. Since the average atom model cannot resolve individual ion stages, there is no meaning in directly comparing to the experimental data.

Though our findings qualitatively agree with Krief et al. for iron in the energy range of the Sandia experiment, they see a distinct difference in opacity between their ion sphere and ion correlation models at lower frequencies. The ion correlation model used in Reference [11] was developed by Rozsnyai [106] and involves a self-consistent calculation in which there is a significant change to the system chemical potential as compared to an average atom calculation. In contrast, our mean force calculation preserves the chemical potential and hence the state occupations of the underlying average atom calculation but uses the mean force scattering potential in the matrix elements used to determine the optical properties of the plasma. Since our calculation also preserves the ionization determined by the average atom model, it is not surprising that we see significant differences in our calculation versus that of Reference [11], especially in the free-free and bound-free transitions corresponding to the loosely bound states.

4.5 Conclusion

We have presented the calculation of plasma conductivity and opacity in the Kubo-Greenwood formalism with the effects of ion-correlations accounted for using the model developed by Starrett [9]. We see that ion-correlations can have a significant impact on the free-free transitions that dominate the DC conductivity and the opacity at low frequencies. Our V^{MF} DC conductivity calculations show improved agreement with high-fidelity DFT-MD calculations [8] of aluminum for most plasma conditions as compared to calculations using the V_{eff}^{AA} scattering potential in the Kubo-Greenwood matrix elements. The results for the AC conductivity are less clear, but V^{MF} generally shows greater agreement with DFT-MD simulations compared to V_{eff}^{AA}.

The results for the deuterium plasma show that the opacity has improved agreement with DFT-MD calculations through the use of V^{MF} over V^{AA}. The opacity in this plasma is purely due to free-free transitions. Given the improvements seen using V^{MF} to calculate the DC conductivity, which is also caused by free-free transitions, the data show that use of V^{MF} generally results in a more accurate representation of optical properties in systems where free-free transitions dominate. However, no obvious improvement is observed for bound-bound and bound-free transitions. This is likely due to the fact that the V^{MF} states are not determined

self-consistently, which would lead to shifts in the bound-bound and bound-free transition frequencies. A self-consistent determination of V^{MF} and its associated electronic structure would require a new model and is beyond the scope of this work. In Shaffer et al.'s [100] determination of the free-free opacity, two different model potentials were required to determine the opacity in deuterium and aluminum, the pseudoatom and average atom potentials, respectively. Our work shows that we can obtain reasonable results for the free-free opacity through use of V^{MF} regardless of the system under study.

For the temperatures and densities where ion correlations are significant, we see that using V^{MF} to determine the opacity has a significant impact on the free-free profile, while it has a weak effect on the bound-free and bound-bound profiles. The V^{MF} and V_{eff}^{AA} calculations are both shown to give reasonable results and satisfy the f-sum rule for the cases tested.

The relative importance of the ion-correlations is shown to depend on the plasma environment, with the effect generally becoming smaller in low density or high temperature plasmas. When assessing the relative importance of the correlations for iron at the conditions measured by Bailey et. al [12], we see no appreciable difference between the standard average atom calculation and the mean force calculation. This indicates that ion-correlations, accounted for at the level of our current model, cannot explain the discrepancy between the experimental measurements and modern opacity calculations.

Chapter 5

Ion-ion dynamic structure factor of warm dense mixtures

5.1 Abstract

The ion-ion dynamic structure factor of warm dense matter is determined using the recently developed pseudo-atom molecular dynamics method [Starrett *et al.* Phys. Rev. E 91, 013104 (2015)]. The method uses density functional theory to determine ion-ion pair interaction potentials that have no free parameters. These potentials are used in classical molecular dynamics simulations. This constitutes a computationally efficient and realistic model of dense plasmas. Comparison with recently published simulations of the ion-ion dynamic structure factor and sound speed of warm dense aluminum finds good to reasonable agreement. Using this method, we make predictions of the ion-ion dynamical structure factor and sound speed of a warm dense mixture – equimolar carbon-hydrogen. This material is commonly used as an ablator in inertial confinement fusion capsules, and our results are amenable to direct experimental measurement.

5.2 Introduction

Typically, warm dense matter refers to plasmas that have temperatures of 1-100 eV and are 1-100 times solid density. It is a state of matter that exists in the interiors of giant planets [107], in the envelopes of white dwarfs [108], and in inertial confinement fusion experiments [109]. Due to the strong electron-electron, electron-ion and ion-ion interactions, it is very challenging to model. The last few years have seen an increased interest in modeling warm dense plasma mixtures, which occur in many systems of interest in nature and the laboratory. Ab initio

simulation methods have been applied to the calculation of the equation of state and transport properties of D-T mixtures [110], LiH [111], and a variety of C-H mixtures [112, 113, 114].

The ion-ion dynamic structure factor embodies the space and time correlations of the ionic positions in the plasma. From it, one can in principle extract macroscopic information on state of the plasma, including the adiabatic sound speed and thermal diffusivity, which are essential input quantities for hydrodynamic simulations of plasmas. Predicting the ion-ion dynamic structure factor in warm dense matter has been the subject of a number of recent publications [14, 13, 115, 116]. Its measurement using free-electron lasers [117, 118] is an imminent possibility, and will represent an unparalleled test of current models.

To date, predictions of the ion-ion dynamical structure factor $S_{\alpha\beta}(k,\omega)$ from simulations of warm dense matter have been made using either density functional theory (DFT) molecular dynamics (MD) [14, 13], or with classical molecular dynamics using model ion-ion pair interaction potentials with adjustable parameters [115, 14]. The former method, DFT-MD, is the state-of-the-art approach for modeling warm dense matter but suffers from being extremely expensive; typically a calculation at a single density-temperature point requires the use of massively parallel supercomputers. This limiting factor is particularly acute for the calculation of $S_{\alpha\beta}(k,\omega)$ since its evaluation suffers from numerical noise that can only be reduced by using long simulations and thousands of particles [116]. So far, DFT-MD simulations for $S_{\alpha\beta}(k,\omega)$ in the warm dense matter regime have been limited to hundreds of particles, relatively short simulation times, and to pure aluminum plasmas. In contrast, the relatively inexpensive pair potential based classical molecular dynamics simulations [115, 14] can use thousands of particles and long simulation times. However, their predictive capability is limited by their parametric potentials that are tuned so that the results match DFT-MD calculations [14]. Moreover, such matching has been shown to be problematic [119].

Recently, it has been shown that reliable, and parameter free, ion-ion pair interaction potentials can be calculated with DFT-based approach called pseudo-atom molecular dynamics (PAMD) [43]. These pair potentials are not tuned to DFT-MD simulations, but are the result of DFT-based average atom calculations. The average atom calculations proceed rapidly, and for a given plasma density, temperature and composition, pair potentials can be quickly

generated without high-performance computing resources. These pair potentials have already been shown to give equation of state, diffusion coefficients and pair distribution functions in excellent agreement with DFT-MD simulations [28, 1, 43]. In this chapter we use PAMD to make the first predictions of $S_{\alpha\beta}(k,\omega)$ in warm dense matter based on a parameter-free pair potentials. We compare to Kohn-Sham based DFT-MD simulations for aluminum [13], finding good agreement, and to Thomas-Fermi based DFT-MD simulations finding reasonable agreement. This is a further, very stringent test of the quality of the pair potentials obtained with this method. The result shows that accurate predictions of $S_{\alpha\beta}(k,\omega)$ in warm dense matter using parameter-free pair potentials in MD simulations are possible. Due to the vastly reduced computational expense, this opens the door to wide-ranging explorations of the ionic structure of dense plasmas, including mixtures, that can both guide and be tested by experiments [118].

Here we use PAMD to show that in the hydrodynamic limit of $k \to 0$ our predictions for the dynamic structure factor for aluminum recover the known hydrodynamical form. We then make predictions for $S_{\alpha\beta}(k,\omega)$ and the adiabatic sound speed of warm dense plastic (CH), which is commonly used as an ablator material in inertial confinement fusion capsules [120]. We extract the sound speeds from each component of the dynamic structure factor and show that in the hydrodynamic limit they converge to a common value – as they should. Finally, the quasi-elastic electron-electron dynamic structure factor is calculated from $S_{\alpha\beta}(k,\omega)$. Such a quantity is in principle directly accessible in X-ray scattering experiments [117].

5.3 Methods

In pseudo-atom molecular dynamics (PAMD) the electronic density of the plasma for a given set of nuclear positions is constructed through a superposition of spherically symmetric pseudo-atom electron densities that are identical for all ions of a given species. The pseudo-atom density contains contributions from bound electrons (together with the nucleus, they form the ion) and the electrons that screen the ion [43]. The pseudo-atom electron densities are found using DFT [28, 1, 121], for which we use the Dirac exchange functional [61]. By applying the integral equations of fluid theory to the plasma [28, 121], one can determine the ion-ion pair interaction potentials. These pair potentials are uniquely determined by the pseudo-atom

electron densities; there are no adjustable parameters or assumed functional form. The nuclear positions are found with classical molecular dynamics using these pair potentials. The only inputs to PAMD are the plasma density, temperature and composition (i.e. atomic masses, nuclear charges and the number fractions of the species). Our classical MD simulations are carried out in the micro-canonical ensemble. The simulations are guided to equilibrium using velocity rescaling to achieve the target temperature; no thermostat is used during the production phase. Due to the short range nature of the pair interaction potentials for the systems considered here there is no need to use the Ewald summation technique. Specific simulation parameters are given for each calculations presented in section 5.4.

The dynamic structure factor is evaluated by first calculating the Fourier transform of the ionic number density

$$n_\alpha(\boldsymbol{k}, t) = \sum_{i=1}^{N_\alpha} \exp(\imath \boldsymbol{k} \cdot \boldsymbol{r}_i(t))$$

where there are N_α ions of species α in the simulation with positions $\boldsymbol{r}_i(t)$ at time t. The intermediate scattering function is then constructed

$$F_{\alpha\beta}(k, t) = \frac{1}{\sqrt{N_\alpha N_\beta}} \langle n_\alpha(\boldsymbol{k}, t) n_\beta(-\boldsymbol{k}, t) \rangle$$

where the angular brackets imply an average of directions as well as the ensemble average. Finally, the dynamic structure factors are the time Fourier transforms of $F_{\alpha\beta}(k, t)$

$$S_{\alpha\beta}(k, \omega) = \frac{1}{2\pi} \int_{-\infty}^{\infty} dt \exp(\imath\omega t) F_{\alpha\beta}(k, t)$$

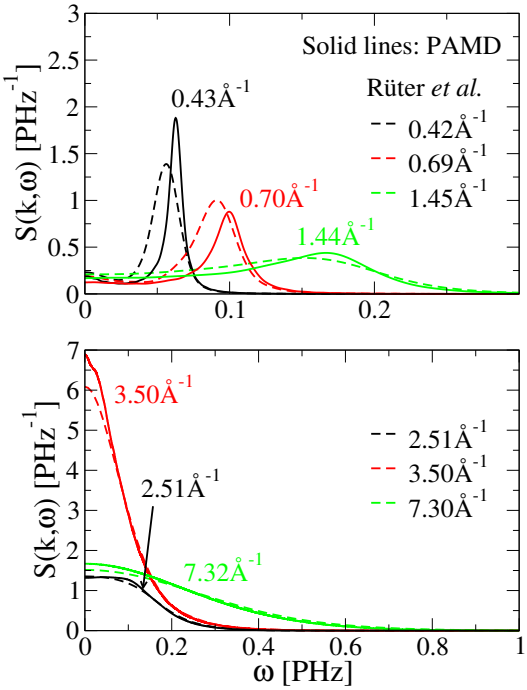

Figure 5.1: $S(k, \omega)$ for aluminum at 5.2 g/cm^3 and 3.5 eV. Solid lines are PAMD calculations and the numbers beside each curve indicate the k-value. The dashed lines are from QMD simulations [13] and the legend indicates their k-values. Despite the very different simulation methods involved, the agreement is good. The differences result from a combination of physical approximations and computational limitations (see text).

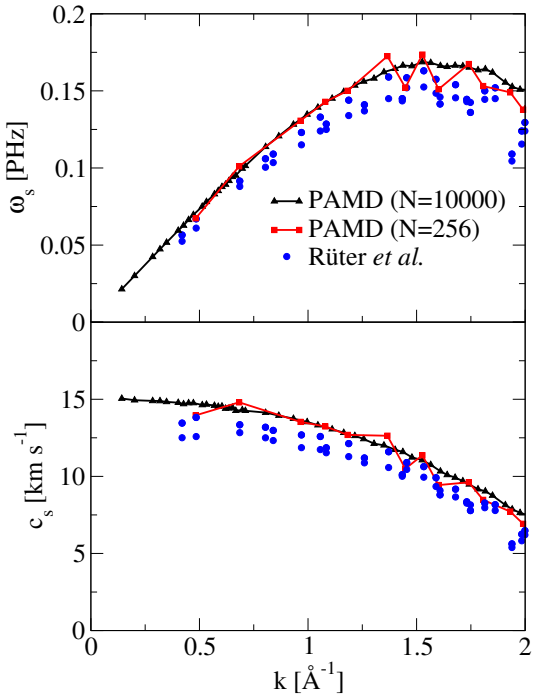

Figure 5.2: Dispersion relation ω_s (top panel) and adiabatic sound speed $c_s = \omega_s/k$ (bottom panel) for aluminum at 5.2 g/cm^3 and 3.5 eV. Solid lines with triangles are PAMD calculations using 10,000 particles. The blue dots are QMD results from [13], where 256 particles were used. For comparison, we also plot the results of a PAMD simulation using 256 particles (solid lines with squares).

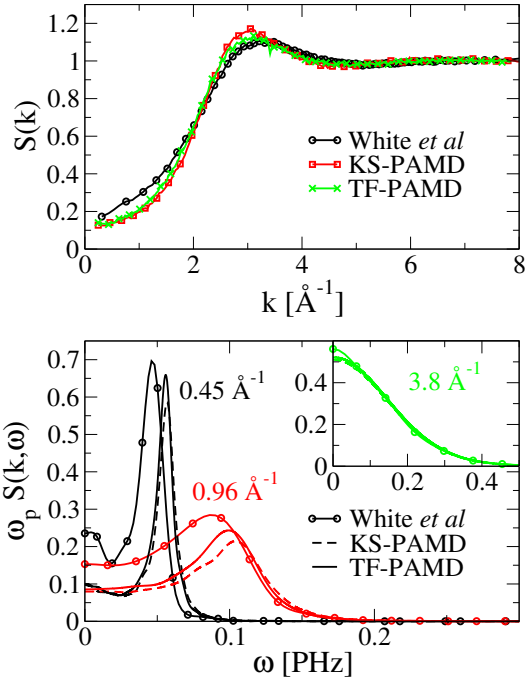

Figure 5.3: Static structure factor (top panel) and $S(k,\omega)$ (bottom panel) for aluminum at 2.7 g/cm^3 and 5 eV compared to TF-DFT-MD simulations [14]. We show PAMD results using both Thomas-Fermi (TF) and Kohn-Sham (KS) functionals. ω_p is the ion plasma frequency. For KS-PAMD $\hbar\omega_p$ = 0.123 eV, for TF-PAMD $\hbar\omega_p$ = 0.125 eV.

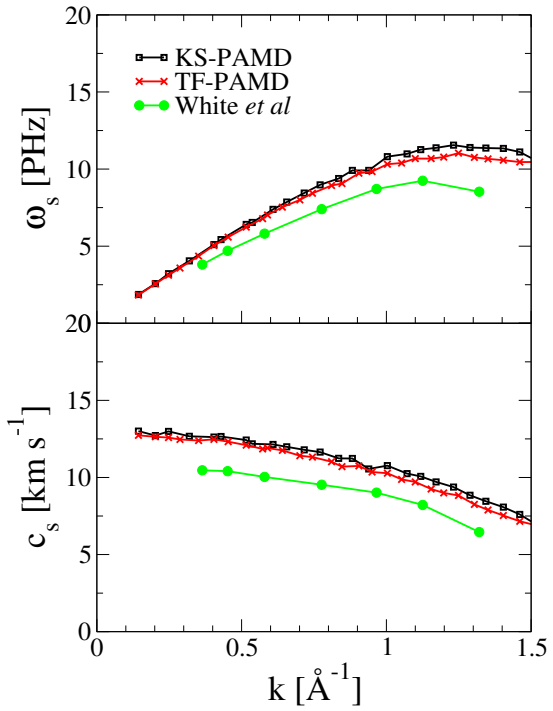

Figure 5.4: Dispersion relation ω_s (top panel) and adiabatic sound speed $c_s = \omega_s/k$ (bottom panel) for aluminum at 2.7 g/cm^3 and 5 eV. We show PAMD results using both Thomas-Fermi (TF) and Kohn-Sham (KS) functionals.

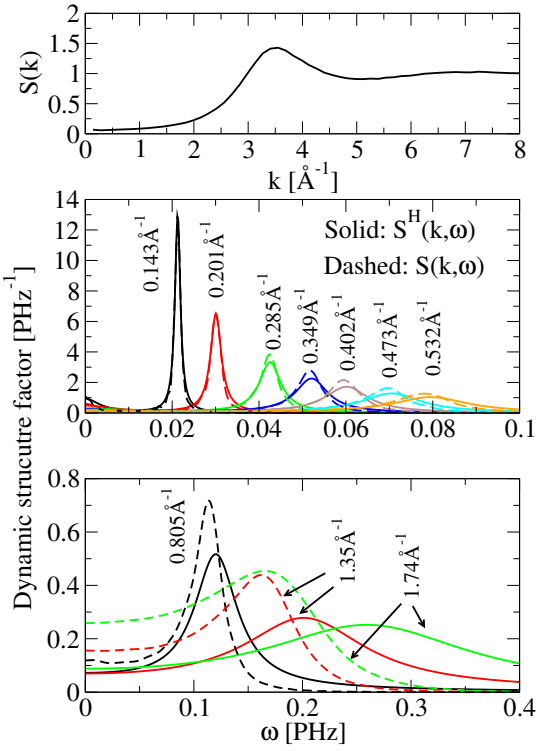

Figure 5.5: Static structure factor (top panel) for aluminum at 5.2 g/cm^3 and 3.5 eV. The bottom two panels show the calculated dynamical structure factor and the hydrodynamical fit (equation (5.1)). The four fit parameters are determined by a least squares fit of the calculated data for $k = 0.143$ Å^{-1}. On increasing k (values are marked beside the corresponding lines) this hydrodynamical fit begins to deviate from the calculated curves, as is expected.

5.4 Results

5.4.1 Aluminum plasmas

In figure 5.1 we compare PAMD calculations of $S_{\alpha\beta}(k,\omega)$ to QMD[1] results [13] for an aluminum plasma at 3.5 eV and 5.2 g/cm^3. For the smallest k-vectors[2] both calculations predict a strong ion acoustic (Brillouin) peak, and a small central diffusive (Rayleigh) peak. This is also where the quantitative agreement of the two approaches is at its worst. Increasing k to values corresponding to the first peak in the static structure factor (see figure 5.5), and beyond, the agreement improves and both methods recover the free particle limit (a Gaussian) at the largest k value.

In figure 5.2 we show the dispersion relation $\omega_s(k)$ of the ion acoustic peak for the same aluminum plasma compared to the QMD results of [13], and the corresponding sound speed $c_s = \omega_s/k$. The scatter in the QMD data is partly a result of suppression of long time oscillations in $F(k,t)$ using a Gaussian window function [13] with two different choices of the decay time scale. These long time oscillations must also be damped in the PAMD simulations; we apply the method described in [122]. The combination of this method as well as long and large PAMD simulations result in very little numerical noise in ω_s and c_s. The PAMD simulations predict a slightly larger sound speed (15.0 km s^{-1}) than the QMD simulations (12.5–14 km s^{-1}), but the overall agreement is good.

The differences in the predicted $S(k,\omega)$ from the two methods (PAMD and QMD) are likely to be caused by a combination of numerical limitations and physical approximations. The well-converged PAMD simulations used 10,000 particles for a total simulation time of 0.36 ns [3]. In contrast, the QMD simulations of [13] used 256 particles for a total simulation time of 3.08 ps. Due to the expensive nature of the QMD simulations convergence tests using a larger number of particles and longer simulations are impractical. We verified that PAMD simulations using 256 particles and 3.08 ps do not significantly change the resulting sound

[1] QMD – Quantum Molecular Dynamics, refers to Kohn-Sham DFT-MD simulations.

[2] The use of periodic boundary conditions in both QMD and PAMD restricts the k values that are accessible to each simulation, hence the slight differences in the k values in figure 5.1.

[3] We used a cubic simulation cell with a time step of 0.95 fs.

speed, although it becomes much noisier (figure 5.2). However, QMD and PAMD should have different size effects due to the different methods involved. A modest reduction of $\sim 2.5\%$ in the PAMD c_s was found when the Dirac exchange potential was replaced by a finite temperature exchange and correlation potential in the local density approximation [79]. One the other hand the QMD simulations [13] used a generalized gradient approximation [123]. Other physical approximations that may affect the results include the superposition approximation in PAMD, and the use of a pseudopotential in the QMD simulations [13]. We note that PAMD does not use a pseudopotential; bound states are treated in the same way as the continuum states. In summary the agreement between the methods is good, given the very different approaches used.

In figure 5.3 we show the static structure factor and $S(k,\omega)$ for an aluminum plasma at 2.7 g/cm^3 and 5 eV. Both Thomas-Fermi (TF) and Kohn-Sham (KS) PAMD results are shown and compared the DFT-MD simulations of White et al. [14]. The simulations of White et al. used the Thomas-Fermi functional and a pseudopotential derived by inverting the Kohn-Sham equations for bulk aluminum [124]. This effectively corrects the poor behavior of TF-DFT-MD at low temperatures by recovering the proper limit, and makes the TF-DFT-MD behave like KS-DFT-MD at low temperature. The KS and TF-PAMD results are similar, and there is reasonable agreement with the TF-DFT-MD results of White et al. However, the agreement is worse than for the KS-DFT aluminum plasma shown in figure 5.1. In particular, PAMD gives a smaller value for $S(k,\omega=0)$ than the results of White et al and higher frequencies for the acoustic peak at small k values. The corresponding sound speeds and dispersion relations for are shown in figure 5.4. TF-PAMD predicts an adiabatic sound speed of 12.7 km/s compared to 10.4 km/s from TF-DFT-MD. Our PAMD simulations used 5000 particles in a cubic simulation cell with a time step of 0.84 fs for a total simulation time of 1.34 ns. In contrast the TF-DFT-MD result used 864 particles with a time step of 0.25 fs for a simulation time of 1.5 ps. The most likely source of the differences observed in figure 5.3 is either the superposition approximation in PAMD or the pseudopotential in TF-DFT-MD.

In summary, the comparison of PAMD to KS- and OF-DFT-MD simulations of $S_{\alpha\beta}(k,\omega)$ and the corresponding sound speed reveals good to reasonable agreement. The differences are

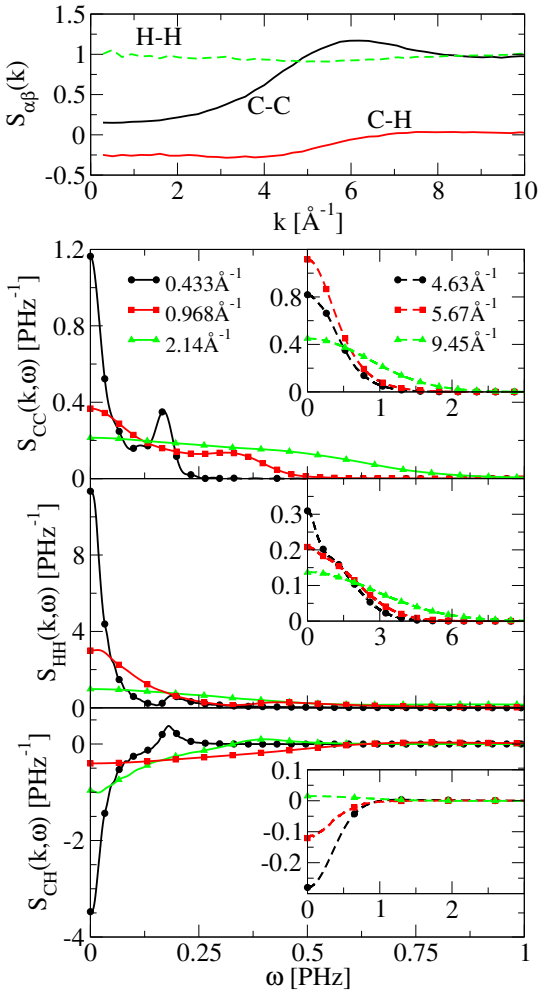

Figure 5.6: Static structure factor from PAMD (top panel) for a carbon-hydrogen mixture at 10 g/cm^3 and 10 eV. The bottom three panels show the dynamic structure factors for C-C, H-H and C-H at various fixed values of k.

most likely due to physical approximations: the superposition approximation in PAMD, the pseudopotentials in KS- and OF-DFT MD, and the difference choices of exchange and correlations potentials. Numerical limitations of the much more expensive DFT-MD methods may play a part. The dynamic structure factor $S_{\alpha\beta}(k,\omega)$ is a very sensitive test of the forces on the ions. That a parameter-free pair potential method (i.e. PAMD) attains the level of agreement seen with the DFT-MD methods is quite remarkable, and supports the underlying assumptions of PAMD. These comparisons also give us confidence that predictions of $S_{\alpha\beta}(k,\omega)$ with PAMD are reasonably accurate and that PAMD can be used as a relatively inexpensive tool for investigating $S_{\alpha\beta}(k,\omega)$ in warm dense matter.

In figure 5.5 we show $S(k,\omega)$ for an aluminum plasma at 3.5 eV and 5.2 g/cm^3 at small k values. For the smallest k value available from the simulation ($k = 0.143$Å^{-1}) we use a least squares fit to the hydrodynamical form of the dynamic structure factor [125]:

$$\begin{aligned} S^H(k,\omega) &= \frac{S(k)}{2\pi}\left[\left(\frac{\gamma-1}{\gamma}\right)\frac{2D_T k^2}{\omega^2+(D_T k^2)^2}\right. \\ &\left.+\frac{1}{\gamma}\left(\frac{\Gamma k^2}{(\omega+c_s\,k)^2+(\Gamma\,k^2)^2}+\frac{\Gamma k^2}{(\omega-c_s\,k)^2+(\Gamma\,k^2)^2}\right)\right] \end{aligned} \tag{5.1}$$

The four parameters of this fit are $\gamma = c_P/c_V$, the ratio of specific heats, D_T, the thermal diffusivity, Γ, the sound attenuation coefficient which is related to the kinematic viscosity [125] and c_s, the adiabatic sound speed. In principle, fitting the form (5.1) to the small-k $S_{\alpha\beta}(k,\omega)$ provides all four material properties. For reference the values of the four fit parameters found for this case are (in atomic units) γ = 1.18, D_T = 1.68$\times$ 10^{-2}, Γ = 3.21$\times$ 10^{-3} and c_s = 6.84$\times$10^{-3}. The agreement between the PAMD $S(k,\omega)$ and the fit is very good. Keeping these parameters fixed, but increasing k we can see that the hydrodynamical fit starts to deviate from the calculated curves, with noticeable differences for $k \gtrsim 0.3$Å^{-1}.

5.4.2 Carbon-hydrogen Plasma

We now turn to $S_{\alpha\beta}(k,\omega)$ for a carbon-hydrogen mixture relevant to inertial confinement fusion experiments [113]. Figure 5.6 shows the PAMD $S_{CC}(k,\omega)$, $S_{HH}(k,\omega)$ and $S_{CH}(k,\omega)$ for an equimolar carbon - hydrogen mixture at 10 eV and 10 g/cm^3. Bonds can occur in CH

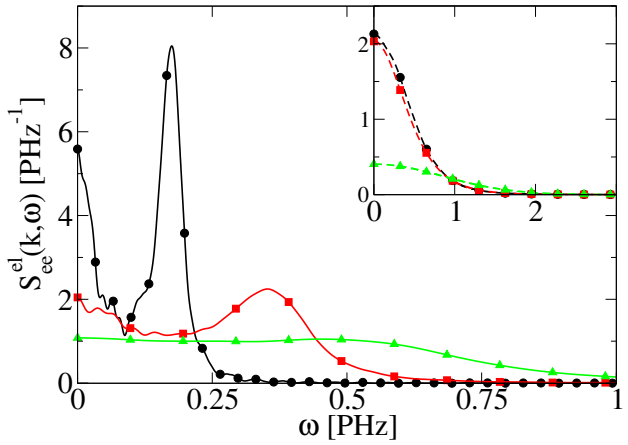

Figure 5.7: Elastic part of the electron-electron dynamic structure factor for CH at 10 eV and 10 g/cm^3. The k-values and line labels in this figure and inset are the same as in figure 5.6.

plasmas at lower temperature and density [113]. We have previously shown that the ion-ion pair interaction potentials used in PAMD result in static structure predictions that agree well with QMD calculations under similar conditions for a carbon-hydrogen mixture [121], consistent with the complete breakup of bonds found in [113]. The PAMD simulations here used a total of 8,000 particles and a total simulation time of 0.12ns in a cubic simulation box with time step of 0.068 fs. The partial structure factors $S_{\alpha\beta}(k)$ for the CH plasma (figure 5.6, top panel) shows that the hydrogen ions are uncorrelated, the carbon ions are moderately coupled, and that there is no sign of incipient bonding in the system. The partial dynamical structure factors $S_{\alpha\beta}(k,\omega)$ reveal significantly different behavior of the carbon and hydrogen ions. The H-H diffusive peak is $\sim$10 times larger than that of C-C, owing to the much lower mass and charge (i.e. coupling) of the hydrogen. For the same reason the acoustic peak of $S_{HH}(k,\omega)$ is always at a higher frequency than for $S_{CC}(k,\omega)$.

X-ray scattering experiments measure the double-differential cross section which is proportional to the total electron structure factor [126]. For small ω the dominant contribution to this is from quasi-elastic scattering by the bound and screening electrons. This is related to the ion-ion dynamic structure factors by [126, 127, 128, 121]

$$S_{ee}^{el}(k,\omega) = \sum_{\alpha,\beta} \sqrt{x_\alpha x_\beta} n_{\alpha,e}^{PA}(k) n_{\beta,e}^{PA}(k) S_{\alpha\beta}(k,\omega) \tag{5.2}$$

where the sums are over species index, x_α is the number fraction of species α and $n_{\alpha,e}^{PA}(k)$ is the Fourier transform of the pseudo-atom electron density for species α [121, 128]. The result for the carbon-hydrogen mixture is shown in figure 5.7. Unlike the pure aluminum cases, the central diffusive (Rayleigh) peak is comparable in magnitude to the acoustic peak at small k. This is due in roughly equal parts to the larger value of $S(k)$ for CH compared to that for Al (see equation (5.1)), and a larger value of the ratio of specific heats γ.

The dispersion relations and corresponding sound speeds extracted from $S_{CC}(k,\omega)$ and $S_{HH}(k,\omega)$ are shown in figure 5.8. As $k \to 0$ these sound speeds converge to a common value, as they should in the hydrodynamic limit. Even with these large simulations, at the smallest k value available the two sound speeds still differ by $\sim 8\%$; their average value predicting a sound

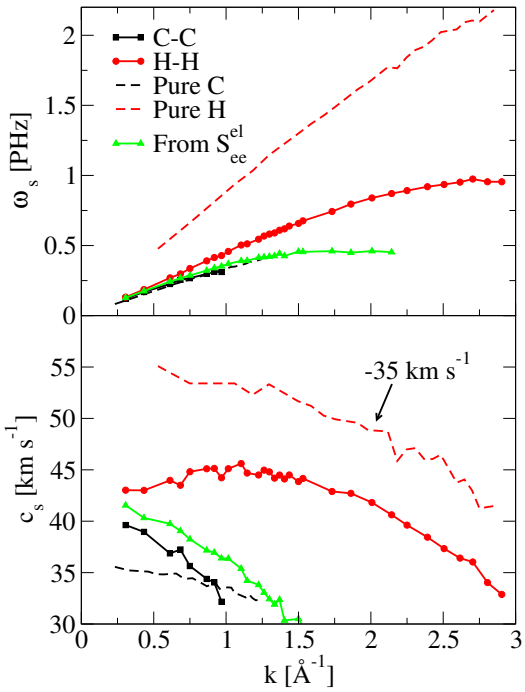

Figure 5.8: Top panel shows the dispersion relations extracted from the PAMD dynamic structure factors $S_{CC}(k,\omega)$, $S_{HH}(k,\omega)$ and $S_{ee}^{el}(k,\omega)$ as well as the dispersion relations for a pure hydrogen and a pure carbon plasma at the same temperature and density as the mixture (10 eV and 10 g/cm^3). In the bottom panel the corresponding adiabatic sound speeds ($c_s = \omega_s/k$) are shown. For clarity, the sound speed for the pure hydrogen case has been shifted by -35 km s^{-1}.

speed of 41.3 km s^{-1}. For comparison, we also show the dispersion relations and sound speeds for pure hydrogen and pure carbon plasmas at the same density and temperature as the mixture. Also shown in figure 5.8 is the dispersion relation and sound speed extracted from $S_{ee}^{el}(k,\omega)$. Qualitatively this follows the carbon-carbon result but is shifted to larger sound speeds.

As k increases from the hydrodynamic limit the sound speeds for hydrogen and carbon split into fast (H) and slow (C) sounds, with hydrogen showing a slight positive dispersion (figure 5.8). This phenomenon, known as "fast sound", was first predicted in molecular dynamics simulations of liquids [129] and later observed in neutron scattering experiments on a cryogenic He-Ne mixture [130] and in a low-density, hot Be-Au plasma [131]. To our knowledge, this is the first time the fast sound phenomenon has been predicted in the warm dense matter regime. This effect arises as a consequence of transitioning from the hydrodynamic to kinetic regimes [132], where the behavior of particles of each species is less collective and reflects more their different masses and interaction potentials.

5.5 Conclusions

In conclusion, we have demonstrated that the recently developed pseudo-atom molecular dynamics simulation method for warm dense matter can be used to investigate the ion-ion dynamic structure factor, giving results that agree well with the much more computationally expensive KS-DFT-MD methods. A comparison with TF-DFT-MD simulations also gave reasonable agreement. These comparisons give us confidence that PAMD can be used as reasonably accurate and relatively inexpensive tool to investigate the properties of $S_{\alpha\beta}(k,\omega)$ in warm dense matter. In the hydrodynamic limit, the known form of the ion-ion dynamic structure factor is recovered by PAMD simulations for an aluminum plasma. We have used PAMD to make predictions of the ion-ion dynamic structure factor and the adiabatic sound speed of a warm dense mixture of carbon and hydrogen. From these we have calculated the quasi-elastic part of the electron-electron dynamic structure factor, a quantity that is measurable in X-ray scattering experiments.

Chapter 6

Linear Response Time-Dependent Density Functional Theory Applied to Absorption Cross-sections

As the previous chapters of this work have demonstrated, density functional theory provides a strong formalism for describing multi-electron systems using the simpler, single-particle Kohn-Sham framework as opposed to the oft intractable full solution of the many-particle Schrodinger equation. The work in this chapter describes the time-dependent density functional theory (TD-DFT) in its linear response formulation and our use of the TD-DFT techniques to evolve the ground state electron density obtained by Tartarus. Specifically for this chapter, the TD-DFT framework provides a rigorous extension of DFT to the study of time-dependent photo-excitation events within the Tartarus average atom model.

The work detailed in Chapter 4 showed the independent particle response of electrons exposed to an incident photon. The independent particle response is marked by describing an electron's transition from one state in its unperturbed system to another state in the same unperturbed system. Clearly this picture does not capture all of the physics of an absorption, as the electrons in a system should exhibit a correlated motion in response to any perturbation. TD-DFT allows us to study the way that the entire multi-electron system responds to a perturbation, which formally would include transitions of the ground state to all possible excited states. With the entire correlated response accounted for by a time-dependent approach, we can obtain dynamic results that often show significant differences from the independent particle results. Not only does this allow us to better describe the photo-excitation process in our system, it also helps us to understand in what frequency regimes the electrons exhibit the

most exchange-correlation (xc) effects (i.e. where the independent particle description is least reliable is where the electrons of the system are most strongly correlated).

Before giving an overview of the linear response TD-DFT formalism applied in this chapter, it is useful to broadly give the history of this topic. After the initial KS-DFT formalism was firmly grounded by theoretical proofs and results demonstrating good agreement with experiments, the application of DFT became widespread and applied to a vast number of many-electron systems in their ground state. It is no surprise that there was also interest in utilizing DFT for the study of dynamic systems, and the first attempts at this were done by Ando [133], Peuckert [134], and Zangwill and Soven [135]. These works involved mapping the response of the electron density in a time-dependent potential into a system of independent particles each responding to an effective time-depenent potential (which was in general different from the actual perturbing potential). Ando's work involved specifically studying the line-shapes of transitions within the surface of a silicon system. Peuckert provided a detailed formalism with explicit time-dependence and applied this to a test-study of helium. Zangwill and Soven's work recast the formalism into a frequency-space representation involving a self-consistent determination of the effective time-dependent potential. Their work had considerable impact as the frequency-space formalism they presented was more readily applicable to a variety of systems of interest than the explicit time approaches (mainly due to the relative simplicity of the frequency response approach, in terms of both computational implementation and theoretical formulation). Zangwill and Soven demonstrated excellent agreement with experimental results for neutral, rare gases, when in the past independent particle calculations showed signficant discrepancy with the experiments. Each of these foundational studies was carried out with sound physical intuition, but no formal theorem analogous to the Hohenberg-Kohn or Kohn-Sham theorems existed.

With such promising results from these initial studies, there became a need for a formal continuation of the theorem of DFT into the time-dependent regime. For the interested reader, a brief overview of the foundational DFT model and some approapriate references are given in

Chapter 1.2.1 of this work. To restate this problem, the need was to have a theorem which described a one-to-one correspondence between an external time-dependent potential and a time-dependent electron density (in analogy to the first Hohenberg-Kohn theorem). Further, there was need to show that these time-dependent densities could be recast into a system of independent quasi-electrons in single-particle time-dependent states of an effective time-dependent potential (in direct analogy to the Kohn-Sham DFT formalism). The first attempts at formalizing TD-DFT in these ways came from using specific forms of time-dependent potentials from Deb and Ghosh [136] and Bartolotti [137, 138]. Deb and Ghosh formed a rigorous description of TD-DFT using periodic potentials, whereas Bartolotti did the same for potentials describing adiabatic processes. The general formulation for TD-DFT was completed by Runge and Gross in 1984 [139]. Further refinements of the theory to apply for all causal time-dependent external potentials (i.e. all physical potentials) were added by van Leeuwen in 1999 [140]. There were many other contributions towards the rigorous demonstration of TD-DFT's validity for a variety of mathematically complex situations. We direct the interested reader to the review article by Marques and Gross (reference [141]) for more details on the refinement of the proofs of the TD-DFT theorems.

Modern efforts in TD-DFT have spread into diverse fields of study, with real-time TD-DFT methods studying non-perturbative laser interactions with matter, the use of time-dependent calculations to inform the static ground state exchange-correlation functionals, and the study of large systems such as solids [142]. Some studies of solids require a formalism extended even beyond TD-DFT to time-dependent current-density functional theory, originally developed by Vignale and Kohn [143]. Even with the many various applications and adaptation of TD-DFT in use today, the vast majority of applications for TD-DFT are in spectroscopic fields. This includes photoabsorption spectra and the study of excitation energies normally unaccessable by ground state DFT calculations. Most of these applications can be studied with the frequency-space representation of TD-DFT (largely unchanged from its first implementation by Zangwill and Soven) and the modest size of the systems means that knowledge of the ground state XC potential is sufficient for most purposes (the so-called adiabatic local density approximation) [142].

This chapter will describe our intial efforts in developing a TD-DFT code for use with the Tartarus ground state electron density. We will begin with a broad overview of the theoretical description of the TD-DFT formalism, with focus on the linear response approximation and the frequency-space application to photon perturbations. In order to show that we are able to achieve reasonable results with our code, we compare to previously published data, including experimental and theoretical results. First we compare to the foundational results for neutral rare gases, originally studied by Zangwill and Soven. Next we compare to results for finite-temperature systems. Finally we provide a brief conclusion that includes our thoughts on future work using TD-DFT.

6.1 Theoretical Overview of Linear Response TD-DFT

Our main interest in this work is to study the evolution of a many-electron system exposed to an exciting photon. These photons can be considered weak electric fields oscillating at the photon frequency. The weak electric field of a photon allows us to treat the photon's interaction with the system as a perturbation, and the total induced dipole moment from the perturbation can be used to obtain the absorption cross-section. For many purposes, knowing the linear response (i.e. the response of the system that has the same characteristic frequency as the perturbation) of the system is sufficient. Fortunately for our purposes, we can obtain exact expressions for the linear response of a system whose ground state density is described by Kohn-Sham orbitals. This section will give a broad overview of the linear response description of the TD-DFT formalism, and we follow standard prescriptions that show up in many other sources (e.g. references [142], [141]).

6.1.1 Linear Density Response

We consider a system at rest in its ground state. At $t = 0$ some time-dependent perturbation occurs which illicits a time-dependent response in the electron density. Under this description the external potential (i.e. the potential due to nuclei and photons) can be represented as the sum of the static external potential and the time-dependent perturbation:

$$V_{ext}(\vec{r},t) = V_{ext,0}(\vec{r}) + \delta V_{ext}(\vec{r},t) \tag{6.1}$$

where $V_{ext,0}$ is the external potential associated with the ground state system and δV_{ext} is the time-dependent potential associated with the perturbation to the ground state. Since the central tenet of TD-DFT is that the external potential fully defines the time-dependent electron density (and vice versa), we can represent the time-dependent density as a Taylor series:

$$n(\vec{r},t) = n_0(\vec{r}) + \delta n_1(\vec{r},t) + \delta n_2(\vec{r},t) + \cdots \tag{6.2}$$

where the linear response is defined by truncating the expansion after the second term, δn_1. Following from standard response theory and in accordance with the one-to-one correspondence of the external potential to the time-dependent density, we can write the density response as

$$\delta n_1(\vec{r},t) = \int_0^\infty dt' \int d\vec{r'} \chi(\vec{r},\vec{r'},t,t') \delta V_{ext}(\vec{r'},t') \tag{6.3}$$

where χ is a susceptibility function equivalently defined, as in typical response theory, as the change in the density with respect to the external potential:

$$\chi(\vec{r},\vec{r'},t,t') = \left. \frac{\delta n(\vec{r},t)}{\delta V_{ext}(\vec{r'},t')} \right|_{V_{ext}=V_{ext}(\vec{r'},0)} \tag{6.4}$$

and where the δ notation in equation 6.4 is used to denote the functional derivative of the electron density with respect to the total external potential. This susceptibility function, using perturbation theory, can also be written in terms of the ground state multi-electron wavefunction (i.e. Ψ_0), the multi-electron wavefunctions associated with all possible excited states of the system (i.e. Ψ_i), and the frequency ω associated with the linear response obtained after Fourier transforming with respect to time (specifically with respect to the difference in time between

events, $t - t'$):

$$\chi(\vec{r}, \vec{r'}, \omega) = \sum_i \left[\frac{\langle \Psi_0 | \hat{n}(\vec{r}) | \Psi_i \rangle \langle \Psi_i | \hat{n}(\vec{r'}) | \Psi_0 \rangle}{\omega + E_0 - E_i + i\delta} - \frac{\langle \Psi_0 | \hat{n}(\vec{r'}) | \Psi_i \rangle \langle \Psi_i | \hat{n}(\vec{r}) | \Psi_0 \rangle}{\omega + E_i - E_0 + i\delta} \right] \tag{6.5}$$

where the sum runs over all excited many-body states (ostensibly an infinite number of states), $\hat{n} = \sum_{j=1}^{N} \delta(\vec{r} - \vec{r}_j)$ is the density operator with the sum running over all electrons in the system and δ being the Dirac delta function, ω is the frequency of the perturbing photon (or more generally, the principal frequency associated with the perturbing potential), δ is a positive infinitessimal, and E is the energy associated with the many-body states, Ψ [135, 142].

6.1.2 Time-Dependent Kohn-Sham Equation

Up until now in this chapter, we have presented the exact formulation of the density response to a perturbation, but these obviously assume complete knowledge of the many-body ground and excited states as full-solutions to the Schrodinger or Dirac equations. The exact many-body wavefunctions for the ground state and excited states are all but impossible to obtain for most systems. Just as DFT circumvents the need for these wavefunctions by recasting the many-body system into an effective non-interacting particle system, we can do the same for the time-dependent system. The so-called time-dependent Kohn-Sham (TDKS) equation can be written as

$$i\frac{\partial \psi_j(\vec{r}, t)}{\partial t} = \left[\frac{-\nabla^2}{2} + V_{KS}[n(\vec{r}, t); n_0(\vec{r})](\vec{r}, t) \right] \psi_j(\vec{r}, t) \tag{6.6}$$

where ψ_j are the non-interacting KS electron states, and V_{KS} is the effective one-body potential (which is a functional of both the density at time t and the ground state density, n_0), defined as

$$V_{KS}[n(\vec{r}, t); n_0(\vec{r})](\vec{r}, t) = V_{ext}[n(\vec{r}; t); n_0(\vec{r})] + \int d\vec{r'} \frac{n(\vec{r'}, t)}{|\vec{r} - \vec{r'}|} + V_{xc}[n(\vec{r}, t); n_0(\vec{r})](\vec{r}, t) \tag{6.7}$$

where V_{ext} is the external potential, the second term is the classical Hartree potential associated with repulsion between the electrons, and V_{xc} is the Kohn-Sham potential that contains all of the exchange-correlation information not contained within the other two terms. Just as in ground

state DFT, V_{xc} must generally be approximated for realistic systems. It is worth reiterating a major point of TD-DFT here: the potential V_{ext} is a functional of the present density ($n(\vec{r},t)$) and the ground state density ($n_0(\vec{r})$) because there is a one-to-one correspondence between the external potential and the electron density according to the Runge-Gross theorem [139]. The final expression needed to complete the TDKS equations is the correspondence between the KS states and the time-dependent electron density:

$$n(\vec{r},t) = \sum_{j=1}^{N} f_j \left| \psi_j(\vec{r},t) \right|^2 \tag{6.8}$$

where f_j are the occupations of the j-th state. Equations 6.6, 6.7, and 6.8 together represent the recasting of an interacting N electron system into a system of N non-interacting quasiparticles in an effective time-dependent potential, and together the three equations can be solved self-consistently along with a time-propagation to solve for the time-dependent density.

It should be stated here that the density obtained by equation 6.8 is the true many-body electron density if the exact form of V_{xc} is known. This is of course analogous to ground state DFT, where decades of work has been carried out to find accurate exchange-correlation functionals. Likewise, in most cases it is a lack of knowledge of $V_{xc}(\vec{r},t)$ that limits the usefulness of TD-DFT methods.

6.1.3 TDKS Linear Response

With the basics of linear response and the TDKS formalisms detailed in the previous two subsections, we have the theoretical basis needed to fully describe the frequency-space linear response calculations as developed by Zangwill and Soven [135]. The linear response description detailed in 6.1.1 is presented with explicit time-dependence for ease of understanding, and the TDKS equations in 6.1.2 likewise are represented with explicit time-dependence. Though the TDKS expressions can be solved with explicit time-dependent methods (and in some applications this is done), the linear response formalism lends itself to often be easily solved with a frequency-dependent method. As we can see from equations 6.5 and 6.3, for small perturbations there is a relatively straightforward means of determing the induced density if one knows

all of the many-body wavefunctions for the ground and excited states. Since this is impractical, we can combine the TDKS procedures with the linear response formalism to recast the solution of the induced density in terms of a non-interacting system.

Combining the procedures in 6.1.1 and 6.1.2, we can see that the exact linear density response can be written as

$$\delta n_1(\vec{r},t) = \int_0^\infty dt' \int d\vec{r}\chi_0(\vec{r},\vec{r'},t,t')\delta V_{KS}(\vec{r'},t') \tag{6.9}$$

where $\delta V_{KS} = V_{KS} - V_0^{ext}$ and with

$$\chi_0(\vec{r},\vec{r'},t,t') = \left.\frac{\delta n(\vec{r},t)}{\delta V_{KS}(\vec{r'},t')}\right|_{V_{KS}=V_{KS}(\vec{r'},0)} \tag{6.10}$$

Since χ_0 is associated with non-interacting Kohn-Sham systems, when expressed analogously to equation 6.5, we obtain a simplified expression in terms of non-interacting KS states associated with the ground state:

$$\chi_0(\vec{r},\vec{r'},\omega) = \sum_{i,j}(f_i - f_j)\frac{\psi_i^*(\vec{r})\psi_j(\vec{r})\psi_i(\vec{r'})\psi_j^*(\vec{r'})}{\omega - (E_j - E_i) + i\delta} \tag{6.11}$$

where the sums over i and j run over all possible states. This non-interacting susceptibility exactly describes the linear response of the system to the external potential if the KS induced potential (δV_{KS}) is known—that is to say, equations 6.3 and 6.9 are formally equivalent and are exact within the regime of small perturbations. Clearly the issue to obtaining the exact linear density response is obtaining the appropriate induced KS potential. How this is done as well as how the induced density is used to access observable quantities is the focus of the next section.

6.2 Induced Linear Response

6.2.1 Induced Density

As we know from the Runge-Gross theorem [139], all time-dependent observables can be obtained from the time-dependent density, and therefore our main goal for this work is to obtain

the induced density and thus the time-dependent density within the linear response approximation. This is a task that can be efficiently accomplished by using the frequency-space representation of the induced quantities. We note here that within the linear response approximation, all induced quantities only have dependence on the frequency of the perturbation, and this greatly simplifies the algorithm when implementing this solution.

Here we present the relevant expressions in their frequency-dependent representation. The concepts behind their derivation are no different from what was described in the previous sections, and to obtain these expressions a Fourier transform with respect to time is taken. We also note that since we are only concerned with the linear response, we drop the first-order subscript on the induced density (i.e. $\delta n_1 = \delta n$ for the remainder of this work).

$$\delta V_{KS}(\vec{r},\omega) = \delta V_{ext}(\vec{r},\omega) + \int d\vec{r'} \frac{\delta n(\vec{r'},\omega)}{|\vec{r}-\vec{r'}|} + \delta V_{xc}(\vec{r},\omega) \tag{6.12}$$

$$\delta n(\vec{r},\omega) = \int d\vec{r'} \chi_0(\vec{r},\vec{r'},\omega)\delta V_{xc}(\vec{r'},\omega) \tag{6.13}$$

where $\delta V_{xc} = V_{xc} - V_{xc,0}$ with $V_{xc,0}$ being the ground state exchange-correlation (xc) potential. There is obviously significant choice in how one represents δV_{xc}, but the most commonly used approximation in photoabsorption applications is the ALDA. This approximation is used throughout our work and can be represented by

$$\delta V_{xc}(\vec{r},\omega) = \delta n(\vec{r},\omega) \left. \frac{\delta V_{xc,0}(\vec{r})}{\delta n(\vec{r'})} \right|_{n(\vec{r})=n_0(\vec{r})} \tag{6.14}$$

The determination of δn is done through a self-consistent iterative solution of equations 6.12, 6.13, and 6.14 in a procedure that will be described in more detail in subsequent sections.

6.2.2 Application to Photoabsorption

With a theoretical formulation established for calculating the induced density caused by a perturbation, we can use this for the specific problem of determining the absorption cross-sections

of atoms exposed to a perturbing photon. If we consider the photon as a classical field oscillating at a fixed frequency, ω, then we can easily apply the standard dipole approximation and represent the photon as an external perturbation of the form

$$\delta V_{ext}(\vec{r}) = \frac{1}{2}\varepsilon_0 z \tag{6.15}$$

where ε_0 is the magnitude of the photon's associated electric field. The description of the photon according to equation 6.15 is formed under several reasonable assumptions. Firstmost the dipole approximation allows us to treat the plane-wave photons as a dipole. This is a commonly used approximation that works well for most atomic systems. Secondly we assume that the unperturbed ground state system is spherically symmetric, and we can therefore choose an arbitrary polarization for the photon in order to simplify the calculation. This allows us to represent the spatial dependence of the photon's field along the z-axis of our system. Thirdly the fact that individual photons have only one frequency (corresponding to their energy, i.e. $\hbar\omega$) means that they only have a single Fourier component, which leads to the external perturbation from the photon having no explicit frequency dependence (in a more general description the frequency dependence could be written as $\delta(\omega - \omega_{photon})$). This point is also key as to why the linear response approximation works so well for photoabsorption, i.e. the independence of the external potential with respect to frequency means there is no need to account for higher order response in most cases.

With an explicit form for the external potential we can use the expressions of the previous section to determine the induced density, δn. For now we will leave the details on how this is done in practice and simply describe how δn can be used to obtain the observable quantities of interest. The practical determination of δn will be the focus of the next section. The induced density represents a displacement of charge from the ground state system, and therefore can be used to determine a dipole moment in the classical sense. The ratio of this induced dipole moment to the external field strength is the definition of the polarizability of the ground state system:

$$\alpha(\omega) = -\frac{2}{\varepsilon_0}\int z\delta n(\vec{r},\omega)d\vec{r} \tag{6.16}$$

The polarizability is a complex quantity that describes the degree to which the system is disturbed by a photon at frequency ω. The real part of α gives us an idea of how strongly the electrons in the system screen or enhance the absorption of the photon. In that sense the smaller the real part of α, the less important electron correlations and exchange effects are to the absorption process at that frequency. The imaginary part of α can be related through Fermi's Golden Rule to a measurable absorption cross section. This photoabsorption cross section is given by

$$\sigma(\omega) = 4\pi\frac{\omega}{c}\Im\alpha(\omega) \tag{6.17}$$

where c is the speed of light and $\Im$ denotes taking the imaginary part of the argument. This photoabsorption coefficient, σ, corresponds to the opacity in cases where photon scattering (i.e. change in photon momentum and energy coming from multiple collisions in the plasma) is negligible.

6.3 Practical Implementation of TD-DFT

This section will focus on the practical approaches used to solve the TDKS equations within the linear response regime. As was stated in previous sections, the TDKS equations may be formally exact, but a correct time-dependent exchange-correlation functional is needed to obtain the exact density response. Since this is a currently insurmountable problem, we must attempt to access the necessary information through a self-consistent field (SCF) scheme along with an approximate form for the xc functional (in our case the ALDA). Though SCF procedures are common in solving problems with many-body quantum mechanics (e.g. Hartree-Fock Theory and DFT), their stability is often dependent on having a reasonable initial guess at the correct solution to the problem. In our case, where we use an SCF approach to determine the converged induced density without time-dependent xc effects accounted for, we will use the induced density without interactions beyond the ground state treatment as our initial guess.

6.3.1 Independent Particle Approximation and χ_0

A commonly used approximation used to calculate excitation spectrum from ground state systems is the independent particle approximation. In this approximation, excitations of the system are treated as transitions between non-interacting states of the ground state system. In this sense the total excitation cross-section is the sum of the excitation cross-sections from all possible single-particle transitions within the system. For photoabsorption in this independent particle picture, standard perturbation theory allows us to write the cross-section as

$$\sigma_0(\omega) = \frac{4\pi^2\omega}{c}\sum_{i,j}(f_i - f_j)\left|\langle\psi_j|z|\psi_i\rangle\right|^2\delta(\omega - E_j + E_i) \tag{6.18}$$

where f_i is the occupation of state i, δ is the Dirac delta function which enforces energy conservation, and i and j correspond to the initial and final independent electron states with energies E_i and E_j, respectively. This equation clearly demonstrates no electron interactions during the timescale of the excitation, as both the initial and final state are eigenstates of the unperturbed KS Hamiltonian. This is a commonly used approximation within techniques which utilize effective non-interacting electron states (such as those in DFT). More refined methods determine the final state as an eigenstate of a perturbed Hamiltonian (the so-called orbital relaxation technique), but this scheme still does not account for interactions between the electrons or between different excitation channels (i.e. there should be interference between different excitations, i to j, i' to j', etc.).

In this work our main interest in the independent particle results is as a starting point to obtaining a more complete description of excitations through an SCF approach, but it is also useful for us to compare to methods which rely upon the independent particle to access excitation information from their electronic structure calculations. Fortunately the linear response TDKS equations already give us the information needed to obtain the independent particle quantities we need. The independent particle response requires only the KS response function, which we repeat here for the reader's convenience:

$$\chi_0(\vec{r},\vec{r'},\omega) = \sum_{i,j}(f_i - f_j)\frac{\psi_i^*(\vec{r})\psi_j(\vec{r})\psi_i(\vec{r'})\psi_j^*(\vec{r'})}{\omega - (E_j - E_i) + i\delta} \tag{6.11}$$

It is worth reiterating that the ψ are the single-particle KS states of the ground state system. This susceptibility can be used to determine the exact density response if the time-dependent xc functionals are known (see equation 6.13), but if these functionals are ignored it can be used to determine the response in the independent particle case:

$$\delta n_0(\vec{r},\omega) = \int \chi_0(\vec{r},\vec{r'},\omega)\delta V^{ext}(\vec{r'},\omega)d\vec{r'} \tag{6.19}$$

where we denote δn_0 as the density response of the system under the independent particle approximation. This response can be used as normal to obtain observable quantities such as the polarizability,

$$\alpha_0(\omega) = -\frac{2}{\varepsilon_0}\int z\delta n_0(\vec{r},\omega)d\vec{r} \tag{6.20}$$

If equation 6.20 is used with equation 6.17, the resulting photo-absorption cross-section is identical to equation 6.18, as expected.

Though equation 6.19 ties the independent particle approximation to the KS susceptibility function, the difficulty remains that we must calculate χ_0. The two summations needed to determine χ_0 must be carried out over all states of the KS ground state system, of which there are infinitely many. To explicitly determine χ_0 would practically require an approximation by truncating the sums. Fortunately we can direcly determine χ_0 using the Green's function associated with the KS Hamiltonian (for more details on the Green's function and its application in the ground state system, see Chapters 2 and 3). The Green's function contains an eigenfunction expansion (the Lehmann representation) of the form

$$G(\vec{r},\vec{r'},E) = \sum_m \frac{\psi_m(\vec{r})\psi_m^*(\vec{r'})}{E - E_m \pm i\delta} \tag{6.21}$$

where the sign of the infinitessimal depends on the boundary conditions chosen when solving the associated Green's function equation (i.e. the sign indicates whether determining the advanced or retarded Green's function). Our formulation chooses a positive infinitessimal and as such we construct the retarded Green's function.

Using the Green's function we can rewrite the KS susceptibility as

$$\chi_0(\vec{r},\vec{r'},\omega) = \sum_i f(E_i,\mu)\psi_i^*(\vec{r})\psi_i(\vec{r'})G(\vec{r},\vec{r'},E_i+\omega) + \sum_i f(E_i,\mu)\psi_i(\vec{r})\psi_i^*(\vec{r'})G^*(\vec{r},\vec{r'},E_i-\omega) \quad (6.22)$$

where we have applied the Fermi-Dirac statistics relevant to our warm dense systems with chemical potential μ and where we note that the sum in both terms is ostensibly over all of the electronic states, but the occupation factors given by the Fermi-Dirac functions effectively limit the summation over occupied states only. Note that the index i in the two terms can no longer be considered to correspond to the initial state.

Equation 6.22 is equivalent to equation 6.11, and therefore must preserve the same physical characteristics. First, energy conservation is preserved through the imaginary part of the Green's function, which contains poles at the eigenvalues of the bound states and is identically zero for all other negative energies. Since its argument is either $E_i + \omega$ or $E_i - \omega$, this enforces the same energy conservation seen from the delta function in equation 6.18. Second, transitions between occupied states must not be allowed. Though this is less obvious, the two terms in equation 6.22 contain equal but opposite parts that cancel out at the energies corresponding to a disallowed transition. Third, the information of all possible transition states is still present, but this time implicitly within the functional structure of the Green's functions themselves. With equation 6.22 the physics is preserved, but numerical implementation must be done carefully in order to preserve these basic properties of excitation processes. This will be discussed in later sections.

This reformulation of χ_0 gives us no benefit in terms of computational efficiency if equation 6.21 is used to determine G, as the calculation of the two Green's functions in equation 6.22

requires two separate summations over all states. However, the Green's function can be determined by a direct method which involves solving for the regular (i.e. divergent at infinity) and irregular (i.e. divergent at the origin) solutions of the Kohn-Sham Schrodinger equation. The product of those two solutions at a particular energy is used to construct the Green's function directly without the need for the eigenfunction expansion. For more details see the derivation of the radial expressions for the TD-DFT approach in Appendix A.3, but we give this expression here as well:

$$G_l(r, r', E) = \frac{j_l(r_<)h_l(r_>)}{W[j_l, h_l]} \tag{6.23}$$

where l is the angular momentum quantum number, j_l is the regular solution of the KS-Schrodinger equation (i.e. is regular at the origin), h_l is the irregular solution of the KS-Schrodinger equation (i.e. is irregular at the origin but converges as $r \to \infty$), and $W[f, g]$ is the Wronskian, defined by

$$W[f, g] = r^2 \Big[f(r)g'(r) - f'(r)g(r) \Big]_{r=a} \tag{6.24}$$

where the solution is independent of the choice of a. The regular and irregular solutions can be obtained through numerical integration, and robust algorithms were developed to do this for the Tartarus code (see Chapters 2 and 3 of this dissertation for more details).

Equation 6.23 is a significantly more accessible form of the Green's functions than equation 6.21, but the two contain equivalent information. The summation over infinitely many states is no longer required as it is contained implicitly within the Green's function, and we can now determine χ_0 with a sum over only the occupied KS states of the system.

6.3.2 Self Consistent Field Approach

To go beyond the independent particle approximation we need to determine information on how the electrons respond to each other as they are perturbed by the external potential. As was explained in section 6.2, we can find this information if we had full knowledge of the exact susceptibility, χ (equation 6.3) or equivalently if we have full knowledge of the effective TDKS

xc potential (equation 6.9). Given that knowledge of either gives the same density response, we can write a Dyson-like equation that illustrates how this problem lends itself to solution via a self-consistent procedure.

$$\chi(\vec{r},\vec{r'},\omega) = \chi_0(\vec{r},\vec{r'},\omega) + \int d\vec{r_1}\chi_0(\vec{r},\vec{r_1},\omega)\int d\vec{r_2}\left[\frac{1}{|\vec{r'}-\vec{r_2}|} + \frac{\delta V_{xc}(\vec{r'},\omega)}{\delta n(\vec{r_2},\omega)}\bigg|_{n_0}\right]\chi(\vec{r_2},\vec{r_1},\omega) \tag{6.25}$$

This expression defines χ in terms of itself, χ_0, and the Hartree and xc operators (the terms in brackets). A relation like this can be solved self consistently using an initial guess for χ on the right-hand side (the initial guess in our scheme is χ_0) and an assumed form for V_{xc}. Solutions for χ are iterated until the procedure yields the same results from one iteration to the next. Though this is formally equivalent to the procedure we carry out, we find that recasting the self consistent calculation in terms of the induced density is more intuitively pleasing and algorithmically simpler to implement than equation 6.25. In either approach our overall accuracy is limited by the approximations used to determine V_{xc}. In this section, we use a slight change of notation simply to illustrate that these quantities change iteratively throughout the scheme, but the converged quantities should in principal be the same as they are defined by the TDKS equations.

Our end goal is to obtain a converged form of the induced density, which will follow the form

$$\delta n^{SCF}(\vec{r},\omega) = \int \chi_0(\vec{r},\vec{r'},\omega)\phi_{SCF}(\vec{r'},\omega)d\vec{r'} \tag{6.26}$$

where ϕ_{SCF} is the total external field arising from the perturbation,

$$\phi^{SCF}(\vec{r},\omega) = \delta V_{ext}(\vec{r}) + \delta V_C(\vec{r},\omega) + \delta V_{XC}(\vec{r},\omega) \tag{6.27}$$

The electrostatic redistribution of electrons is contained within δV_C, which has the same form as the Hartree potential associated with the induced density:

$$\delta V_C(\vec{r},\omega) = \int \frac{\delta n^{SCF}(\vec{r'},\omega)}{|\vec{r}-\vec{r'}|}d\vec{r'} \tag{6.28}$$

To account for the other correlation and exchange effects felt under this redistribution, we simply apply a linearization of the xc potential about the unperturbed density:

$$\delta V_{XC}(\vec{r},\omega) = \delta n^{SCF}(\vec{r},\omega)\frac{\partial V_{XC}}{\partial n}\bigg|_{n=n_0(\vec{r})} \tag{6.29}$$

This is the ALDA described previously.

In summary of the preceding section, we use the independent particle induced density from equation 6.19 as our initial guess (which is formally equivalent to setting δV_C and δV_{XC} equal to zero in the first iteration), and we iteratively solve equations 6.26 – 6.29. At the end of this procedure we will have obtained the converged linear density response and the associated external potential.

Though we can determine the total photo-absorption cross-section using equation 6.17, it can also be instructive to see how the converged interacting system affects transitions from the viewpoint of single-particle KS states. We can express the fully converged photo-absorption cross-section in a form analogous to equation 6.18 by simply inserting the KS external potential from the SCF calculation in place of the normal dipole operator:

$$\sigma(\omega) = \frac{4\pi^2\omega}{c}\sum_{i,j}(f_i - f_j)\left|\langle\psi_j|\phi^{SCF}(r,\omega)Y^{10}(\hat{r})|\psi_i\rangle\right|^2\delta(\omega - E_j + E_i) \tag{6.30}$$

where ϕ^{SCF} is the radial dependence of the KS external potential (see equation A.4 in Appendix A).

6.3.3 Implementation in Radial Expressions

In order to provide a more useful guide to the expressions as they are implemented in our code, we provide the radial expressions that result from carrying out spherical harmonic expansions of all of the previous TD-DFT expressions and simplifying the angular algebra. This simplification and demonstration of the proper selection rules is shown in detail in Appendix A, and here we only present the final expressions.

In the code, a susceptibility-like term is used for algorithmic simplification instead of determining χ_0 explicitly. This term does not change throughout self-consistent iterations and is calculated at the beginning of the code:

$$\mathfrak{G}(r,r',\omega) = -\frac{1}{8}\sum_{i,l}(2l+1)f(E_{i,l})P_{i,l}(r)P_{i,l}(r') \times \sum_{l'}(2l'+1)\begin{pmatrix} l & l' & 1 \\ 0 & 0 & 0 \end{pmatrix}^2 \left[G_{l'}(r,r',E_{i,l}+\omega) + G_{l'}(r',r,E_{i,l}-\omega)\right] \quad (6.31)$$

The radial dependence of the induced density can be readily obtained from the following expression:

$$\delta n^r(r,\omega) = \int dr' r' \phi_\omega^{SCF}(r') \frac{\mathfrak{G}(r,r',\omega)}{r} \quad (6.32)$$

where

$$\delta n(\vec{r},\omega) = \delta n^r(r,\omega) Y_{10}(\hat{r}) \quad (6.33)$$

with the self-consistent induced field given by

$$\phi_\omega^{SCF}(r) = -\sqrt{\frac{4\pi}{3}}r - \frac{2}{\varepsilon_0}\left[\delta V_C^r(r,\omega) + \delta V_{XC}^r(r,\omega)\right] \quad (6.34)$$

where the independent particle solution (which is the first solution of the self-consistent procedure) is obtained by setting $\delta V_C^r = \delta V_{XC}^r = 0$.

The induced Coulomb potential is determined from the induced density according to

$$\delta V_C^r(r,\omega) = \frac{4\pi}{3}\left[\frac{1}{r^2}\int_0^r r'^3 \delta n^r(r',\omega)dr' + r\int_r^\infty \delta n^r(r',\omega)dr'\right] \quad (6.35)$$

and the XC induced potential is determined by

$$\delta V_{XC}^r(r,\omega) = \delta n^r(r,\omega)\left.\frac{\partial V_{XC}}{\partial n}\right|_{n=n_0(r)} \quad (6.36)$$

Figure 6.1 shows the SCF procedure for carrying out the TD-DFT approach to study a multi-electron system under a perturbation. Step 1 in the diagram corresponds to the ground

state density being perturbed by some external potential (in this case caused by a photon of frequency ω). Step 2 is where the electron susceptibility of the ground state system is used to determine the induced density due to the perturbation. In the independent particle scheme, the density induced by the initial photon perturbation is all that is required to determine the photo-absorption properties of the system, i.e. the process needs to only be carried out to step 2 to obtain the independent particle result. Step 3 determines the screening potentials that arise from the ground state density being perturbed, i.e. the potentials that arise from electron correlation and exchange within the density induced by the photon. Step 4 is when a new, self-consistently determined perturbation is formed from the initial external potential and the new screening potentials. If the perturbative potential is practically unchanged from the previous iteration, then the SCF procedure is converged.

6.3.4 Numerical Considerations

Implementation of the SCF scheme to determine the response of an electronic system to external perturbations is subject to the same difficulties encountered in any SCF approach. In order to vary the iteratively obtained induced potentials in such a way that we can obtained a converged result, we apply the same numerical techniques implemented in Tartarus (see Chapter 3.4.4 of this work for more details). Beyond the standard SCF scheme implementation, there are implicit difficulties that arise due to the implementation of the Green's functions formalism when determining χ_0. How these difficulties arise and how they can be addressed is the focus of this section.

As we can see from equations 6.31 and 6.32, the majority of the numerical work that needs to be done is in determining the radial part of the Green's function, $G_l(r, r', E)$ (done via equation 6.23). In order to determine $\mathfrak{G}$ in equation 6.31, we must evaluate the Green's function at energies equal to the independent electron energies shifted upwards and downwards by energy $\hbar\omega$, corresponding to the $G_l(r, r', E_i + \omega)$ and $G_l(r, r', E_i - \omega)$ terms, respectively. The Green's function is a complex function with poles at the independent particle eigenvalues of the KS Hamiltonian, i.e. the bound state energies of the non-interacting KS quasiparticles. Though the true Green's function has a branch cut along the positive real energy axis, we work

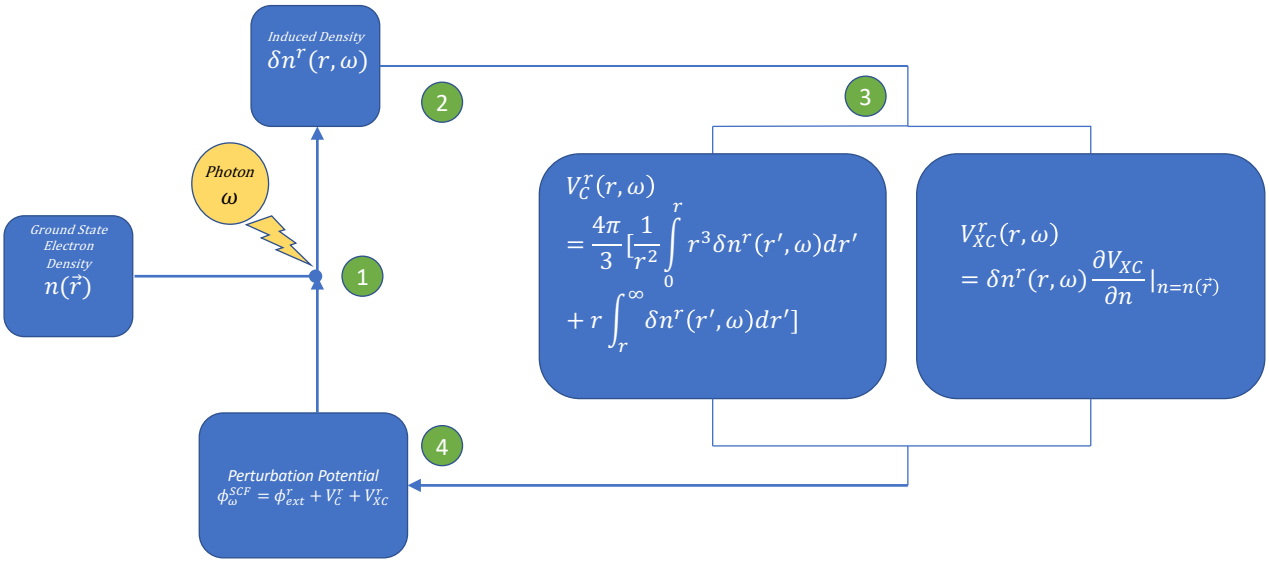

Figure 6.1: A schematic of the SCF procedure and radial functions used to determine the induced density.

with the retarded Green's function which avoids the jump discontinuity by being defined only on the upper-half of the complex energy plane.

It is well known that the imaginary part of the Green's function corresponds to the real electron density matrix (see Chapter 2.3.3 of this work for more details), and thus can be thought of as the part of the Green's function corresponding to observable quantities. Indeed this is one of the central ideas behind DFT: observable quantities are functionals of the electron density. Though this might imply that we only care about the imaginary part of the Green's function, the real part of the Green's function and hence the KS susceptibiliy couples to the imaginary part of the induced density through both the Hartree and xc induced external potentials (equations 6.35 and 6.36). This can also be seen in equation 6.25, where the real part of χ_0 is coupled to the imaginary part of χ through the Hartree and xc operators (i.e. the operators within the brackets). In short what this means is that we must determine the real part of χ_0 through the Green's functions in order to accurately determine the density response. It is through the behavior of the real part of the Green's function for negative energies that our main numerical difficulties arise.

When the photon frequency corresponds to a resonance between two occupied states (i.e. $E_i + \omega = E_j$ or $E_i - \omega = E_j$ where $i \neq j$ and E_j also corresponds to an eigenenergy of the system), no absorption should occur if the two states are equally occupied. If the states have differing occupations, then this would correspond to a bound-bound transition. This can be easily seen in equation 6.11 because the two Fermi-Dirac occupation factors would subtract to zero when equal. In the Green's function implementation of equation 6.22, we see the same result when the terms associated with $G(E_i + \omega)$ and $G(E_j - \omega)$ perfectly cancel out (being equal in magnitude and opposite in sign). Analytically we can easily see that the poles in the imaginary parts of the Green's functions in such a case have the same functional form and thus cancel out perfectly. The problem for us is that the same cannot be said of the real part of the Green's functions, which are finite but extremely large near resonant energies.

Our method of dealing with the poles in the imaginary part of the Green's function is quite simple: we avoid calculating the poles near resonant energies and set the imaginary part of the Green's function to zero when the energy argument is negative. Since the poles only exist

at the bound state eigenvalues and the imaginary part of the Green's function is zero for all negative energies, this is both an analytically sound and algorithmically simple solution. Still, the time-dependent xc effects determined by the SCF procedure should also have an effect on bound-bound transitions. We account for this by interpolating ϕ^{SCF} to determine its value at the resonant frequencies and then utilize equation 6.30 to determine the specific contribution the bound-bound transition has on the photo-absorption cross-section.

We must also treat the real part of the Green's function carefully near resonant frequencies between occupied states. Just as the imaginary parts should cancel out from the two Green's function terms when the resonant energy is between two equally occupied states, the real parts of those Green's function terms should cancel in such a way that χ_0 is well-behaved. Since these are large finite values determined numerically, it is very difficult to accurately subtract two such values and obtain a small quantity. When dealing with these large quantities in a numerical implementation, there are multiple ways to approach the problem. The simplest and often used method is to introduce a small imaginary part to the perturbing energy (i.e. $\omega = \omega_R + i\omega_I$). This shifts the evaluated energy away from the sharp features which lie along the real energy axis, and the values of the imaginary part of the Green's function become finite and must also be treated explicitly. The issue with this approach is that you are introducing a free parameter in the form of the imaginary part of the perturbing energy, ω_I. The parameter is introduced solely to solve a numerical issue and therefore can lead to small inaccuracies in the calculation, especially in parts of the photoabsorption spectrum surrounding the resonant frequency. For most applications this error does not seem to be a significant issue.

A similar but more physically justified approach is to determine an imaginary part of the resonant energies that is due to the physical reality that all electronic states have a finite lifetime. This corrects the issue of the divergences by introducing a complex value for the eigenenergies, but instead of using a small, adjustable parameter, the imaginary part of the energy is determined from the state lifetime (see for example Reference [18]). Once again the introduction of finite imaginary part (in this case it is introduced via the eigenernergy of the electronic state, but the result is equivalent to adding the same value as the imaginary part of the perturbing energy) allows one to avoid the divergences in the imaginary part of the

Green's function and smooth out the real part of the Green's function near the poles, and thus cancellation can be implemented numerically. The issue with this approach is that an additional model must be used in order to determine the lifetime, which both increases the computational cost and adds additional uncertainty. Further, it is typical that the obtained lifetimes must be modified by additional free parameters when frequencies are near a resonance [18].

Our numerical calculations have not had significant issues obtaining stable results when calculating the susceptibility near resonant frequencies, and although the code retains the capability to add an imaginary component to the frequency, we have not needed to do so for any of the cases of interest in this work. Much work was carried out in the development of Tartarus to obtain stable calculations of the Green's function, even when its value is significantly large. Even still, issues do arise when multiple resonant frequencies are near each other. This most commonly occurs at low frequencies near resonances between weakly bound states in heavier elements. In these systems the bound states are near the ionization threshold and tend to be quite numerous. Though the real part of the Green's function is most sharply valued at eigenvalues of the KS system, it is still finite near those eigenvalues, and this leads to large values of the real part of the susceptibility at frequencies near clusters of resonant frequencies. In these systems we have found that our calculations have stability issues at low frequencies, and those issues can be resolved by adding a small imaginary component to the frequency. Since loosely-bound states are expected to have large self-energy corrections, the methods used by Grimaldi et al. [18] would likely work quite well for these systems. We stress here again that all of the results shown in this work were done with purely real frequencies and energies as inputs to the Green's functions.

Beyond the treatment of the susceptibility near resonant frequencies, there is an additional nuance to the SCF scheme that should be discussed. In a typical photo-absorption calculation, energy conservation is enforced in part by requiring that no transitions between bound states are allowed unless the mediating photon has energy equal to the difference in the states' energies and the states have differing statistical occupations. Since the typical algorithmic approach is to separate the determination of a contributions into the spectra formed by bound-bound, bound-free, and free-free transitions, the bound-free spectra is typically calculated under the constraint

that the initial state energy, E_i, plus the exciting photon's energy, ω, is greater than the ionization threshold, $E = 0$ (i.e. $E_i + \omega > 0$). For the independent particle approximation, where no reorganization of the electronic structure occurs due to the perturbing photon, this ionization condition holds true and there is no contribution to the susceptibility from states where $E_i + \omega < 0$. When we allow the electrons to communicate in a time-dependent calculation, the picture is not so simple.

Keeping in mind that even the frequency-space representation of TD-DFT still formally describes time-dependent interactions with the perturbing photon and the ground state system, we can no longer only consider contributions to the bound-free absorption when the perturbing photon's frequency is large enough to ionize the bound electrons. This is because in time-dependent calculations the bound states are no longer stationary states and spread out in energy during the absorption process due to the uncertainty principle. You can also view this intuitively by realizing that an electron in a deeply bound state still feels a force from the photon's electric field (and is therefore perturbed) even if that electron is too deeply bound to be ionized or transition to an occupied bound state. Since our goal is to account for electron correlations and exchange effects within the absorption, we must consider how these deeply bound, off-resonance electrons affect the absorption of other electrons that could be ionized by the photon.

In the code we must account for electrons that would not contribute to the photoabsorption in the independent particle picture, and we do this by simply accounting for every bound state in the sum of equation 6.31. Unfortunately this is where our numerical limitations force us to introduce a lower cutoff to the sum, because the second Green's function term (with argument $E_{i,l} - \omega$) often needs to be evaluated at very large negative energies. This is especially true at higher frequencies, where $E_{i,l} - \omega$ is often below $-300\, E_H$. At these large negative arguments, our Green's function calculation is not stable and leads to errors in the calculation. As such we enforce a minimum energy cutoff, such that $E + \omega > E_{cut}$ and where $E_{cut} < 0$. We find that this cutoff works very well, as the perturbations of the very deeply bound electrons do not strongly couple with the ionization of the more weakly bound electrons (i.e. unless the electron states are near each other in energy, their coupling through the TDKS equations is relatively weak). Further, even when the photon is energetic enough to ionize deeply bound states, those

states tend to have large energy separations from adjacent states, and therefore including those states in the SCF solution of the TDKS equations is expected to cause a smaller effect than for the ionization of more weakly bound states.

The effects seen by not including these non-ionizing, off-resonance states in the susceptibility can be very significant. In Figure 6.2 we can see the photo-absorption cross-section for xenon near the the 4d ionization threshold. If we consider states such that $E_{cut} = -10E_H$, then we get a smooth redistribution of the 4d bound-free cross-section which accounts for screening from all of the states nearby in energy. If we limit the states such that $E_{cut} = 0E_H$ (i.e. only states that can be ionized by the photon), then we get a result that is vastly different from the converged SCF result. In addition, the $0E_H$ minimum case introduces a sharp feature in the cross-section near $4.4E_H$. This feature arises because that frequency corresponds to a bound-bound transition between two fully occupied states—the 4p and 5s states. The real part of the susceptibility gains a contribution from the 5s state because it could be ionized by the photon, but the more deeply bound 4p state is not considered. When both states are considered, their contribution to the real part of the susceptibility cancel out perfectly, removing this sharp unphysical feature.

6.4 Results

6.4.1 Neutral Gas Results

The first step in testing our implementation of the TD-DFT approach is to demonstrate results that reproduce those presented in previous theoretical works and compare with experiments. Our work is based on using the average atom model solved in Tartarus, and therefore the electronic structure obtained is representative of an atom within a plasma of finite temperature and density. In order to compare directly to neutral gases we must obtain a solution from Tartarus for plasmas at very low temperatures and densities. Even though Tartarus was designed primarily for calculations of finite density and temperature plasmas, our results compare excellently to those previously published, with the differences explainable by our use of finite temperature and density AA electron density and the choice of exchange-correlation functional used. In

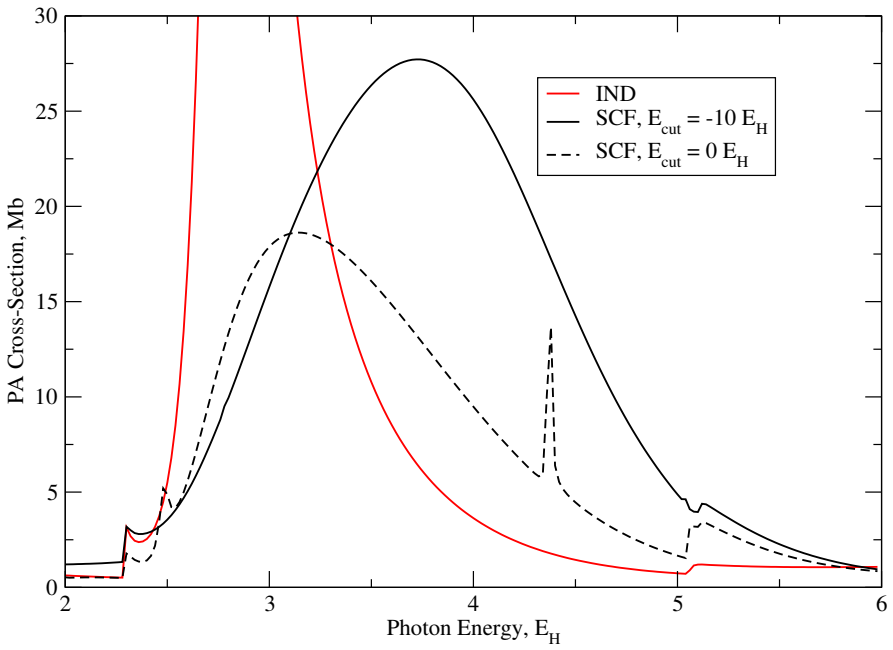

Figure 6.2: Here we see the results for the SCF calculation of the photo-absorption cross-section (σ) when we enforce a minimum energy as a criterion for whether we consider the contribution of an initial state to the susceptibility. IND refers to the independent particle solution, and SCF refers to self-consistent solutions to TDKS equations.

all of the work in this chapter, we use the exchange-correlation energy functional developed by Groth et al. [7]. In this section we will compare to digitized neutral gas results from Caizergues et al. [15].

Before results from our DFT-based model can be compared to experimental results, it is worth considering whether the DFT approaches can be directly compared to spectra, which involve the actual electrons and not KS quasiparticles. In previous chapters we discussed how DFT approaches suffer from describing quasiparticle energies as opposed to actual electron energies (i.e. the Kohn-Sham eigenergies do not inherently correspond to electron energy levels observed in nature), thus they often are not applicable to direct comparison to spectra, where transition edges correspond to the ionization energies of the electrons. However this disconnect between quasiparticle and actual electron energies does not change the trend one should see in the photo-absorption cross-sections, i.e. though the energies may be shifted, the scale of the redistribution of the cross-section due to time-dependent effects should be the comparable. Further, the shifts in eigenvalues are on the order of a few eV in energy, which is relatively small on the scale of a bound-free transition spectrum. This allows us to use this method to compare directly to experiment for these neutral gases, keeping in mind that there will be small shifts in the ionization threshold due to the use of approximate exchange-correlation functionals.

In Figure 6.3 we show good agreement with previous calculations as well as experimental results for neon. Though the reduction in the cross-section throughout the plot would seem to violate the f-sum rule for photoabsorption, the total spectrum sees an enhancement at higher frequencies that compensates for the apparent reduced absorption. The sharp peak near $.5E_H$ corresponds to the bound-free edge for the 2p state, and there are no other transitions until the 2s edge near $1.3E_H$. Even though the 2s state cannot be ionized by photons with energy less than $1.3E_H$, the state still screens the absorption of the photon by the 2p electron.

In Figure 6.4 we show good agreement with previous work for argon. Unlike in cold neutral neon, for argon we see a dramatic shift in the cross-section, indicating more absorption at higher frequencies. The screening of the absorption by the all of the argon electrons causes less lower-energy photons to be absorbed, and we even see a change in the location of the peak absorption frequency. This change in the relatively simple argon atom implies that the

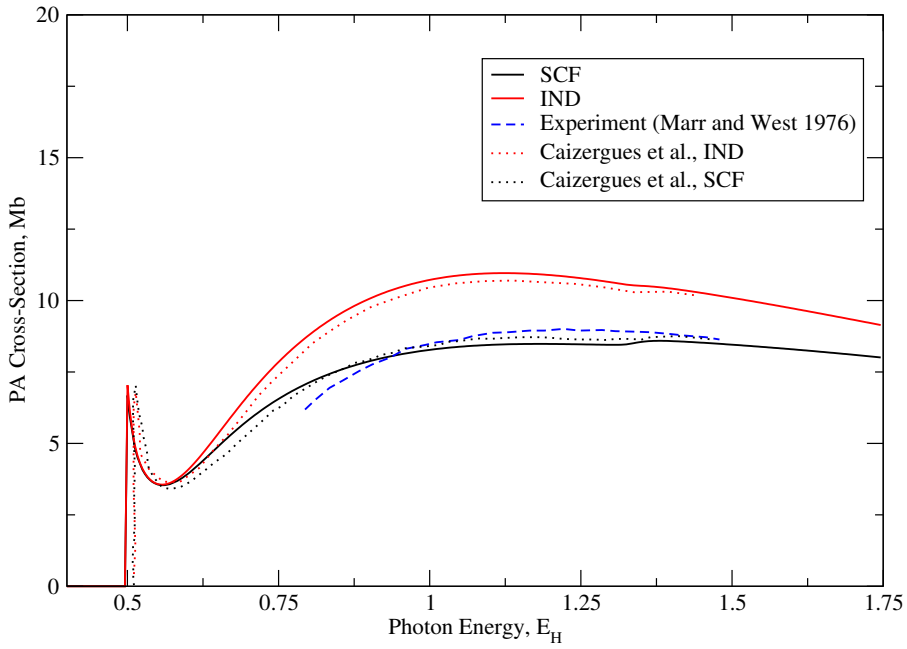

Figure 6.3: This figure shows the photo-absorption cross-section (σ) for neon compared to results digitized from Caizergues et al. [15] and to the experimental results of Marr and West [16]. We see a modest reduction of the cross-section in the SCF results for the frequency range shown on the plot. This reduction translates to a redistribution of the spectrum towards higher energies. The slight offsets in peak features (notably the 2p ionization near $.5E_H$) are due to the differences in exchange-correlation energy and to the finite temperature and density used in our calculation. IND refers to the independent particle solution, and SCF refers to self-consistent solutions to the TDKS equations.

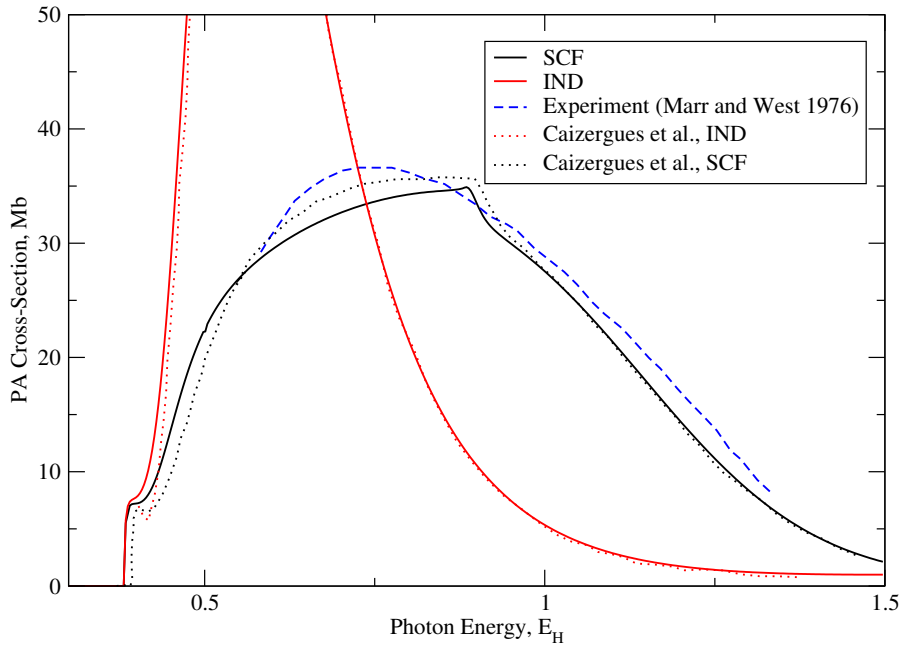

Figure 6.4: This figure shows the photo-absorption cross-section (σ) for argon compared to results digitized from Caizergues et al. [15] and to the experimental results of Marr and West [16]. We see a very dramatic shift of the cross-section towards higher frequencies, including changing where the peak absorption occurs in neon. IND refers to the independent particle solution, and SCF refers to self-consistent solutions to TDKS equations.

electron correlations accounted for by the SCF procedure could lead to significant changes in the absorption spectra of many systems. Of particular note in our calculation is the increase in prominence of the 3s bound-free transition near $.9E_H$. In the independent particle calculation the 3s edge is so small that it is not visible in the plot. For the SCF results, the 3s absorption shows as a strong increase in the spectrum even though the absorption by the 3p electron is stronger than it was for the independent particle result. This enhanced absorption of the 3p also translates to an increased absorption for the 3s electron, demonstrating that the correlations between the electrons as accounted for in the SCF scheme can both suppress and enhance the absorption. It should also be noted that the rearrangement of the 3p cross-section from its independent particle peak near $.6E_H$ to higher frequencies is due primarily to the interaction with the 3s state, which is closest in energy to the 3p state.

The final test of our implementation against the cold neutral gases is for xenon, which is shown in Figure 6.5. As in the case of argon, we see a dramatic rearrangement of the cross-section when the electron correlations are accounted for by the SCF scheme. Once again the more deeply bound electrons are able to cause a significant change in the absorption of the 4d electrons (near $2.25E_H$). Though not as prominent as in the argon case, we see an enhancement of the 4p absorption near $5E_H$. The slight enhancement seen here is likely due to the fact that the 4d electrons respond less strongly to the incident photon (as is evident by the decreasing cross-section leading up to $5E_H$), leading to corelations between the states being less important than in the analogous case for argon.

6.4.2 Finite Temperature Plasma Results

The atoms in a plasma exist at a finite temperature and density, which leads to the electrons in various ion stages being distributed over a multitude of states. The average atom model describes a system like this by occupying the electronic states according to Fermi-Dirac statistics. The effective chemical potential of the system is determined iteratively as part of the Tartarus calculation (see Chapters 2 and 3). This means that all electronic states are considered fractionally occupied according to the Fermi-Dirac distribution, and this includes the existence of free

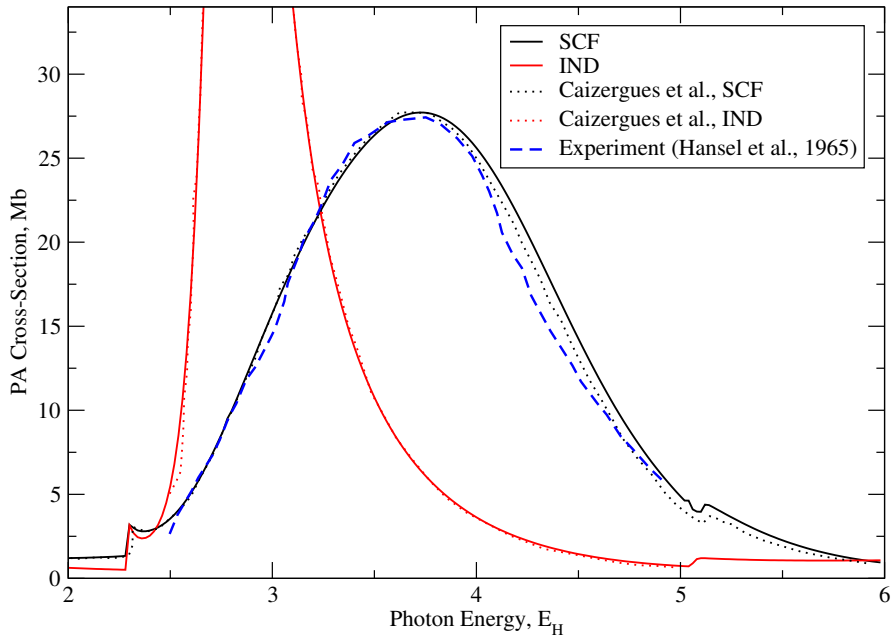

Figure 6.5: This figure shows the photo-absorption cross-section (σ) for xenon compared to results digitized from Caizergues et al. [15] and to the experimental results of Hansel et al. [17]. IND refers to the independent particle solution, and SCF refers to self-consistent solutions to TDKS equations.

electrons. In this way the average atom model implicitly accounts for the various ion stages through fractional occupation of the ground state.

In principle the free electrons in the system should respond to the external perturbation and each other, however the application to finite temperatures and densities requires no change to the formalisms presented previously if we do not consider the screening effects of cotinuum electrons on each other. Though for some systems this may represent a considerable contribution to the SCF screening potential, we believe that this approximation is well-justified when looking at the spectra arising from the ionization of bound electrons. Most of the screening or anti-screening effects that enter from the SCF procedure are strongest when the interacting states are near in energy. Thus, when a bound state is ionized, we would expect that the continuum electrons would not siginificantly impact the absorption. However, we do believe that for loosely-bound states and for systems that have strong continuum resonances, the screening arising from the continuum states is likely to be significant, if not the dominant source of the screening seen through the SCF procedure. For our initial work presented in this chapter, we will look at systems and cross-sections where we expect that the free electron contribution to the susceptibility will be small.

In Figure 6.6 we show the photo-absorption cross-section for solid density iron at a temperature of 100 eV. This spectrum was also shown by Grimauldi et al. [18] with the addition of self-energy corrections to the state lifetimes, and our work shows excellent agreement with their results. The prominent features of our SCF results are the Fano resonances that appear in the spectrum. These asymmetric line shapes arise due to inteference of the photon absorption from an underlying bound-bound transition. To be clear, our calculation includes no mechanism for state broadening and only includes bound-free transitions. These Fano resonances arise because the strong response of the bound states near a bound-bound transition leads to significant contributions to the real part of the susceptibility.

The asymmetry of the resonance features is due to how the resonant bound states screen or enhance the ionization. For photon energies less than, but near, the resonant bound-bound transition frequency, the lower bound state in the bound-bound transition rearranges significantly in such a way that it reduces the absorption. At the bound-bound transition frequency

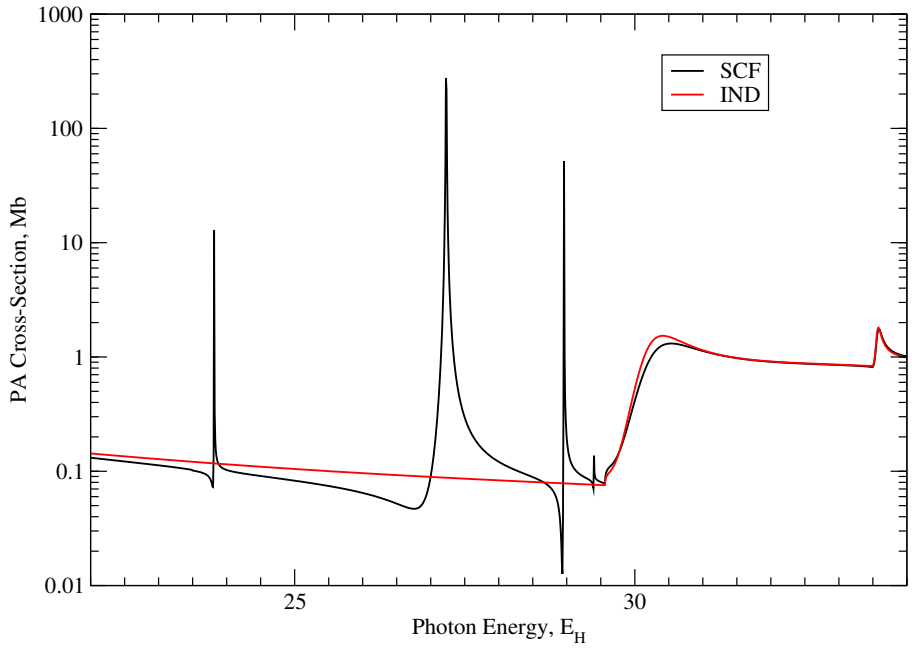

Figure 6.6: This figure shows the photo-absorption cross-section (σ) for solid density iron (7.85 $\mathrm{g/cm^3}$) at 100 eV. This work was also done by Grimaldi et al. [18], but the data in the publication could not be easily digitized without significant loss of quality. This figure is directly comparable to Figure 8 in Reference [18]. We see sharp features in the SCF results that arise from Fano resonances at frequencies corresponding to bound-bound transition energies. IND refers to the independent particle solution, and SCF refers to self-consistent solutions to the TDKS equations.

and higher energies, the interference is constructive and enhances the absorption. This effect is a general wave phenomenom that occurs in many different systems governed by wave dynamics, and in this case the resonance occurs because we couple the ionizing electron to the more deeply bound electron via their Coulomb interaction. This is analogous to the classical Fano resonance picture: two masses coupled together by a spring where one of the masses is exposed to a driving force. In our system, the ionizing electron is exposed to the driving force from the photon and is coupled to the more deeply bound electron via the SCF induced potentials (algorithmically, this coupling enters through the contribution of the deeply bound electron to the real part of the susceptibility).

Though our results for iron are at finite temperature, the Fano resonances arise in any system where we have a continuum scattering process with a background resonance process. To see this we performed a TD-DFT calculation of manganese at temperatures and densities meant to emulate the cold isolated atom limit. We chose this element because it was previously studied by Liberman and Doolen [144] in a theoretical model and was experimentally tested at Oak Ridge National Laboratory [19]. Our results are shown in Figure 6.7 and Figure 6.8. These figures are respectively comparable to Figures 1 and 2 of Reference [144]. These figures demonstrate that the Fano resonances shown in our results are realistic structures that should appear in the bound-free spectra if there is an underlying resonant feature (e.g. an underlying bound-bound transition).

6.5 Conclusions and Future Work

In this chapter we presented the basic formalisms behind the TD-DFT approach to studying absorption spectra in plasmas. Our goal for the work presented here was to show that the electronic density obtained from the average atom Tartarus code would be able to serve as an accurate ground state density for use in a TD-DFT calculation under the linear response approximation. This was done to a satisfactory degree for cold, neutral noble gases, which were studied experimentally and were the test cases for the first full linear response TD-DFT calculations. The results for those systems showed that even with a relatively simple electronic structure, exchange and correlations between electron states can enter into the time-dependent

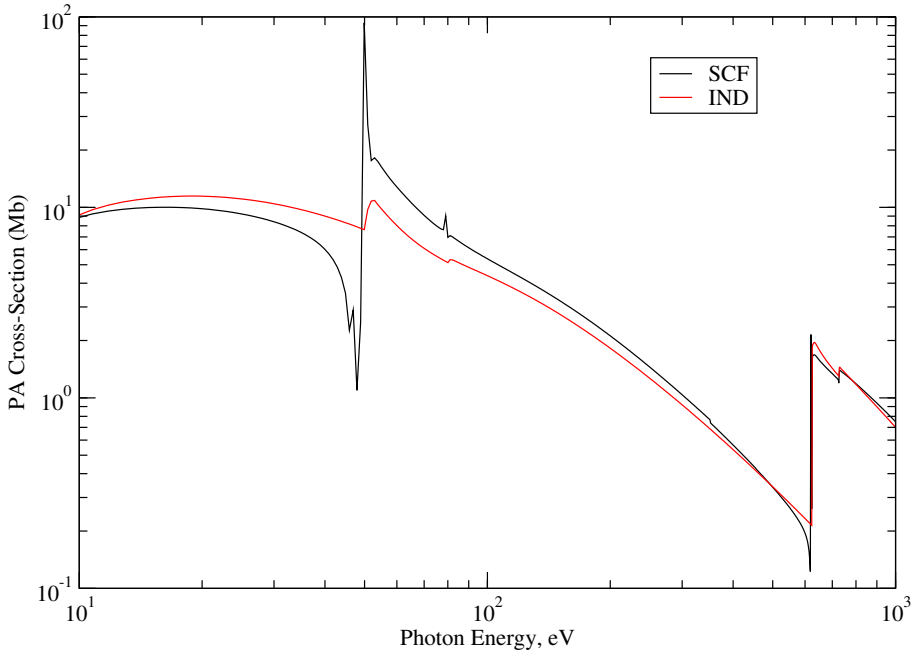

Figure 6.7: This figure shows the photo-absorption cross-section (σ) for cold manganese in the isolated atom limit. The primary features of interest are the Fano resonances that appear in the SCF solution. IND refers to the independent particle solution, and SCF refers to self-consistent solutions to TDKS equations.

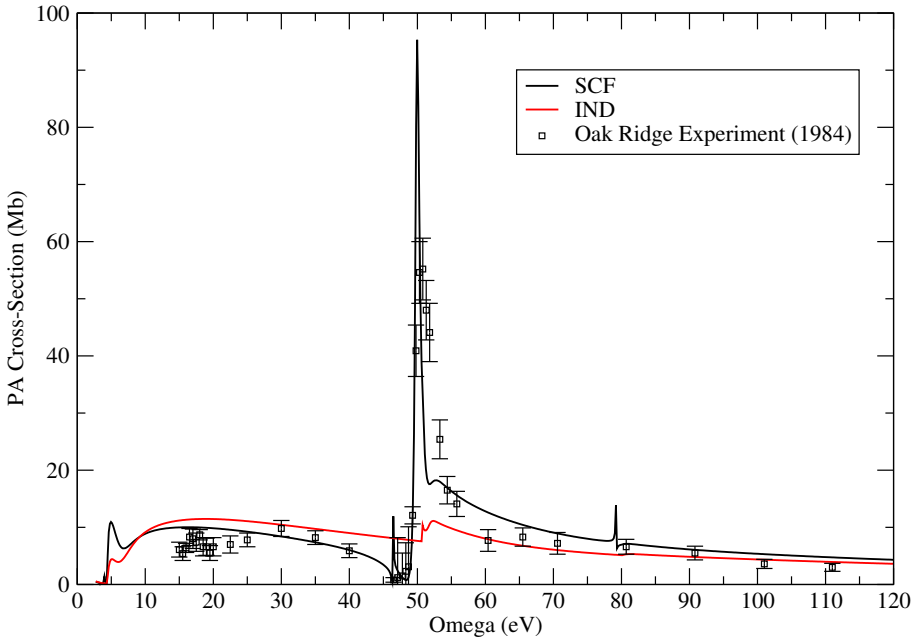

Figure 6.8: This figure shows the photo-absorption cross-section (σ) for cold manganese in the isolated atom limit compared to experimental results done at Oak Ridge [19]. The Fano resonance follows the experimental results quite nicely. The discrepencies at low frequency are likely due to temperature and density effects, as the weakly bound states involved in that part of the spectrum are particularly sensitive to the plasma conditions. IND refers to the independent particle solution, and SCF refers to self-consistent solutions of the TDKS equations.

absorption process in such a way that there are dramatic changes to spectra. The changes in the absorption spectra were not only simple shifts, but in some cases, such as for argon and xenon, significant redistributions of the bound-free absorption profiles. From these results alone it is clear that accounting for time-dependent electron correlations in photoabsorption is likely to be important for many systems.

We also implemented the TD-DFT approach for determining bound-free spectra at finite temperature and density, yielding interesting results that compared favorably to results previously published. Unlike the previous results, we did not implement self-energy corrections to broaden resonant features in the calculation, but we still saw strong features arising from the interaction of core resonances with the ionization process. These features took the form of Fano line-shapes, demonsrating both constructive and destructive interference between bound-bound and bound-free processes. Separate from these Fano resonances, we see a similar redistribution of the spectra from the SCF procedure, once again adding to the importance of accounting for the correlation physics when highly accurate spectra are required. As a further check, we also demonstrated the existence of these Fano profiles for materials in the neutral, isolated atom limit.

With the primary goal of replicating previous work satisfactorily achieved, we have confidence in our implementation of the TD-DFT approach used with our average atom electron density model. This will allow us to study systems at realistic plasma conditions, obtaining photo-absorption information for plasmas in the warm dense region and beyond. The work in this chapter also demonstrated that Tartarus has the capability to generate reasonable spectral results even in the low temperature and density regimes.

Our future work will at first be focused on studying finite temperature systems of interest to the opacity community, such as the 2015 Sandia opacity experiment [12] discussed in Chapter 5. It may be that the redistribution of the spectra that occurs due to the dynamic response of the electrons in TD-DFT could have significant impact on experimentally observed bound-free profiles.

Beyond the continued study of TD-DFT for bound-free profiles, our future work will involve the implementation of the formalism developed by Blenski to treat free-free transitions

[145]. We have already implemented the mathematical formalism from that work for bound-free transitions, and we obtain the same results as the implementation described in this chapter. Doing this will allow us to see exactly how important correlations between the free states as well as between free states and bound states are to absorption spectra. This will be of particular importance to systems where there are strong continuum resonances in the density of states, as well as for dense, heavy systems where we expect to see many weakly-bound states. Though this will primarily allow us to treat free-free transitions with dynamic response TD-DFT, the correlations between free states and bound states may also change the bound-free profiles.

Accounting for the free-free transitions is a computationally arduous task, as the continuum of states must be well resolved for numerical integrations. This is especially difficult to do when there are sharp, "pressure-ionized" resonances in the continuum. This issue was addressed by the Tartarus Green's function formalism described in Chapters 2 and 3 of this work. We will develop and implement a similar formalism for the TD-DFT calculations which will allow us to use a complex contour integration to lessen the computational burden of accounting for all of the continuum states. The use of the contour integration will also serve to fix any of the issues with resonant features adding computational instability to the calulcation, as all of the large features that contribute to the real part of the susceptibility can be smoothly accounted for by the contour integration.

Chapter 7

Conclusions

The difficulties in describing dense plasmas require a myriad of techniques drawn from various fields of physics. The average atom model meets many of these difficulties by incorporating techniques and concepts from atomic physics and plasma physics to determine an electron density that is statistically relevant to warm dense systems. Though efficient compared to other approaches, the average atom methods have still historically suffered from computational difficulties that limited their usefulness in generating large tables of plasma data such as equation of state. In Chapters 2 and 3 we describe the formalism we developed using Green's functions and complex energy integration to determine the average atom electron density. The robustness of this scheme, implemented in the Tartarus code, allows users to generate large tables of data without the need to manually adjust numerical parameters at various plasma temperatures and densities, and the code we developed can be run in a relativistic or nonrelativistic mode. We show good results for equation of state compared to other methods and experiments.

The average atom model provides a strong starting point to build up models with additional physics incorporated. In Chapter 4 we use the pseudoatom model to extract information on the ion correlations within the plasma in the form of a mean-force scattering potential. This potential can be used to generate electronic states influenced by correlations with other ions in the plasma (as opposed to states dependent only on interactions within a central ion). This can lead to significant changes in the continuum and weakly bound electron states, which in turn can have signficant effects on the low-frequency parts of the electrical conductivity.

In Chapter 5 the pseudoatom model is coupled to a molecular dynamics simulation in order to obtain results for the ion-ion dynamic structure factor that are in good agreement with

more expensive calculations. Using this method to study mixtures of carbon and hydrogen show the first prediction of so-called ”fast sound” effects in warm dense plasmas. The method was found to compare well other more expensive, less approximate techniques.

In Chapter 6 we use the ground state electron density obtained from the Tartarus code as an initial state for a time-dependent density functional theory calculation. We show that the TD-DFT code we developed is capable of obtaining good agreement for opacities with similar calculations for cold neutral systems. Further we use the finite temperature and density results from Tartarus to obtain time-dependent results for the opacity of warm dense iron. The work on using the average atom ground state in TD-DFT calculations is ongoing.

Appendices

Appendix A

Radial Expressions of the TD-DFT Formalism

This chapter provides the expansion of the expressions relevant to the TD-DFT formalism in spherical coordinates. Most terms used in the approaches implemented in this work are either naturally spherically or azimuthally symmetric, which makes a spherical coordinate representation efficient for use in our work. We start first with an expansion of the bound KS orbitals over spherical harmonics:

$$\psi_i(\vec{r}) = \sum_{l,m} \frac{P_{i,l}(r)}{r} Y_{l,m}(\hat{r}) \tag{A.1}$$

where $P_{i,l}(r)$ are the radial functions associated with a state at energy E_i and orbital angular momentum quantum number l, m is the projection of the angular momentum on the z axis (i.e. the magnetic quantum number), and $Y_{l,m}$ are the spherical harmonic functions.

The Green's functions can also be expanded in terms of spherical harmonics by

$$G(\vec{r}, \vec{r'}, E) = \sum_{l,m} G_l(r, r', E) Y^*_{l,m}(\hat{r}) Y_{l,m}(\hat{r'}) \tag{A.2}$$

With these two expansions, we can rewrite equation 6.22 as

$$\chi_0(\vec{r}, \vec{r'}, \omega) = \sum_i f(E_i, \mu) \sum_{l',m'} \frac{P_{i,l'}(r) P_{i,l'}(r')}{r r'} Y^*_{l',m'}(\hat{r}) Y_{l',m'}(\hat{r'}) \sum_{l,m} Y^*_{l,m}(\hat{r}) Y_{l,m}(\hat{r'}) G_l(r, r', E_i + \omega) + \ldots \tag{A.3}$$

where only the first term of χ_0 is explicitly shown for concision. The second term containing $G^*(\vec{r}, \vec{r'}, E_i - \omega)$ is analogous to the first and can be easily treated in the same manner using the expression $G^*(\vec{r}, \vec{r'}, E) = G(\vec{r'}, \vec{r}, E)$.

A.1 Treatment of Angular Dependence of δn

Since the external field is assumed to be directed along the z axis (see equation 6.15), we only expect the symmetry along the z axis to be broken, leading to an azimuthally symmetric induced potential (or equivalently, an azimuthally symmetric induced density). With this knowledge we can write the induced density in spherical coordinates with an appropriate azimuthally symmetric form:

$$\phi_{SCF}(\vec{r}, \omega) = -\frac{1}{2}\varepsilon_0 \phi_\omega^{SCF}(r) Y_{10}(\hat{r}) \tag{A.4}$$

With the form of the SCF potential (with the only unknown/iterated part being the radially dependent $\phi_\omega^{SCF}(r)$), we can write the density displacement as

$$\begin{aligned}\delta n(\vec{r}, \omega) &= -\frac{1}{2}\varepsilon_0 \int \chi_0 \phi_\omega^{SCF}(r') Y_{10}(\hat{r'})(r')^2 dr' d\hat{r'} \\ &= -\frac{1}{2}\varepsilon_0 \int dr'(r')^2 \phi_\omega^{SCF}(r') \sum_i f(E_i) \sum_{lm} \sum_{l'm'} \frac{P_{il'}(r) P_{il'}(r')}{r r'} Y^*_{l'm'}(\hat{r}) Y^*_{lm}(\hat{r}) G_l(r, r'; E_i + \hbar\omega) \\ &\qquad \times \int Y_{l'm'}(\hat{r'}) Y_{lm}(\hat{r'}) Y_{10}(\hat{r'}) d\hat{r'} + \ldots\end{aligned} \tag{A.5}$$

Now we can use the following identity to evaluate the integral over $\hat{r'}$

$$\begin{aligned}&\int Y_{l_1 m_1}(\hat{r}) Y_{l_2 m_2}(\hat{r}) Y_{l_3 m_3}(\hat{r}) d\hat{r} = \\ &\qquad \sqrt{\frac{(2l_1+1)(2l_2+1)(2l_3+1)}{4\pi}} \begin{pmatrix} l_1 & l_2 & l_3 \\ m_1 & m_2 & m_3 \end{pmatrix} \begin{pmatrix} l_1 & l_2 & l_3 \\ 0 & 0 & 0 \end{pmatrix}\end{aligned} \tag{A.6}$$

which yields the following expression for the density displacement

$$\delta n(\vec{r},\omega) = -\frac{1}{2}\varepsilon_0 \int dr'(r')^2 \phi_\omega^{SCF}(r') \sum_i f(E_i) \sum_{lm} \sum_{l'm'} \frac{P_{il'}(r) P_{il'}(r')}{rr'} \times Y^*_{l'm'}(\hat{r}) Y^*_{lm}(\hat{r}) G_l(r,r';E_i+\hbar\omega) \times \sqrt{\frac{3(2l'+1)(2l+1)}{4\pi}} \begin{pmatrix} l & l' & 1 \\ m & m' & 0 \end{pmatrix} \begin{pmatrix} l & l' & 1 \\ 0 & 0 & 0 \end{pmatrix} + \ldots \quad \text{(A.7)}$$

We can further simplify this expression and retrieve the expected azimuthal symmetry by making use of the following identity

$$Y_{l_1 m_1}(\hat{r}) Y_{l_2 m_2}(\hat{r}) = \sum_{l_3=|l_1-l_2|}^{|l_1+l_2|} \sqrt{\frac{(2l_1+1)(2l_2+1)(2l_3+1)}{4\pi}} \times \begin{pmatrix} l_1 & l_2 & l_3 \\ m_1 & m_2 & m_1+m_2 \end{pmatrix} \begin{pmatrix} l_1 & l_2 & l_3 \\ 0 & 0 & 0 \end{pmatrix} Y_{l_3, m_1+m_2} \quad \text{(A.8)}$$

and then, accounting for the sum over m and m' in equation A.7 to make use of the orthogonality of the 3-j coefficients, arrive at the simplified form for the density displacement with explicit azimuthal symmetry

$$\delta n(\vec{r},\omega) = -\frac{1}{2}\varepsilon_0 \int dr'(r')^2 \phi_\omega^{SCF}(r') \sum_i f(E_i) \sum_{l} \sum_{l'} \frac{P_{il'}(r) P_{il'}(r')}{rr'} G_l(r,r';E_i+\hbar\omega) \times \frac{(2l'+1)(2l+1)}{4\pi} \begin{pmatrix} l & l' & 1 \\ 0 & 0 & 0 \end{pmatrix}^2 Y^*_{10}(\hat{r}) + \ldots \quad \text{(A.9)}$$

Note that the 3-j coefficient in equation A.9 greatly truncates the summation for a given angular momentum as its value is 0 when the condition $l' = l \pm 1$ is not met.

We shall make a trivial definition just to simplify the following expressions and ease with which the expressions involving δn can be implemented in the code:

$$\delta n(\vec{r},\omega) = \delta n^r(r,\omega) Y_{10}(\hat{r}) \quad \text{(A.10)}$$

A.2 Resulting Expressions for δV_C and δV_{XC}

Both the Coulombic induced field (see δV_C in equation 6.28) and the XC induced field (see δV_{XC} in equation 6.29) are dependent solely on the induced density:

$$\delta V_C(\vec{r},\omega) = \int \frac{\delta n(\vec{r'},\omega)}{|\vec{r}-\vec{r'}|} d\vec{r'} \tag{A.11}$$

$$\delta V_{XC}(\vec{r},\omega) = \left.\frac{\partial V_{XC}}{\partial n}\right|_{n=n(\vec{r})} \delta n(\vec{r},\omega) \tag{A.12}$$

With an azimuthally symmetric form of the density displacement given by equation A.9, we can now explicitly write out the expression for the Coulombic part of the induced field. As can easily be seen from equation A.12, there is no need to write out an expression for δV_{XC} as it is simply linearly dependent on δn (with the slope being determined by the choice of exchange-correlation functional and the equilibrium electron density, which does not change over the SCF iterations). In order to explicitly write out equation A.11 in terms of its angular and radial components, we must first carry out the Laplace expansion:

$$\frac{1}{|\vec{r}-\vec{r'}|} = \sum_{l=0}^{\infty} \frac{4\pi}{2l+1} \sum_{m=-l}^{l} \frac{r_<^l}{r_>^{l+1}} Y_{l,-m}(\hat{r}) Y_{lm}(\hat{r'}) \tag{A.13}$$

where $r_< = \min(r,r')$ and $r_> = \max(r,r')$. With this expansion, we can write out δV_C with the use of Equation A.7 (used here instead of equation A.9 simply because the algebraic simplification is easier to see) as

$$\delta V_C(\vec{r},\omega) = -\frac{1}{2}\varepsilon_0 \int dr' d\hat{r'}(r')^2 \int dr''(r'')^2 \phi_\omega^{SCF}(r'') \times \sum_i f(E_i) \sum_{lm} \sum_{l'm'} \sum_{l''m''} \frac{P_{il'}(r')P_{il'}(r'')}{r'r''} \times Y^*_{l'm'}(\hat{r'})Y^*_{lm}(\hat{r'})G_l(r',r'';E_i+\hbar\omega)\sqrt{\frac{3(2l'+1)(2l+1)}{4\pi}} \times \begin{pmatrix} l & l' & 1 \\ m & m' & 0 \end{pmatrix} \begin{pmatrix} l & l' & 1 \\ 0 & 0 & 0 \end{pmatrix} \frac{4\pi}{2l''+1}(-1)^{m''} \frac{r_<^{l''}}{r_>^{2l''+1}} \times Y_{l'',-m''}(\hat{r})Y_{l''m''}(\hat{r'}) + ... \quad \text{(A.14)}$$

where once again we will be able to make use of the integration of the full angle to simplify the summations. The integration can be carried out as

$$\int Y^*_{l'm'}(\hat{r'})Y^*_{lm}(\hat{r'})Y_{l''m''}(\hat{r'})d\hat{r'} = \sqrt{\frac{(2l'+1)(2l+1)}{4\pi(2l''+1)}} C(l,l',l'';m,m',m'')C(l,l',l'';0,0,0) \quad \text{(A.15)}$$

where C are the Clebsch-Gordon coefficients, which are related to the 3-j coefficients by

$$C(j_1,j_2,j_3;m_1,m_2,m_3) = (-1)^{j_1-j_2+m_3}\sqrt{2j_3+1} \begin{pmatrix} j_1 & j_2 & j_3 \\ m_1 & m_2 & m_3 \end{pmatrix} \quad \text{(A.16)}$$

which allows us to rewrite Equation A.15 as

$$\int Y^*_{l'm'}(\hat{r'})Y^*_{lm}(\hat{r'})Y_{l''m''}(\hat{r'})d\hat{r'} = \sqrt{\frac{(2l+1)(2l'+1)(2l''+1)}{4\pi}}(-1)^{2(l-l')+m''} \begin{pmatrix} l & l' & l'' \\ m & m' & -m'' \end{pmatrix} \begin{pmatrix} l & l' & l'' \\ 0 & 0 & 0 \end{pmatrix} \quad \text{(A.17)}$$

We can also make use of the orthogonality relationship for the 3-j coefficients

$$\sum_{m,m'} \begin{pmatrix} l & l' & l'' \\ m & m' & -m'' \end{pmatrix} \begin{pmatrix} l & l' & l'' \\ m & m' & 0 \end{pmatrix} = \delta_{l'',1}\delta_{-m'',0}\frac{1}{2l''+1} \tag{A.18}$$

Taking the integration, the orthogonality relationship and the sum over $l", m"$ in equation A.14 into account, we arrive at the final expression for the Coulombic part of the induced potential

$$\begin{aligned}\delta V_C(\vec{r},\omega) = -\frac{1}{2}\varepsilon_0 \int dr'(r')^2 \int dr''(r'')^2 \phi_\omega^{SCF}(r'') \\ \times \sum_i f(E_i) \sum_l \sum_{l'} \frac{P_{il'}(r')P_{il'}(r'')}{r'r''} G_l(r',r'';E_i+\hbar\omega) \\ \times \frac{(2l'+1)(2l+1)}{3}\frac{r_<}{r_>^2} Y_{10}(\hat{r}) \begin{pmatrix} l & l' & 1 \\ 0 & 0 & 0 \end{pmatrix}^2 + ...\end{aligned} \tag{A.19}$$

which has azimuthal symmetry, as expected. This expression can be easily recast in terms of the induced density, at which point we retrieve the intuitive and easily implementable expression

$$\begin{aligned}\delta V_C(\vec{r},\omega) = \int d\hat{r'} dr' r'^2 \sum_{lm} \frac{4\pi}{2l+1}\frac{r_<^l}{r_>^{l+1}} Y_{l,-m}(\hat{r}) Y_{lm}(\hat{r'}) Y_{10}(\hat{r'}) \delta n^r(r',\omega) \\ = \frac{4\pi}{3}\left[\frac{1}{r^2}\int_0^r r'^3 \delta n^r(r',\omega)dr' + r\int_r^\infty \delta n^r(r',\omega)dr'\right] Y_{10}(\hat{r})\end{aligned} \tag{A.20}$$

We can easily see from equation A.20 that we need to simply carry out integrations over δn^r (which, as a reminder, is simply the radial dependence of $\delta n(\vec{r},\omega)$) to determine the induced Coulombic potential. This provides a great simplification in the algorithm, and this expression does not change from a nonrelativistic to a relativistic implementation.

A.3 Determination of $G_l(r, r', E)$

If we consider the Green's function as satisfying the following relationship

$$\left[E + \frac{1}{2}\nabla^2 + V_{eff}(\vec{r})\right] G(\vec{r}, \vec{r'}, E) = \delta(\vec{r} - \vec{r'}) \tag{A.21}$$

which is the differential equation associated with the Green's function as a propogator of a Schrodinger-like equation (in this case the KS-Schrodinger equation), then we determine the radial part of the Green's function by using

$$G_l(r, r', E) = \frac{j_l(r_<)h_l(r_>)}{W[j_l, h_l]} \tag{A.22}$$

where j_l is the regular solution of the KS-Schrodinger equation (i.e. is regular at the origin), h_l is the irregular solution of the KS-Schrodinger equation (i.e. is irregular at the origin but converges as $r \to \infty$), and $W[f, g]$ is the Wronskian, defined by

$$W[f, g] = r^2 \left[f(r)g'(r) - f'(r)g(r)\right]_{r=a} \tag{A.23}$$

where the solution is independent of the choice of a. The regular and irregular solutions can be obtained through numerical integration, and robust algorithms were developed to do this for the Tartarus code (see Chapters 2 and 3 of this dissertation for more details).

A.4 Expressions Implemented in Code

This section provides the detailed set of expressions that are implemented in the code, including the necessary prefactors that arise from the angular integrals and azimuthal symmetry. First we present the self-consistent potential terms needed to carry out the self-consistent field scheme. Taking the decomposition shown in equations A.4 and 6.27, we get

$$\phi_{SCF}(\vec{r}, \omega) = -\frac{1}{2}\varepsilon_0 \phi_\omega^{SCF}(r) Y_{10}(\hat{r}) = \phi^{ext}(\vec{r}) + \phi^{ind}(\vec{r}, \omega) \tag{A.24}$$

where

$$\phi^{ext}(\vec{r}) = \frac{1}{2}\varepsilon z = \frac{1}{2}\sqrt{\frac{4\pi}{3}}\varepsilon r Y_{10}(\hat{r}) \tag{A.25}$$

and

$$\phi^{ind}(\vec{r},\omega) = \delta V_C(\vec{r},\omega) + \delta V_{XC}(\vec{r},\omega) = \left[\delta V_C^r(r,\omega) + \delta V_{XC}^r(r,\omega)\right] Y_{10}(\hat{r}) \tag{A.26}$$

where δV_C and δV_{XC} have had the radial dependence trivially extracted in order to define δV_C^r and δV_{XC}^r. This allows us to solve for the radial dependence of the induced field as

$$\phi_\omega^{SCF}(r) = -\sqrt{\frac{4\pi}{3}}r - \frac{2}{\varepsilon_0}\left[\delta V_C^r(r,\omega) + \delta V_{XC}^r(r,\omega)\right] \tag{A.27}$$

where the magnitude of the photon's electric field, ε_0, will cancel out the same term implicitly included in both induced fields, giving no algorithm dependence on the electric field strength.

A.5 Unchanging Susceptibility-Like Term

The self-consistent field calculation iterates over a changing induced density and the associated induced potentials, but the underlying electron susceptibility (equation A.3) does not change throughout the iterative procedure. As such, in the code we consolidate the unchanging terms into an expression that is functionally equivalent to the susceptibility (but includes additional constant prefactors from the angular simplifications due to the azimuthal symmetry):

$$\begin{aligned}\mathfrak{G}(r,r',\omega) = &-\frac{1}{8}\sum_{i,l}(2l+1)f(E_{i,l})P_{i,l}(r)P_{i,l}(r') \\ &\times \sum_{l'}(2l'+1)\begin{pmatrix} l & l' & 1 \\ 0 & 0 & 0 \end{pmatrix}^2 \left[G_{l'}(r,r',E_{i,l}+\omega) + G_{l'}(r',r,E_{i,l}-\omega)\right]\end{aligned} \tag{A.28}$$

which allows us to determine the induced density according to

$$\delta n^r(r,\omega) = \int dr' r' \phi_\omega^{SCF}(r')\frac{\mathfrak{G}(r,r',\omega)}{r} \tag{A.29}$$

A.6 Polarizability

The final quantity that is typically extracted from the code in order to determine the photoabsorption cross-section is the polarizability. With the simple decomposition into radial terms that we have presented in this appendix, we can simply express the polarizability as

$$\begin{aligned}\alpha(\omega) &= -\frac{2}{\varepsilon_0}\int z\delta n(\vec{r},\omega)d\vec{r} \\ &= -\frac{2}{\varepsilon_0}\int r(\sqrt{\frac{4\pi}{3}})\delta n^r(r,\omega)Y_{10}(\hat{r})Y_{10}(\hat{r})r^2 dr d\hat{r} \\ &= -\frac{2}{\varepsilon_0}\sqrt{\frac{4\pi}{3}}\int r^3\delta n^r(r,\omega)dr \quad \text{(A.30)}\end{aligned}$$

References

[1] C.E. Starrett and D. Saumon. A simple method for determining the ionic structure of warm dense matter. *High Energy Density Physics*, 10(0):35 – 42, 2014.

[2] Burkhard Militzer and Kevin P. Driver. Development of path integral monte carlo simulations with localized nodal surfaces for second-row elements. *Phys. Rev. Lett.*, 115:176403, Oct 2015.

[3] L. V. Al'tshuler, A. A. Bakanova, I. P. Dudoladov, E. A. Dynin, and B. S. Chekin R. F. Trunin. Shock adiabats for metals. new data, statistical analysis and general regularities. *J. Appl. Mech. Techn. Phys.*, 22:145, 1981.

[4] L. V. Al'tshuler, K. K. Krupnikov, and M. I. Brazhnik. Dynamical compressibility of metals under pressure from 400000 to 4 million atmospheres. *Sov. Phys. JETP*, 34:886–893, 1958.

[5] R. P. Feynman, N. Metropolis, and E. Teller. Equations of state of elements based on the generalized fermi-thomas theory. *Phys. Rev.*, 75:1561–1573, May 1949.

[6] J. P. Perdew and A. Zunger. *Phys. Rev. B*, 23:5048, 1981.

[7] S. Groth, T. Dornheim, T. Sjostrom, F. D. Malone, W. M. C. Foulkes, and M. Bonitz. Ab initio exchange-correlation free energy of the uniform electron gas at warm dense matter conditions. *Phys. Rev. Lett.*, 119:135001, 2017.

[8] B. B. L. Witte, P. Sperling, M. French, V. Recoules, S. H. Glenzer, and R. Redmer. Observations of non-linear plasmon damping in dense plasmas. *Physics of Plasmas*, 25:056901, 2018.

[9] C. E. Starrett. Potential of mean force for electrical conductivity of dense plasmas. *High Energy Density Phys.*, 25:8–14, 2017.

[10] S. X. Hu, L. A. Collins, T. R. Boehly, J. D. Kress, V. N. Goncharov, and S. Skupsky. First-principles thermal conductivity of warm-dense deuterium plasmas for inertial confinement fusion applications. *Phys. Rev. E*, 89:165113, 2014.

[11] M. Krief, Y. Kurzweil, A. Feigel, and D. Gazit. The effect of ionic correlations on radiative properties in the solar interior and terrestrial experiments. *The Astrophysical Journal*, 856:2, 2018.

[12] J. E. Bailey, T. Nagayama, G. P. Loisel, G. A. Rochau, C. Blancard, J. Colgan, Ph. Cosse, G. Faussurier, C. J. Fontes, F. Gilleron, I. Golovkin, S. B. Hansen, C. A. Iglesias, D. P. Kilcrease, J.J. MacFarlane, R. C. Mancini, S. N. Nahar, C. Orban, J.-C Pain, A. K. Pradhan, M. Sherril, and B. G. Wilson. A higher-than-predicted measurement of iron opacity at solar interior temperatures. *Nature*, 517:56–59, 2015.

[13] H. R. Rüter and R. Redmer. *Phys. Rev. Lett.*, 112:145007, 2014.

[14] T. G. White, S. Richardson, B. J. B. Crowley, L. K. Pattison, J. W. O. Harris, and G. Gregori. *Phys. Rev. Lett.*, 111:175002, 2013.

[15] C. Caizergues, T. Blenski, and R. Piron. Dynamic linear response of atoms in plasmas and photo-absorption cross-section in the dipole approximation. *High Energy Density Physics*, 18:7 – 13, 2016.

[16] G.V. Marr and J.B. West. Absolute photoionization cross-section tables for helium, neon, argon, and krypton in the vuv spectral regions. *Atomic Data and Nuclear Data Tables*, 18(5):497 – 508, 1976.

[17] R. Haensel, G. Keitel, P. Schreiber, and C. Kunz. Optical absorption of solid krypton and xenon in the far ultraviolet. *Physical Review*, 188(3):1375–1380, 1969. Cited By :148.

[18] François Grimaldi, Annette Grimaldi-Lecourt, and M. W. C. Dharma-wardana. Time-dependent density-functional theory of light absorption in dense plasmas: Application to iron plasma. *Phys. Rev. A*, 32:1063–1071, Aug 1985.

[19] Manfred O. Krause, Thomas A. Carlson, and Anders Fahlman. Photoelectron spectrometry of manganese vapor between 12 and 110 ev. *Phys. Rev. A*, 30:1316–1324, Sep 1984.

[20] P. Hohenberg and W. Kohn. Inhomogeneous electron gas. *Phys. Rev.*, 136:B864–B871, Nov 1964.

[21] W. Kohn and L. J. Sham. *Phys. Rev.*, 140:A1133, 1965.

[22] N. David Mermin. Thermal properties of the inhomogeneous electron gas. *Phys. Rev.*, 137:A1441–A1443, Mar 1965.

[23] L. H. Thomas. *Proc. Camb. Phil. Soc.*, 23:542, 1927.

[24] E. Fermi. *Zeits. Phys.*, 48:73, 1928.

[25] B. F. Rozsnyai. Relativistic hartree-fock-slater calculations for arbitrary temperature and matter density. *Phys. Rev. A*, 5:1137, 1972.

[26] David A. Liberman. Self-consistent field model for condensed matter. *Phys. Rev. B*, 20:4981–4989, Dec 1979.

[27] C. E. Starrett and D. Saumon. *Phys. Rev. E*, 85:026403, 2012.

[28] C. E. Starrett and D. Saumon. Electronic and ionic structures of warm and hot dense matter. *Phys. Rev. E*, 87:013104, Jan 2013.

[29] F. Perrot. *Phys. Rev. A*, 42:4871, 1990.

[30] J. M. Ziman. *Proc. Phys. Soc.*, 91:701, 1967.

[31] L. Dagens. *J. Phys. C*, 5:2333, 1972.

[32] J. Chihara. Unified description of metallic and neutral liquids and plasmas. *J. Phys: Condens. Matter*, 3:8715, 1991.

[33] J. A. Anta and A. A. Louis. *Phys. Rev. B*, 61:11400, 2000.

[34] G. Faussurier. *Phys. Rev. E*, 69:066402, 2004.

[35] G. Zérah, J. Clérouin, and E. L. Pollock. *Phys. Rev. Lett.*, 69:446, 1992.

[36] T. Sjostrom and J. Daligault. *Phys. Rev. B*, 88:195103, 2013.

[37] D. M. Ceperley. Path integrals in the theory of condensed helium. *Rev. Mod. Phys.*, 67:279, 1995.

[38] K. P. Driver and B. Militzer. All-electron path integral monte carlo simulations of warm dense matter: Application to water and carbon plasmas. *Phys. Rev. Lett*, 108:115502, 2012.

[39] N. M. Gill and C. E. Starrett. Tartarus: A relativistic green's function quantum average atom code. *High Energy Density Phys.*, 24:33–38, 2017.

[40] Charles Edward Starrett, Nathanael Matthew Gill, Travis Sjostrom, and Carl William Greeff. Wide ranging equation of state with tartarus: A hybrid green's function/orbital based average atom code. *Computer Physics Communications*.

[41] N.M. Gill and C.E. Starrett. Mean-force scattering potential for calculating optical properties of dense plasmas. *High Energy Density Physics*, 31, 02 2019.

[42] N. M. Gill, R. A. Heinonen, C. E. Starrett, and D. Saumon. Ion-ion dynamic structure factor of warm dense mixtures. *Phys. Rev. E*, 91:063109, 2015.

[43] C. E. Starrett. A green's function quantum average atom model. *High Energy Density Phys.*, 16:18, 2015.

[44] T. Blenski and B. Cichocki. Variational theory of average-atom and superconfigurations in quantum plasmas. *Phys. Rev. E*, 75:056402, 2007.

[45] G. Faussurier, C. Blancard, P. Cossé, and P. Renaudin. Equation of state, transport coefficients, and stopping power of dense plasmas from the average-atom model

self-consistent approach for astrophysical and laboratory plasmas. *Phys. of. Plas.*, 17:052707, 2010.

[46] B. Wilson, V. Sonnad, P. Sterne, and W. Isaacs. Purgatorio–a new implementation of the inferno algorithm. *J. Quant. Spect. Rad. Trans.*, 99:658, 2006.

[47] R. Piron and T. Blenski. Variational-average-atom-in-quantum-plasmas (vaaqp) code and virial theorem: Equation-of-state and shock-hugoniot calculations for warm dense al, fe, cu, and pb. *Phys. Rev. E*, 83:026403, Feb 2011.

[48] S. Mazevet, M. P. Desjarlais, L. A. Collins, J. D. Kress, and N. H. Magee. Simulations of the optical properties of warm dense aluminum. *Phys. Rev. E*, 71:016409, 2005.

[49] M. P. Desjarlais, J. D. Kress, and L. A. Collins. Electrical conductivity for warm, dense aluminum plasmas and liquids. *Phys. Rev. E*, 66:025401(R), 2002.

[50] F. Lambert, J. Clérouin, J.-F. Danel, L. Kazandjian, and G. Zérah. Direct verification of mixing rules in the hot and dense regime. *Phys. Rev. E*, 77:026402, 2008.

[51] A. K. Rajagopa. Inhomogeneous relativistic electron gas. *J. Phys. C*, 11:L943, 1978.

[52] A. H. MacDonald and S. H. Vosko. A relativistic density functional formalism. *J. Phys. C*, 12:2977, 1979.

[53] J. Zabloudil, R. Hammerling, L. Szunyogh, and P. Weingberger. *Electron Scattering in Solid Matter: a Theoretical and Computational Treatise*. Springer Science Business Media, 2000.

[54] M. Klapisch A. Bar-Shalom, J. Oreg. Eosta—an improved eos quantum mechanical model in the sta opacity code. *J. Quant. Spect. Rad. Trans.*, 99:35, 2006.

[55] J. Oreg A. Bar-Shalom. Recent progress in the eosta model. *High Energy Density Phys.*, 5:196, 2009.

[56] Walter R. Johnson. *Atomic Structure Theory*. Springer, 2007.

[57] M. Kodama. Algorithm 877: A subroutine package for cylindrical functions of complex order and nonnegative argument. *ACM Trans. Math. Software*, 34:22, 2008.

[58] T. Blenski and K. Ishikawa. Pressure ionization in the spherical ion-cell model of dense plasmas and a pressure formula in the relativistic pauli approximation. *Phys. Rev. E*, 51:4869, 1995.

[59] Z. Gong, L. Zejda, and W. Dappen. Generalized fermi–dirac functions and derivatives: properties and evaluation. *Comp. Phys. Commun.*, 136:294, 2001.

[60] R. M. More. Pressure ionization, resonances, and the continuity of bound and free states. *Advances in atomic and molecular physics*, 21:305, 1985.

[61] Paul A.M. Dirac. Note on exchange phenomena in the thomas atom. *Proceedings of the Cambridge Philosophical Society*, 26:376, 1930.

[62] D. A. Liberman. *J. Quant. Spec. Rad. Trans.*, 27:335, 1982.

[63] W. R. Johnson, C. Guet, and G. F. Bertsch. Optical properties of plasmas based on an average-atom model. *J. Quant. Spect. Rad. Trans.*, 99:327, 2006.

[64] P.A. Sterne, S.B. Hansen, B.G. Wilson, and W.A. Isaacs. *High Energy Density Physics*, 3:278, 2007.

[65] M.B. Trzhaskovskaya and V.K. Nikulin. Atomic structure data based on average-atom model for opacity calculations in astrophysical plasmas. *High Energy Density Physics*, 26:1 – 7, 2018.

[66] M. Penicaud. *J. Phys. Condens. Matter*, 21:095409, 2009.

[67] A. A. Ovechkin, P. A. Loboda, and A. L. Falkov. Transport and dielectric properties of dense ionized matter from the average-atom reseos model. *High Energy Density Phys.*, 20:38–54, 2016.

[68] Balazs F. Rozsnyai, James R. Albritton, David A. Young, Vijay N. Sonnad, and David A. Liberman. Theory and experiment for ultrahigh pressure shock hugoniots. *Physics Letters A*, 291(4–5):226 – 231, 2001.

[69] M. W. C. Dharma-wardana and F. Perrot. *Phys. Rev. E*, 26:2096, 1982.

[70] J. Vackář O. Čertík, J. E. Pask. dftatom: A robust and general schrodinger and dirac solver for atomic structure calculations. *Computer Physics Communications*, 184:1777–1791, 2013.

[71] B.G. Wilson, D.D. Johnson, and A. Alam. Multi-center electronic structure calculations for plasma equation of state. *High Energy Density Physics*, 7(2):61 – 70, 2011.

[72] V. Eyert. A comparative study on methods for convergence acceleration of iterative vector sequences. *Journal of Computational Physics*, 124(2):271 – 285, 1996.

[73] D.G. Anderson. Iterative procedures for nonlinear integral equations. *Journal of the ACM (JACM)*, 12(4):547–560, 1965. cited By 281.

[74] A class of methods for solving nonlinear simultaneous equations. *Math. Comp.*, 19:577–593, 1965.

[75] D.D. Johnson. Modified broydens method for accelerating convergence in self-consistent calculations. *Physical Review B*, 38(18):12807–12813, 1988. cited By 369.

[76] Philip a. sterne, from inferno to purgatorio: An average- atom approach to equation of state and electrical conductivity calculation. ucrl-pres-225592.

[77] S. P. Lyon (ed.) and J. D. Johnson (ed.). *Los Alamos National Laboratory Tech. Rep.*, LA-UR-92-3407, 1992.

[78] R. M. More, K. H. Warren, D. A. Young, and G. B. Zimmernam. *Phys. Fluids*, 31:3059, 1988.

[79] Valentin V. Karasiev, Travis Sjostrom, James Dufty, and S. B. Trickey. *Phys. Rev. Lett.*, 112:076403, 2014.

[80] Travis Sjostrom and Jérôme Daligault. Gradient corrections to the exchange-correlation free energy. *Phys. Rev. B*, 90:155109, Oct 2014.

[81] X. Gonze, B. Amadon, P.-M. Anglade, J.-M. Beuken, F. Bottin, P. Boulanger, F. Bruneval, D. Caliste, R. Caracas, M. Côté, T. Deutsch, L. Genovese, Ph. Ghosez, M. Giantomassi, S. Goedecker, D.R. Hamann, P. Hermet, F. Jollet, G. Jomard, S. Leroux, M. Mancini, S. Mazevet, M.J.T. Oliveira, G. Onida, Y. Pouillon, T. Rangel, G.-M. Rignanese, D. Sangalli, R. Shaltaf, M. Torrent, M.J. Verstraete, G. Zerah, and J.W. Zwanziger. Abinit: First-principles approach to material and nanosystem properties. *Computer Physics Communications*, 180(12):2582 – 2615, 2009. 40 YEARS OF CPC: A celebratory issue focused on quality software for high performance, grid and novel computing architectures.

[82] X. Gonze, G.-M. Rignanese, M. Verstraete, J.-M. Beuken, Y. Pouillon, R. Caracas, F. Jollet, M. Torrent, G. Zerah, M. Mikami, P. Ghosez, M. Veithen, J.-Y. Raty, V. Olevano, F. Bruneval, L. Reining, R. Godby, G. Onida, D.R. Hamann, and D.C. Allan. A brief introduction to the abinit software package. *Zeitschrift fur Kristallographie*, 220(5-6):558–562, 2005. cited By 1013.

[83] François Jollet, Marc Torrent, and Natalie Holzwarth. Generation of projector augmented-wave atomic data: A 71 element validated table in the xml format. *Computer Physics Communications*, 185(4):1246 – 1254, 2014.

[84] N.A.W. Holzwarth, A.R. Tackett, and G.E. Matthews. A projector augmented wave (paw) code for electronic structure calculations, part i: atompaw for generating atom-centered functions. *Computer Physics Communications*, 135(3):329 – 347, 2001.

[85] A. M. Serenelli, S. Basu, J. W. Ferguson, and M. Asplund. New solar composition: the problem with solar models revisited. *Astrophy. J.*, 705:L123–L127, 2009.

[86] M. Asplund, N. Grevesse, J. A. Sauval, and P. Scott. The chemical composition of the sun. *Annu. Rev. Astron. Astrophys.*, 47:481–522, 2009.

[87] E. Caffau, H.-G. Ludwig, M. Steffen, B. Freytag, and P. Bonifacio. Solar chemical abundances determined with a co5bold 3d model atmosphere. *Sol. Phys.*, 268:255–269, 2011.

[88] R. Piron and T. Blenski. Average-atom model calculations of dense-plasma opacities: Review and potential applications to white-dwarf stars. *Contrib. Plasma Phys.*, 58:30–41, 2018.

[89] S. X. Hu, V. N. Goncharov, T. R. Boehly, R. L. McCrory, S. Skupsky, L. A. Collins, J. D. Kress, and B. Militzer. Impact of first-principles properties of deuterium-tritium on inertial confinement fusion target designs. *Physics of Plasmas*, 22:056304, 2015.

[90] R. Kubo. Statistical-mechanical theory of irreversible processes. i. general theory and simple applications to magnetic and conduction problems. *J. Phys. Soc. (Japan)*, 12:570–586, 1957.

[91] D. A. Greenwood. The boltzmann equation in the theory of electrical conduction in metals. *Proc. Phys. Soc. (London)*, 71:585, 1958.

[92] B. Holst, M. French, and R. Redmer. Electronic transport coefficients from ab initio simulations and applications to dense liquid hydrogen. *Phys. Rev. B*, 83:235120, 2011.

[93] J. Colgan, D. P. Kilcrease, N. H. Magee, M. E. Sherrill, J. Abdallah Jr., P. Hakel, C. J. Fontes, J. A. Guzik, and K. A. Mussack. A new generation of los alamos opacity tables. *Astrophys. J.*, 817:116, 2016.

[94] S. Hansen, J. Bauche, C. Bauche-Arnoult, and M. Gu. Hybrid atomic models for spectroscopic plasma diagnostics. *High Energy Density Phys.*, 3:109–114, 2007.

[95] C. A. Iglesias and F. J. Rogers. Opacities for the solar radiative interior. *Astrophys. J.*, 371:408–417, 1991.

[96] Q. Porcherot, J.-C. Pain, F. Gilleron, and T. A. Blenski. A consistent approach for mixed detailed and statistical calculation of opacities in hot plamas. *High Energy Density Phys.*, 7:234–239, 2011.

[97] G. Faussurier, C. Blancard, P. Renaudin, and P.L. Silvestrelli. Electrical conductivity of warm expanded al. *Phys. Rev. B*, 73:075106, 2006.

[98] M. W. C. Dharma-wardana, D. D. Klug, L. Harbour, and L. J. Lewis. Isochoric, isobaric, and ultrafast conductivities of aluminum, lithium, and carbon in the warm dense matter regime. *Phys. Rev. E*, 96:053206, 2017.

[99] C. E. Starrett and D. Saumon. Models of the elastic x-ray scattering feature for warm dense matter aluminum. *Phys. Rev. E*, 92:033101, 2015.

[100] N. R. Shaffer, N. G. Ferris, J. Colgan, D. P. Kilcrease, and C. E. Starrett. Free-free opacity in dense plasmas with an average atom model. *High Energy Density Phys.*, 23:31–37, 2017.

[101] M. Yu. Kuchiev and W. R. Johnson. *Phys. Rev. E*, 78:026401, 2008.

[102] C. E. Starrett. Kubo-greenwood approach to conductivity in dense plasmas with average atom models. *High Energy Density Phys.*, 19:58–64, 2016.

[103] M. P. Prange, J. J. Rehr, G. Rivas, J. J. Kas, and John W. Lawson. Real space calculation of optical constants from optical to x-ray frequencies. *Phys. Rev. B*, 80:155110, 2009.

[104] Z. J. Fu, Q. F. Chen, X. R. Chen, X. W. Sun, and W. L. Quan. Electrical conductivity and nonmetal-metal transition of dense iron and nickel plasmas. *Phys. Scr.*, 85:045502, 2012.

[105] R. W. Powell. The electrical resistivity of liquid iron. *The London, Edinburgh, and Dublin Philosophical Magazine and Journal of Science*, 354:772–775, 1953.

[106] B. F. Rozsnyai. Photoabsorption in hot plasmas based on the ion-sphere and ion-correlation models. *Phys. Rev. A*, 43:3035, 1991.

[107] N. Nettelmann, A. Becker, B. Holst, and R. Redmer. *The Astrophysical Journal*, 750:52, 2012.

[108] Report of ReNew workshop. *Basic research needs for high energy density laboratory physics*. U.S. Department of Energy, 2009. http://science.energy.gov/~/media/fes/pdf/workshop-reports/hedlp_brn_workshop_report_oct_2010.pdf.

[109] S. Atzeni and J. Meyer-Ter-Vehn. *The physics of inertial fusion*. Clarendon Press-Oxford, 2004.

[110] J. D. Kress, James S. Cohen, D. A. Horner, F. Lambert, and L. A. Collins. Viscosity and mutual diffusion of deuterium-tritium mixtures in the warm-dense-matter regime. *Phys. Rev. E*, 82:036404, Sep 2010.

[111] D. A. Horner, J. D. Kress, and L. A. Collins. Quantum molecular dynamics simulations of warm dense lithium hydride: Examination of mixing rules. *Phys. Rev. B*, 77:064102, Feb 2008.

[112] D. A. Horner, J. D. Kress, and L. A. Collins. Effects of metal impurities on the optical properties of polyethylene in the warm dense-matter regime. *Phys. Rev. B*, 81:214301, Jun 2010.

[113] Sebastien Hamel, Lorin X. Benedict, Peter M. Celliers, M. A. Barrios, T. R. Boehly, G. W. Collins, Tilo Döppner, J. H. Eggert, D. R. Farley, D. G. Hicks, J. L. Kline, A. Lazicki, S. LePape, A. J. Mackinnon, J. D. Moody, H. F. Robey, Eric Schwegler, and Philip A. Sterne. Equation of state of $ch_{1.36}$: First-principles molecular dynamics simulations and shock-and-release wave speed measurements. *Phys. Rev. B*, 86:094113, Sep 2012.

[114] J.-F. Danel and L. Kazandjian. Equation of state of a dense plasma by orbital-free and quantum molecular dynamics: Examination of two isothermal-isobaric mixing rules. *Phys. Rev. E*, 91:013103, Jan 2015.

[115] J. Vorberger, Z. Donko, I. M. Tkachenko, and D. O. Gericke. *Phys. Rev. Lett.*, 109:225001, 2012.

[116] James P. Mithen, Jérôme Daligault, and Gianluca Gregori. *Phys. Rev. E*, 83:015401, 2011.

[117] S. H. Glenzer and R. Redmer. *Rev. Mod. Phys.*, 81:1625, 2009.

[118] U. Zastrau, T. Burian, J. Chalupsky, T. Döppner, T.W.J. Dzelzainis, R.R. Fäustlin, C. Fortmann, E. Galtier, S.H. Glenzer, G. Gregori, L. Juha, H.J. Lee, R.W. Lee, C.L.S. Lewis, N. Medvedev, B. Nagler, A.J. Nelson, D. Riley, F.B. Rosmej, S. Toleikis, T. Tschentscher, I. Uschmann, S.M. Vinko, J.S. Wark, T. Whitcher, and E. Förster. Xuv spectroscopic characterization of warm dense aluminum plasmas generated by the free-electron-laser flash. *Laser and Particle Beams*, 30:45–56, 3 2012.

[119] J. Vorberger and D.O. Gericke. Effective ion–ion potentials in warm dense matter. *High Energy Density Physics*, 9(1):178 – 186, 2013.

[120] B. A. Hammel, S. W. Haan, D. S. Clark, M. J. Edwards, S. H. Langer, M. M. Marinak, and M. V. Patel. *High energy density physics*, 6:171, 2010.

[121] C. E. Starrett, D. Saumon, J. Daligault, and S. Hamel. Integral equation model for warm and hot dense mixtures. *Phys. Rev. E*, 90:033110, Sep 2014.

[122] J.P. Mithen. *PhD thesis, available at http://www.surrey.ac.uk/physics/people/james_mithen/*, 2012.

[123] John P. Perdew, Kieron Burke, and Matthias Ernzerhof. Generalized gradient approximation made simple. *Phys. Rev. Lett.*, 77:3865–3868, Oct 1996.

[124] Chen Huang and Emily A. Carter. Transferable local pseudopotentials for magnesium, aluminum and silicon. *Phys. Chem. Chem. Phys.*, 10:7109–7120, 2008.

[125] J.-P. Hansen and I.R. McDonald. *Theory of simple liquids, Third edition*. Academic Press, 2006.

[126] J. Chihara. *J. Phys.: Condens. Matter*, 12:231, 2000.

[127] Kathrin Wünsch, Jan Vorberger, G Gregori, and Dirk O Gericke. X-ray scattering as a probe for warm dense mixtures and high-pressure miscibility. *EPL (Europhysics Letters)*, 94(2):25001, 2011.

[128] A. N. Souza, D. J. Perkins, C. E. Starrett, D. Saumon, and S. B. Hansen. *Phys. Rev. E*, 89:023108, 2014.

[129] Jürgen Bosse, Gianni Jacucci, Marco Ronchetti, and Walter Schirmacher. *Phys. Rev. Lett.*, 57:3277–3279, 1986.

[130] W. Montfrooij, P. Westerhuijs, V. O. de Haan, and I. M. de Schepper. *Phys. Rev. Lett.*, 63:544–546, 1989.

[131] S. H. Glenzer, C. A. Back, K. G. Estabrook, R. Wallace, K. Baker, B. J. MacGowan, B. A. Hammel, R. E. Cid, and J. S. De Groot. Observation of two ion-acoustic waves in a two-species laser-produced plasma with thomson scattering. *Phys. Rev. Lett.*, 77:1496–1499, Aug 1996.

[132] Stefano Cazzato, Tullio Scopigno, Taras Bryk, Ihor Mryglod, and Giancarlo Ruocco. Crossover between hydrodynamic and kinetic modes in binary liquid alloys. *Phys. Rev. B*, 77:094204, Mar 2008.

[133] T. Ando. Inter-subband optical transitions in a surface space-charge layer. *Solid State Communications*, 21(1):133 – 136, 1977.

[134] V Peuckert. A new approximation method for electron systems. *Journal of Physics C: Solid State Physics*, 11(24):4945–4956, dec 1978.

[135] A. Zangwill and Paul Soven. Density-functional approach to local-field effects in finite systems: Photoabsorption in the rare gases. *Phys. Rev. A*, 21:1561–1572, May 1980.

[136] B. M. Deb and S. K. Ghosh. Schrödinger fluid dynamics of many-electron systems in a time-dependent density-functional framework. *The Journal of Chemical Physics*, 77(1):342–348, 1982.

[137] L. J. Bartolotti. Time-dependent extension of the hohenberg-kohn-levy energy-density functional. *Phys. Rev. A*, 24:1661–1667, Oct 1981.

[138] Libero J. Bartolotti. Time-dependent kohn-sham density-functional theory. *Phys. Rev. A*, 26:2243–2244, Oct 1982.

[139] Erich Runge and E. K. U. Gross. Density-functional theory for time-dependent systems. *Phys. Rev. Lett.*, 52:997–1000, Mar 1984.

[140] Robert van Leeuwen. Mapping from densities to potentials in time-dependent density-functional theory. *Phys. Rev. Lett.*, 82:3863–3866, May 1999.

[141] M.A.L. Marques and E.K.U. Gross. Time-dependent density functional theory. *Annual Review of Physical Chemistry*, 55(1):427–455, 2004. PMID: 15117259.

[142] Miguel Marques, Neepa Maitra, Fernando Nogueira, Eberhard Gross, and Angel Rubio. *Fundamentals of Time-Dependent Density Functional Theory*, volume 837. 01 2012.

[143] G. Vignale and Walter Kohn. Current-dependent exchange-correlation potential for dynamical linear response theory. *Phys. Rev. Lett.*, 77:2037–2040, Sep 1996.

[144] Gary Doolen and David A Liberman. Calculations of photoabsorption by atoms using a linear response method. *Physica Scripta*, 36(1):77–79, jul 1987.

[145] Thomas Blenski. On the linear dynamic response of average atom in plasma. *Journal of Quantitative Spectroscopy and Radiative Transfer*, 99(1):84 – 101, 2006. Radiative Properties of Hot Dense Matter.